UNIVERSITÀ DEGLI STUDI DI BOLOGNA

DOTTORATO IN INGEGNERIA ELETTRONICA, INFORMATICA E DELLE TELECOMUNICAZIONI
CAMPI ELETTROMAGNETICI - ING-INF/02
XX CICLO

PH.D. THESYS IN ELECTRONIC, COMPUTER SCIENCE AND TELECOMMUNICATION ENGINEERING
ELECTROMAGNETIC FIELDS - ING-INF/02
XX CYCLE

CO-SIMULAZIONE NONLINEARE / ELETTROMAGNETICA DI RADIOCOLLEGAMENTI A MICROONDE E ONDE MILLIMETRICHE

NONLINEAR / ELECTROMAGNETIC CO-SIMULATION OF MICROWAVES AND MILLIMETER-WAVES LINKS

TESI DI DOTTORATO DI / PH.D. THESYS BY :

PAOLO SPADONI

RELATORE / TUTOR :

Chiar.mo Prof. Ing. VITTORIO RIZZOLI

COORDINATORE / SUPERVISOR :

Chiar.mo Prof. Ing. PAOLO BASSI

CORRELATORI / CO-TUTORS :

Chiar.mo Prof. Ing. ALESSANDRA COSTANZO
Dott. Ing. DIEGO MASOTTI

TABLE OF CONTENTS

INDEX TERMS

Circuit-level

Link

End-to-End

Nonlinear circuits

Electromagnetic analysis

1.1 INTRODUCTION

In the last twenty years, electronics and telecommunications have increased at high speed. The trend, so far, is to integrate and miniaturize circuits, reducing the components size and increasing their number, in order to reach higher performances while limiting the costs. The need to integrate into a chip different functions, which were separated in the past, has become a must and, consequently, the electronic and telecommunication systems complexity has enormously increased.

From a radiofrequency designer point of view, the trend outlined is a challenge that must be faced with appropriate tools. The traditional circuit simulators, which, in the past, had to analyze low complexity circuits with about ten nonlinear components, now have to deal with high complexity circuits, containing hundreds or thousands of nonlinear devices. This means that simulation time increases and it is nomore affordable or compatible with industrial schedules; therefore, a new research field has been developed, and its task is to study of new algorithms that significantly reduce the simulation time of a high complexity circuit.

Beyond the traditional circuit simulators, a new family, the electromagnetic (EM) tools, has been adopted in the last ten years, in order to carry out high frequency system analyses and optimizations. The need of using this kind of tools is to handle electromagnetic coupling and spurious radiation in non-radiating structures, as well as properly characterizing the electromagnetic properties of radiating structures.

In the end, nowadays the challenge of a radiofrequency designer is to contain the costs, in terms of simulation time, while keeping a good degree of accuracy; this has to be done using the circuit and EM tools above mentioned.

1.2 AIM OF THE PH.D. THESIS

In order to describe the task of my thesis, I must state in advance a brief description of the simulation levels, which are related to the accuracy of the simulation performed. A first level is “physical”: this involves the computation of physical phenomena involved into semiconductors. It solves numerically partial differential equations for active elements, such as Drift-diffusion and Potential equation, and its variables can be the electrons flowing into transistor sections. Thus, it gives extremely accurate results notwithstanding it is time consuming. Anyway, it won't be treated anymore in the thesis work, since it would be too expensive in terms of time to simulate a microwave link.

A second level of simulation is the diagram block level, which goes under the name "system" level; such kind of simulation uses the circuit theory approach, but each element of the system is modelled through simple mathematical equations; for example a radiofrequency device is not described in terms of voltages or current, but simply by its representative network functions (an amplifier can be basically described by its gain, a filter by its attenuation and cut-off frequencies); though it's very fast, nevertheless its accuracy is very poor; therefore no industrial process can exclusively rely on this approach.

In between, the "circuit" level approach allows a characterization of a system in terms of voltages and current flowing into the circuit. It is much more accurate than the "system" level approach, and of course less precise than the "physical" one, but more effective for the circuit design. A device such as an amplifier is characterized by a number of information, included in an appropriate and flexible model, allowing to determine its actual nonlinear and linear behaviour. Linear components are simulated by using traditional approaches, such as nodal method or subnetwork growth method.

At this stage, the aim of my Ph.D. thesis can be expressed more clearly. The task is to develop a general and rigorous link analysis approach at *circuit-level*. So far, the link simulation was usually performed by using system simulation. No precise performances of the End-to-End link can be rigorously obtained with this approach. By means of the proposed approach, such accuracy can be obtained.

In order to reach such accuracy, it is necessary to proceed as follows. On one side, the non-radiating part of a telecommunication system is characterized by performing efficient circuit-level nonlinear analyses; this involves the utilization of circuit simulator, wherein algorithms for a fast nonlinear analysis are implemented. On the other side, the electromagnetic radiation of the antennas and, generally speaking, of all the critical structures from an EM point of view, is characterized by appropriate EM tools.

The proposed method is useful for two main reasons: first of all, the method that will be outlined can be of invaluable help in order to establish the accuracy of system-level simulation. In fact, such kind of simulation is too often imprecise. Its task is to give a feeling of the link performances, and, because of that reason, it's not as accurate as should be, regarding the RF designer needs. Therefore, this new method provides an important reference to evaluate the precision of such simulation, and may be used in the phase of behavioral models “validation”.

Secondly, the new approach could be used for the behavioral models “development”. In fact, by performing a set of circuit-level simulation through the new approach, it would be possible to construct a complete database, on which the behavioral model will be based. Such behavioral model could describe adequately the link in function of its critical variables, and, in principle, could be optimized in order to improve the link performances.

To summarize , the purpose of this thesis is to demonstrate that it’s possible to carry out a circuit-level simulation of an entire microwave link, in a reasonable amount of time. During the work, co-design techniques for the project of both antennas and microwave front-end at the same time have been developed.

The thesis work has been mainly developed in the Pontecchio Marconi laboratories of Electronics with the research group headed by Prof. Rizzoli, within D.E.I.S. department.

1.3 PREVIOUS APPROACHES TO THE LINK COMPUTATION

The simulation of the overall system, from the input bit stream to the output bit stream, is an ideal of radiofrequency (RF) engineers. The ability to simulate an entire RF system (starting from the modulator, to the power amplifier, to the antenna, the propagation channel, and, after that, to all the receiver chain) will enable an engineer to select each of the components in the system individually in order to optimize the complete link. The overall system goal is the minimization of bit error rate (BER).

As previously anticipated, usually the link simulation is carried-out at a system-level. Therefore, a diagram block of the system must be set up. The interconnected blocks implement elementary function, such as filtering, amplification, AC/DC conversion, mapping, detection in which the link can be split. For example, transmitter and receiver blocks are seen as an open chain of components characterized by some basic sort of behavioral model such as AM/AM-AM/PM characteristics. In a link analysis, this simulation is used for a preliminary link budget, because of its speed.

Let us explain now in details the several reasons whereby this kind of approach is not suitable. First, too often the components implemented in these simulation tools are ideal, i.e. there is no reference to the actual layout of the components. After that, several phenomena, which take place in the link computation, are disregarded. In particular, bidirectional signal flow can occur in the system chain, as well as nonlinear interactions among interconnected subsystems; in particular, this last limitation lies in the assumption that subsystem models are normally developed for ideal I/O terminations (e.g., 50 Ω), whereas the load, most of the time, is far from the ideal value and varies with the frequency [1]. Besides, hidden states of complex subsystems that are not excited in sinusoidal regime can strongly influence system dynamics under modulated drive. Finally, antennas are usually treated as isotropic point radiators that have no influence on signal transfer, while the antenna radiation pattern has a strong impact on the link performances, especially when a realistic scenario is taken into account.

Previous works in this field have been developed in order to characterize a link under modulated excitation . A system-level link simulated under several modulated RF drive has been presented by Pedro et al. in 2006 [2]. The co-simulation of low-pass equivalent behavioural models with circuit based models is addressed by simulating the overall wireless communication path. This work, notwithstanding it handles modulated signals, simulates only a limited number of nonlinear devices at a circuit-level. Consequently, the degree of accuracy is low in comparison with our method.

Moreover, a significant work on electromagnetic compatibility problems of a link subsystem [3], such as a nonlinear microwave integrated circuits, has been developed by the same research group in 2004. As far as the receiver part is concerned, the method developed is similar to the one used in this work. The radiation from the given circuit is first numerically analysed by means of electromagnetic simulation. Under the assumption of a uniform plane wave incident on the circuit, the reciprocity theorem is then used to characterize the linear subnetwork by a Norton equivalent circuit. Finally, a multitone harmonic-balance analysis allows the effects of the incident wave on the circuit electrical regime to be exactly investigated. In comparison with the proposed method, only a sinusoidal excitation is considered in 2004 approach, in contrast with the envelope transient technique here utilized. Moreover, a small link subsystem, which consists in an active integrated circuit, is analysed in 2004 approach, whereas a complete *End-to-End* microwave link, has been treated in this thesis.

2.1 INTRODUCTION

In this chapter, I will describe the main electromagnetic and circuit-level simulation tools used during the Ph.D. research period. Moreover, I will give an accurate description of the algorithms implemented in the in-house circuit simulator utilized.

2.2 ELECTROMAGNETIC TOOLS : CST MICROWAVE STUDIO

The electromagnetic tool utilized to model antennas is CST Microwave Studio. It's a full 3D simulator, based on the Finite integration technique (FIT) [4]. This is a time-domain method, which is conceptually different from the traditional Finite difference time domain technique (FDTD); the core difference lies in the discretization of the Maxwell equations: while the traditional FDTD discretizes them in their derivative form, the CST technique uses the integral form. Both spatial and time discretization are performed by the simulator. A short pulse in time-domain excites the structure at each port, and, once the response has been obtained, the simulator performs the ratio between the output and input signal at all ports; afterwards, it's possible to perform a Fast Fourier Transform over a wide bandwidth; in this way, the linear port-parameters at all ports are calculated, and, beyond them, all the typical quantities such as current density, power flow, electric and magnetic field on the metallization, far field can be straightforwardly computed.

In combination with the Finite Integration Technique, the perfect Boundary Approximation (PBA) is used for the spatial discretization of the structure. The simulated structure and the electromagnetic fields are mapped to hexagonal mesh. The mesh is automatically generated by the simulator, and it is basically related to the maximum simulation frequency. At such frequency, the algorithm calculates the correspondent wavelength, and it meshes this quantity a number of times according to the critical mesh parameters settings. PBA allows a very good approximation of even curved surfaces within the cubic mesh cells.

As for the stability of the simulation, the step width for the integration must not overcome a known limit, which is the "so called" Courant-Friedrichs-Levy. Let us assume that dx, dy, dz describe the cell sizes, "dt" is the time step, $(\sqrt{\varepsilon\mu})^{-1}$ the speed of light.

$$dt \leq \frac{\sqrt{\varepsilon\mu}}{\sqrt{\left(\frac{1}{dx}\right)^2+\left(\frac{1}{dy}\right)^2+\left(\frac{1}{dz}\right)^2}} \qquad (2.1)$$

The maximum usable time step dt is directly related to the mesh step width used in the discretization of the structure. In particular, from (2.1), the denser the chosen grid, the smaller the usable time step width. The tool is indicated above all for wide-band projects, because of the time-domain short pulse exciting the structure. Anyway, for resonant structures, the simulation cost in terms of time is not high in comparison with frequency-domain solvers, even if the latters are more suitable to analyze narrowband projects.

2.3 CIRCUIT-LEVEL SIMULATION TOOLS

Circuit-level simulation tools allow to characterize the nonlinear network functions, as well as the linear port parameters of the circuit. They provide an accurate calculation of the structure under test. For low frequency simulations, they are strongly indicated because there is a good trade-off between accuracy and simulation time. Nevertheless, as far as the frequency increases up to the GHz or more, they must be used carefully; their result can be not as proper as it should, since they disregard the electromagnetic coupling between different parts of the circuit, which is not negligible at high frequency. This problem is a concern in modern circuits, such as the well known “System-on-chip”(SoC), wherein the integration of small devices is a must.

As far as the circuit tool usedA powerful simulator, “NONLIN”, has been utilized to carry out circuit-level analysis. Let us give now an accurate description of the effective algorithm , the well-known “Harmonic Balance” (HB) technique, implemented in the in-house circuit-level simulator utilized during Ph.D. work. Note that §2.3.1,§2.3.2,§2.3.3, which exploit the HB core theory and evolutions, are extracts from papers [5],[6],[7]-[8] respectively.

2.3.1 HARMONIC BALANCE

The main advantages of this approach are its ability to directly address the steady-state circuit operation under single or multiple-tone excitation, and its full compatibility with the characterization of the linear subnetwork in the frequency domain, which is usually a prerequisite for high-frequency applications. On the other hand, the main drawback is that drawback is that nonlinear circuit analysis is reduced to the solution of a nonlinear algebraic system, which is usually obtained by some sort of iterative procedure. In traditional HB simulators, as the exciting signal levels are increased, the system becomes more and more ill-conditioned, and the iteration slows down and eventually fails. Thus it is usually taken for granted that harmonic balance handles extremely nonlinear behaviour poorly. Moreover, another drawback consists in the size of the solving system, which is equal to the number of state variables times the number of spectral lines. For multiple device circuits excited by multiple tones, this may lead to nonlinear problems with thousands of unknowns, which mean high simulation time. A countermove to handle this problem will be explained in §2.3.3 .

Let us consider a nonlinear microwave circuit operating in a quasi-periodic electrical regime generated by the intermodulation of F sinusoidal tones of incommensurable fundamental angular frequencies $\boldsymbol{\omega}_i$. Any signal a(t) supported by the circuit may be represented by the multiple Fourier expansion

$$a(t) = \sum_{\mathbf{k} \in \mathbf{S}} A_{\mathbf{k}} \exp(j\Omega_{\mathbf{k}} t) \tag{2.2}$$

where $\Omega_{\mathbf{k}}$ is a generic mixing or intermodulation (IM) product of the fundamentals, i.e.,

$$\Omega_{\mathbf{k}} = \sum_{i=1}^{F} k_i \omega_i = \mathbf{k}^{F} \boldsymbol{\omega}_i \tag{2.3}$$

In (2.2), (2.3) k_i is an integer harmonic number, $\mathbf{k}^{\mathbf{T}}$ is an F-vector of harmonic numbers, and $\boldsymbol{\omega}_i$ is the F-vector of the fundamentals. The vector **k** in (2.3) spans a finite subset **S** of the k-space (containing the origin) which will be conventionally named the *signal spectrum.* The Fourier coefficient $\mathbf{A}_{\mathbf{k}}$, will be named the *harmonic* of a(t) at $\Omega_{\mathbf{k}}$ (or the k-th harmonic of a(t)).

HB describes the circuit as interconnection of linear and nonlinear subsystems, as in fig. 2.1.

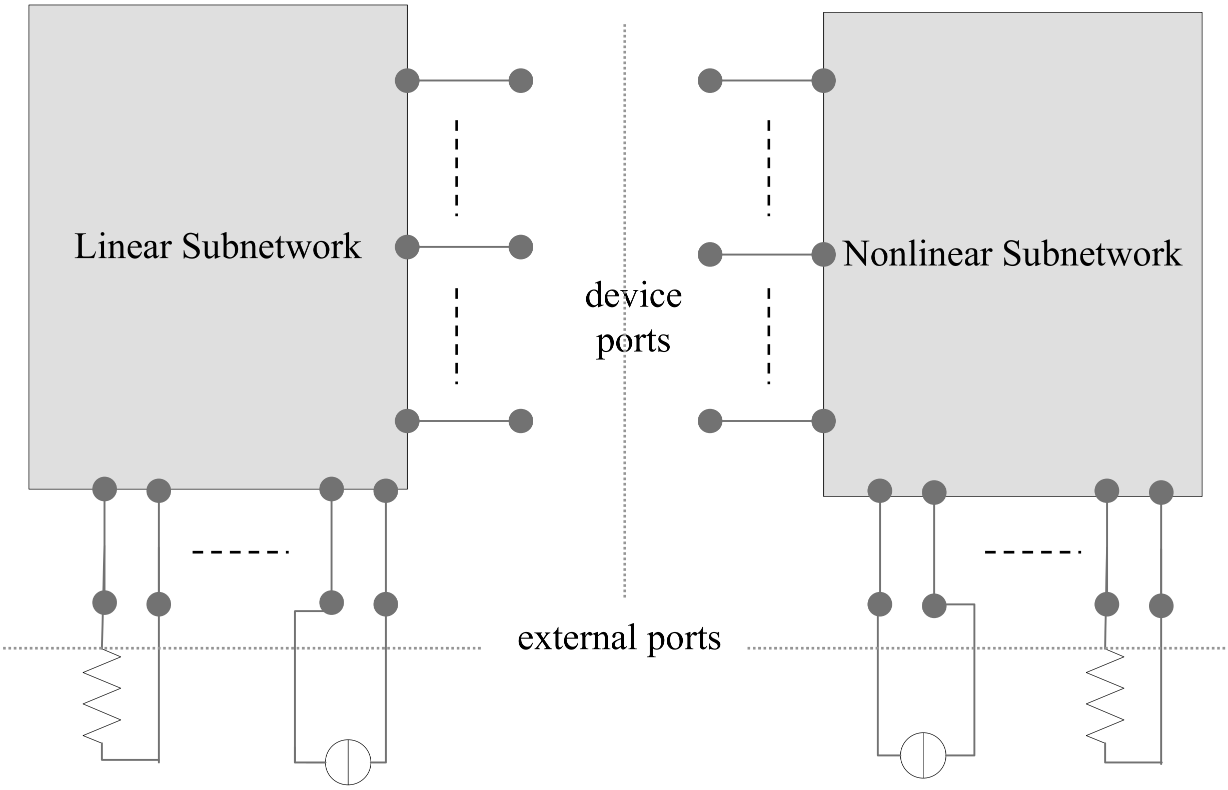

Figure 2.1 : Nonlinear and linear subnetwork – Harmonic Balance approach

Let the nonlinear subnetwork be described by the generalized parametric equations

$$\mathbf{v}(t) = \mathbf{u}\left[\mathbf{x}(t), \frac{d\mathbf{x}(t)}{dt}, \mathbf{x_d}(t)\right] \tag{2.4}$$

$$\mathbf{i}(t) = \mathbf{w}\left[\mathbf{x}(t), \frac{d\mathbf{x}(t)}{dt}, \mathbf{x_d}(t)\right]$$

where $\mathbf{v}(t)$, $\mathbf{i}(t)$ are vectors of voltages and currents at the common ports, $\mathbf{x}(t)$ is a vector of state variables and $\mathbf{x_d}(t)$ a vector of time-delayed state variables, i.e., $\mathbf{x_d}(t) = \mathbf{x_i}(t-\tau_i)$. The time delays may be functions of the state variables [9]. All vectors in (2.4) have a same n_D size equal to the number of device ports. This kind of representation is very convenient from the physical viewpoint, because it is in fact equivalent to a set of implicit integro-differential equations in the port currents and voltages.

This allows an effective minimization of the number of subnetwork ports [10], and, what is more important, results in extreme generality in device modeling capabilities. The quasi-periodic electrical regime of the nonlinear circuit resulting from a multitone excitation is completely defined by a set of timedependent state variables of the form (2.2), or equivalently by the vector **X** of the real and imaginary parts of their harmonics. The size of this vector is $n_T = n_{D*}n_H$, where n_H is the cardinality of the spectrum **S.** The entries of **X** represent the problem unknowns. In order to compute the harmonics $\mathbf{U_k}$, $\mathbf{W_k}$ of the nonlinear subnetwork response (2.4) to the multitone excitation described by a vector **X ,** the program makes use of the multiple fast Fourier transform (MFFT). The general-purpose application of this algorithm to nonlinear microwave circuit analysis was first reported in [11], and a detailed description of its implementation in a CAD environment is given in [10] **.** The excellent performance of the MFFT has been recently acknowledged by several authors (e.g. [12]) The linear subnetwork may be represented by the frequency-domain equation

$$\mathbf{Y}(\omega)\,\mathbf{V}(\omega) + \mathbf{N}(\omega) + \mathbf{I}(\omega) = 0 \qquad (2.5)$$

where $\mathbf{V}(\omega)$, $\mathbf{I}(\omega)$ are vectors of voltage and current phasors, $\mathbf{Y}(\omega)$ is the linear subnetwork admittance matrix, and $\mathbf{N}(\omega)$ is a vector of Norton equivalent current sources. Thus the set of complex harmonic-balance errors at a generic IM product $\mathbf{\Omega_k}$ has the expression

$$\mathbf{E_k(X) = Y(\omega_k)\, U_k\,(X) + N(\omega_k) + W_k\,(X)} \qquad (2.6)$$

The nonlinear analysis problem is reduced to the solution of a nonlinear algebraic system by imposing that all the HB errors vanish. In order to avoid the use of negative frequencies, the nonlinear solving system is formulated in terms of a vector **E** of real and imaginary parts of the HB errors given by (2.6) , and is thus written as a system of n_T real equations in n_T unknowns, namely

$$\mathbf{E(X) = 0} \qquad (2.7)$$

2.3.2 MODULATION ORIENTED HARMONIC BALANCE

The paragraph introduces a new approach to the circuit-level analysis of nonlinear RF/microwave subsystems driven by digitally modulated carriers. The circuit is simulated by a sequence of modified harmonic-balance analyses based on a Krylov-subspace method driven by an inexact Newton loop. In this way, very long bit sequences may be handled by the computer through simulation.

Let usassume that the impressed voltages of the forcing sources and the state variables (SV) are quasi-periodic phase- and amplitude-modulated signals of the form

$$\mathbf{x}(t) = \sum_{\mathbf{k}} \mathbf{X}_{\mathbf{k}}(t) \exp(j\Omega_{\mathbf{k}} t) \tag{2.8}$$

where $\Omega_{\mathbf{k}}$ is a generic intermodulation (IM) product of a set of RF fundamental angular frequencies ω_i. The complex quantity $\mathbf{X}_{\mathbf{k}}(t)$ is the complex modulation law (or complex envelope) of $\exp(j\Omega_{\mathbf{k}}t)$. We also assume that the modulation laws are arbitrary band-limited functions of time for which Fourier-integral representations always exist, e.g.,

$$\mathbf{X}_{\mathbf{k}}(t) = \int_{-\Omega_B}^{\Omega_B} \mathbf{X}_{\mathbf{k}}(\omega) \exp(j\omega t)\, d\omega \tag{2.9}$$

where the $\mathbf{X}_{\mathbf{k}}(\omega)$ are not dependent on time. The set of all complex quantities $\mathbf{X}_{\mathbf{k}}(\omega)$ represents the physical spectrum of $\mathbf{x}(t)$. The modulation laws are sampled at a number of uniformly spaced time instants t_n ($1 \leq n \leq N$), and the complex quantities $\mathbf{X}_{\mathbf{k}}(t_n)$ represent the problem unknowns. A generic t_n will be conventionally called a *modulation-law sampling (MS) instant*. The MS instants must be chosen in such a way as to satisfy the sampling theorem. For communication system applications, the modulation laws may be considered *baseband* functions in the sense that the upper band limit Ω_B may be assumed to be small with respect to any of the IM products of the RF fundamentals to be considered in the analysis, i.e $\Omega_B << \Omega_{\mathbf{k}}$, so that the electrical regime may be described as a sequence of RF steady states [13]. This condition is obviously violated for $\mathbf{k} = \mathbf{0}$ ($\Omega_0 = 0$), which implies that the d.c. component requires a special treatment, as will be discussed later on.

According to the piecewise HB technique, the nonlinear circuit is subdivided into a linear and a nonlinear subnetwork interconnected through n_D common ports (*device ports*). For the sake of simplicity, we shall assume that the nonlinear subnetwork may be described by the set of parametric equations, such as (2.4) . Furthermore, at a generic angular frequency Ω, the frequency-domain equations of the linear subnetwork are

$$\mathbf{I}_{\mathbf{L}}(\Omega) = \mathbf{Y}(\Omega)\,\mathbf{V}(\Omega) + \mathbf{Y}_{\mathbf{T}}(\Omega)\,\mathbf{F}(\Omega) \tag{2.10}$$

where $\mathbf{Y}(\Omega)$, $\mathbf{Y}_{\mathbf{T}}(\Omega)$ are admittance matrices, and $\mathbf{F}(\Omega)$ is the vector of complex phasors of the free sinusoidal voltage sources of angular frequency Ω connected to the source ports. The subscript “L” denotes the currents entering the linear subnetwork ports (*linear currents*).

The nonlinear subnetwork response to the excitations (2.8) is described by the time-dependent harmonics $\mathbf{U}_{\mathbf{k}}(t_n)$, $\mathbf{W}_{\mathbf{k}}(t_n)$. Such harmonics may be computed by the multi-dimensional FFT in a way similar to that discussed in [13] for the case of periodic modulation laws. However, in order to deal with the aperiodic case, the envelope derivatives at the MS instants are now approximated by one-sided multipoint incremental rules of the form [14]

$$\left.\frac{d\mathbf{X}_{\mathbf{k}}(t)}{dt}\right|_{t=t_n} \approx \sum_{m=0}^{M} a_m \mathbf{X}_{\mathbf{k}}(t_{n-m}) \tag{2.11}$$

where the coefficients a_m are explicitly listed in many mathematical handbooks [14], and may be regarded as known. M = 3 was empirically chosen as the default value. Due to (2.11), $\mathbf{U}_{\mathbf{k}}(t_n)$, $\mathbf{W}_{\mathbf{k}}(t_n)$, turn out to be nonlinear functions of $\mathbf{X}_{\mathbf{r}}(t_n)$, $\mathbf{X}_{\mathbf{r}}(t_{n-1})$, ..., $\mathbf{X}_{\mathbf{r}}(t_{n-M})$ for all $\mathbf{r}$.

The n_D-vector $\mathbf{i}_L(t)$ of the time-domain linear currents may be written in a form similar to (2.8), with time-dependent harmonics $\mathbf{I}_{\mathbf{Lk}}(t)$. We may also introduce the physical spectra of $\mathbf{v}(t)$, $\mathbf{i}(t)$, $\mathbf{i}_L(t)$, namely $\mathbf{U}_{\mathbf{k}}(\omega)$, $\mathbf{W}_{\mathbf{k}}(\omega)$, $\mathbf{I}_{\mathbf{Lk}}(\omega)$, by means of Fourier-integral representations similar to (2.8). From the linear subnetwork equation (2.10) we then obtain

$$\mathbf{I}_{\mathbf{Lk}}(\omega) = \mathbf{Y}(\Omega_{\mathbf{k}} + \omega)\,\mathbf{U}_{\mathbf{k}}(\omega) + \mathbf{Y}_{\mathbf{T}}(\Omega_{\mathbf{k}} + \omega)\,\mathbf{F}_{\mathbf{k}}(\omega) \tag{2.12}$$

Under the usual assumptions, if ω is a baseband frequency satisfying $|\omega| \leq \Omega_B$, a frequency change by ω will produce a very small modification of the microwave circuit admittances. Thus for all $\mathbf{k} \neq \mathbf{0}$ we may introduce the approximation

$$\mathbf{Y}(\Omega_{\mathbf{k}} + \omega) \approx \mathbf{Y}(\Omega_{\mathbf{k}}) + \left.\frac{d\mathbf{Y}(\Omega)}{d\Omega}\right|_{\Omega=\Omega_{\mathbf{k}}} \omega \tag{2.13}$$

A similar expansion holds for $\mathbf{Y_T}$. (2.13) are normally sufficient for all practical purposes, but the extension to Taylor expansions containing higher order terms in ω is straightforward. Making use of (2.8) , (2.11) , and (2.13) , $\mathbf{I_{Lk}}(t_n)$ may be directly computed as a function of $\mathbf{X_r}(t_n)$, $\mathbf{X_r}(t_{n-1})$, ... , $\mathbf{X_r}(t_{n-M})$ for all values of $\mathbf{r}$.

(2.13) holds with sufficient accuracy for all $\mathbf{k} \neq \mathbf{0}$. For $\mathbf{k} = \mathbf{0}$ the situation may be quite different, because the time constants of the d.c. circuit are normally long (in comparison to those of the microwave circuit), mainly because of the relatively large d.c. blocking capacitors and RF chokes. Thus if Ω_B is large enough, the d.c. modulation laws may operate in fully dynamic conditions, so that the approximation (2.13) may be grossly in error. In order to cope with this problem, a special algorithm has been implemented in order to compute the d.c. components (**0**-th harmonics) of the linear subnetwork response. The step responses at the linear subnetwork ports are evaluated and stored once for all. The excitations are approximated by staircase functions, and the baseband responses for each t_n are simply evaluated by linear superposition. In this way a uniform accuracy is obtained for all values of $\mathbf{k}$.

If we now balance the linear and nonlinear currents at all device ports and all MS instants, we obtain the time-domain equations

$$\mathbf{I_{Lk}}(t_n) + \mathbf{W_k}(t_n) \overset{\Delta}{=} \mathbf{E_k}(t_n) = \mathbf{0} \qquad (2.14)$$

If the time-dependent harmonics $\mathbf{I_{Lk}}(t_n)$, $\mathbf{W_k}(t_n)$ had been computed exactly, the set of (2.14) through (2.9) would also represent a sufficient condition for the physical spectra $\mathbf{W_k}(\omega)$ + $\mathbf{I_{Lk}}(\omega)$ to vanish. In reality the time-dependent harmonics are only approximately evaluated, so that the spectra are only approximately balanced by imposing (2.14). The approximation becomes worse as the modulation laws become faster.

If we denote by P the number of positive IM products $\Omega_{\mathbf{k}}$ of interest, (2.14) is a system of $N_T = N_{nD}(2P + 1)$ real equations in as many real unknowns (i.e., the real and imaginary parts of all harmonics $\mathbf{X_k}(t_n)$). Owing to the peculiar nature of the errors (2.14), a fast approach to the solution of (2.14) can readily be devised. For a fixed n and all $\mathbf{k}$ let us stack the real and imaginary parts of the errors (2.14) into a real error vector $\mathbf{E}_n$, and the real and imaginary parts of the complex vector phasors $\mathbf{X_k}(t_n)$ into a vector $\mathbf{S}_n$ of real unknowns unknowns. Recalling that $\mathbf{I_{Lk}}(t_n)$, and thus $\mathbf{E_k}(t_n)$ as well, is a nonlinear function of $\mathbf{X_r}(t_n)$, $\mathbf{X_r}(t_{n-1})$, ..., $\mathbf{X_r}(t_{n-M})$ for all values of $\mathbf{r}$, (2.14) may be re-written in the synthetic form

$$\mathbf{E}_n [\mathbf{S}_n, \mathbf{S}_{n-1}, ..., \mathbf{S}_{n-M}] = \mathbf{0} \qquad (2.15)$$
$$(1 \leq n \leq N)$$

For a given n, (2.15) can be viewed as a real system of $n_D(2P + 1)$ equations in as many unknowns (the entries of $\mathbf{S}_n$), with $\mathbf{S}_{n-1}, ..., \mathbf{S}_{n-M}$ playing the role of parameters. Thus with a suitable intialization of $\mathbf{S}_{n-1}, ..., \mathbf{S}_{n-M}$ for $1 \leq n \leq M$, (2.15) can be solved as a sequence of N independent HB systems of size n_D (2P + 1). For n = 1 a conventional HB system is solved. For n > 1 each nonlinear system is modified with respect to an ordinary HB analysis because the unknowns appear in it both in the normal way and through the approximations (2.11) of the envelope derivatives.

If $n_D(2P + 1)$ is relatively large, the nonlinear system associated with each MS instant can be most efficiently solved by a Krylov-subspace method driven by an inexact Newton loop, as is the case for ordinary HB analysis. If the MS instants were uncoupled, the analysis would reduce to a sequence of independent HB analyses, and each Jacobian matrix would be computed by the methods discussed in [15]. In reality, due to couplings established by (2.11), the Jacobian matrix is considerably more involved than the one obtained for ordinary HB [15], *but retains the same formal structure*. Thus it is still possible to carry out Jacobian-vector multiplications mostly by the FFT. This ensures that Krylov-subspace methods can be applied to modulation-oriented analysis with virtually the same efficiency that is already well established for ordinary multitone harmonic balance [15].

2.3.3 OUTLINE OF DOMAIN – PARTITIONING HARMONIC BALANCE TECHNIQUE (DHB)

In order to enhance the efficiency of system-oriented HB simulation, a new method has been developed in the last five years. The new feature is that it can optimally exploit the block structure of the system to be analysed. In this paragraph, we will give only an overview of this technique; analytical details may be found in [7]. The basic idea is to introduce a set of auxiliary state variables (SV) consisting of the voltages at the subsystem ports, which creates in the Jacobian matrix a well-defined sparsity pattern. Such sparsity can be effectively exploited in a hierarchical solution approach if ordinary HB techniques are used [10], or in the simultaneous solution for all the unknowns when the HB analysis is performed by Krylov-subspace methods [15]. The overhead introduced by the auxiliary unknowns is normally small, so that important savings of both memory and CPU time are obtained, and really huge simulation tasks may be brought within the reach of even ordinary PC's. All the nonlinear interactions between subsystems are exactly accounted for in the analysis, both in band and out of band, and all the peculiar advantages of SV-based HB analysis are fully retained by the new technique. In particular, an arbitrary number of linear subsystems of any complexity may be included in the system without substantially affecting memory and CPU time requirements.

The technique has been coupled to the envelope-transient harmonic balance (DHB-MHB) too [8]. In this case, once the circuit has been suitably subdivided into blocks, a further significant enhancement in analysis performance may be obtained by limiting each block's spectrum to the set of lines that are relevant to the block electrical function. In fact, an RF/microwave transceiver would typically consist of interconnected sections that operate at different frequency bands, such as the RF, the intermediate frequency (IF), and baseband sections. This situation is exploited to significantly reduce the overall number of unknowns by DHB algorithm based on a hierarchical domain decomposition. A regular multitone HB analysis with all the intermodulation (IM) products of the unmodulated forcing carriers is first performed to identify the subcircuits that operate with similar spectra. This defines the 1st-tier decomposition. The spectrum for each 1st-tier block is automatically redefined by eliminating the negligible lines, and the interblock connection equations are accordingly modified (again, in an automatic way). Within each 1st-tier block a 2nd-tier near-optimal decomposition is then automatically operated by the algorithm discussed in [16]. The carrier(s) modulation is then reintroduced, and the bulk of the simulation is performed by envelope-oriented analysis based on DHB [7].

In the end, the key idea is to couple this approach to the analysis technique that will be discussed in chapter 3.5; the latter, which is the core of my Ph.D. work, handles general and rigorous IF-to-IF link simulations, by means of circuit-level nonlinear/electromagnetic technique. Hereby, I anticipate that the combination of the two techniques opens the way to an effective co-simulation of the RF circuitry and baseband transceiver sections.

3.1 INTRODUCTION

The link analysis tools and algorithms previously described have been used during the whole Ph.D. work. A general description of method will be provided in the next paragraphs, followed by a numerical example of application.

3.2 GENERAL DESCRIPTION OF THE METHOD

The simulation of a microwave link, considered from the transmitter to the receiver intermediate frequency (IF) ports, is tackled by a rigorous circuit-level nonlinear analysis approach; this is coupled with the electromagnetic (EM) characterization of both the transmitting and receiving antennas, in order to set up a circuit-level nonlinear/EM co-simulation technique.

In fig. 3.1, a block diagram is shown, in order to visualize the conceptual blocks of the link. On the left, note the IF signal source, which is injected into the transmitter; the latter carries out an amplification and an up-conversion of the source signal. The radiofrequency signal flowing out at the output port is then transmitted by the transmitting antenna through the propagation channel. This signal is received by the receiving antenna, and, after that, amplified and down-converted by the receiver to IF frequency. For following considerations, it's worth splitting the microwave link in a nonlinear part and in a linear part. The former includes the transmitter and the receiver (circled), the latter contains both the antennas and the channel (included in the rectangle).

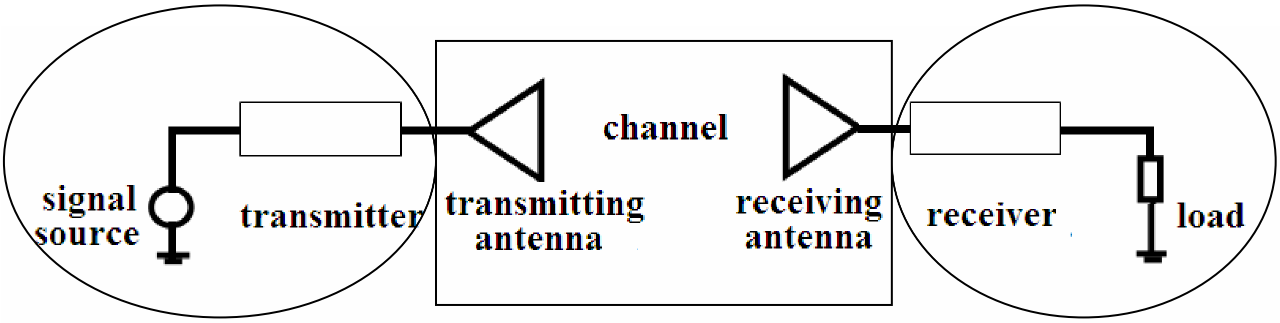

Figure 3.1: Microwave link in terms of its functional blocks

As far as the nonlinear part is concerned, transmitter and receiver are characterized at a circuit-level .They are described by the interconnection of linear and nonlinear subnetwork through device ports, according the Harmonic Balance technique illustrated in §2.2.1 ; external ports are available for RF, DC sources and load (fig. 2.1); a piecewise HB analysis is carried out in order to find the vector of state-variable harmonics (which characterize the state of the system) and of voltage and current harmonics at all ports.

Switching to the linear part, an essential aspect of link calculation is the antenna problem. Antennas are often described as ideal isotropic point sources, which in fact means that their effects on the link performance are not considered. In this approach, antennas are rigorously characterized by EM analysis, and become part of the front-end linear subnetwork. Moreover, we take into account the presence of any scatterer located in the proximity of the antenna (such as the antenna support or even other neighboring antennas), so that all relevant near-field effects be included in the results.

The procedure can be briefly described in the following way. A full-wave simulation of the transmitter and the transmitting antenna is performed with MHB algorithm to produce the radiated field envelope. The far field radiated by the transmitting antenna is expressed as a linear combination of the linear subnetwork port voltages, and the coefficients of such map are found by a cheap post-processing of EM results.

At this stage, reciprocity theorem is applied in order to compute the equivalent Norton current source of the receiving antenna. We subdivide this procedure in two steps. For instance, the field radiated by the transmitting antenna is computed in the receiving antenna phase center, in the absence of the receiving antenna itself. In the second place, the receiving antenna is used in a transmitting mode, and its normalized radiated field is computed in the actual transmitting antenna phase center, in the absence of transmitting antenna itself. Such information is properly combined to find the expression of the equivalent Norton current source of the receiving antenna.

In the end, another nonlinear step takes place. It consists in carrying out an envelope transient analysis of the receiver, to find the IF output current complex envelope.

This approach allows to take into account noise and interference effects as well as refined channel models in a straightforward way.

3.2.1 TRANSMITTER SIDE

The purpose of this paragraph is to characterize by an analytical point of view the procedure applied at the transmitting side.

We can assume that the antenna is excited by a sinusoidal current of angular frequency ω injected at its input port. The EM analysis provides the antenna input admittance $Y_{TA}(\omega)$ and the radiated far-field pattern. More precisely, if we denote by $\mathbf{E_T}$ $(r, \theta, \phi; \omega)$ the radiated far field in a suitable spherical coordinate system, the EM simulator will generate a data base containing the scalar components A_θ, A_ϕ, of the normalized field $\mathbf{E_{Tn}}$ $(r, \theta, \phi; \omega)$.

$$\mathbf{E_{Tn}}(\theta, \phi; \omega) = r \exp(j\beta r) \frac{\mathbf{E_T}(r, \theta, \phi; \omega)}{I_{TA}(\omega)} \tag{3.1}$$

where $I_{TA}(\omega)$ is the excitation current phasor. Under the assumption of free-space propagation, we may thus represent the radiated far field in the matrix form

$$\mathbf{E_T}(r, \theta, \phi; \omega) = \frac{\exp(-j\beta r)}{r} \begin{bmatrix} A_\theta(\theta, \phi; \omega)\, \hat{\boldsymbol{\theta}} \\ A_\phi(\theta, \phi; \omega)\, \hat{\boldsymbol{\phi}} \end{bmatrix} I_{TA}(\omega) \tag{3.2}$$

Let us now assume that the transmitter front-end is excited by a sinusoidal IF signal of angular frequency ω_{IF} and by a sinusoidal local oscillator (LO) of angular frequency ω_{LOT}. The resulting large-signal regime will be quasi-periodic with spectral lines at all the intermodulation (IM) products

$$\begin{aligned} \Omega_k &= k_1 \omega_{IF} + k_2 \omega_{LOT} \\ \mathbf{k} &= [k_1 \quad k_2]^{tr} \end{aligned} \tag{3.3}$$

At the k-th IM product, the front-end output port is loaded by the antenna admittance $\mathbf{Y_{TA}(\Omega_k)}$ generated by EM simulation. A multitone HB analysis may now be carried out by well-known algorithms to compute the vectors of the state-variable harmonics, X, and of the voltage harmonics at the LS ports, V_T, at each IM product of a suitably truncated finite spectrum. One of such products is the RF frequency ω_{RF}. A standard analysis of the LS by linear circuit techniques then allows the RF antenna excitation to be expressed in the form

$$I_{TA}(\omega_{RF}) = \mathbf{Y_t}(\omega_{RF})\, \mathbf{V_T}(\omega_{RF}) \qquad (3.4)$$

where $\mathbf{Y_t}$ (ω) is a transadmittance matrix. By replacing (3.4) into (3.2) we may directly express the far field as a function of the voltage harmonics at the LS ports:

$$\mathbf{E_T}(r, \theta, \phi; \omega_{RF}) = \frac{\exp(-j\beta r)}{r}\, \mathbf{A}(\theta, \phi; \omega_{RF}) \bullet \mathbf{V_T}(\omega_{RF}) \qquad (3.5)$$

where $\mathbf{A}$ is a (2 x n_{DT}) tensor defined by the inner product

$$\mathbf{A}(\theta, \phi; \omega) \bullet \mathbf{V_T}(\omega) \equiv \begin{bmatrix} \hat{\boldsymbol{\theta}}\, A_\theta(\theta, \phi; \omega)\, \mathbf{Y_t}(\omega)\, \mathbf{V_T}(\omega) \\ \hat{\boldsymbol{\phi}}\, A_\phi(\theta, \phi; \omega)\, \mathbf{Y_t}(\omega)\, \mathbf{V_T}(\omega) \end{bmatrix} \qquad (3.6)$$

In this way, it's possible to characterize precisely the E_θ and E_ϕ components of the radiated far-field, which are strongly related to the coefficients $A_\theta(\theta,\phi,\omega)$ and $A_\phi(\theta,\phi,\omega)$.

When one of the signals exciting the front-end is modulated, due to the circuit nonlinearity modulation is transferred onto all IM products of the carrier frequencies. The circuit state $\mathbf{x}(t)$ may thus be represented in the form

$$\mathbf{x}(t) = \sum_{\mathbf{k}} \tilde{\mathbf{X}}_{\mathbf{k}}(t) \exp(j\Omega_{\mathbf{k}} t) \qquad (3.7)$$

where the superscript ~ denotes time-dependent complex envelopes. Obviously, x(t) can represent a voltage or a current envelope at linear subnetwork ports. In such conditions, the circuit may be analysed by the MHB technique described in §2.2.2, where the circuit simulation is reduced to a sequence of multitone HB analyses associated with the envelope sampling instants and coupled through the envelope dynamics.

The key aspect of this method is the calculation of the linear and nonlinear subnetwork responses to a modulated excitation. The latter is rigorously handled by the multidimensional FFT, that allows decoupling of the carrier and modulation time scales.

The linear subnetwork response can be exactly evaluated by time-domain convolution [13]. The latter is the standard procedure to follow if the signal exciting the transmitting Front-End has a wide band.

In our case studies, modulated signals have moderate bandwidth; therefore, it is sufficient to resort to Taylor expansions of the linear subnetwork circuit parameters in the neighborhood of each intermodulation product $\mathbf{\Omega_k}$. For our present purpose, the focus is the intermodulation product ω_{RF} . At this stage, after having computed the linear subnetwork complex envelope voltages through MHB and, in particular, the antenna port voltage $\tilde{\mathbf{V}}_T(t)$. In such a case, the far field complex envelope takes on the expression given below

$$\begin{aligned}\tilde{\mathbf{E}}_\mathbf{T}(r,\theta,\varphi;t) \approx {} & \frac{\exp(-j\beta r)}{r}\,\mathbf{A}(\theta,\varphi;\omega_{RF})\bullet\tilde{\mathbf{V}}_\mathbf{T}(t) - \\ & - j\frac{1}{r}\left.\frac{d\left[\exp(-j\beta r)\,\mathbf{A}(\theta,\varphi;\omega)\right]}{d\omega}\right|_{\omega_{RF}} \bullet \frac{d\tilde{\mathbf{V}}_\mathbf{T}(t)}{dt} - \\ & - \frac{1}{r}\left.\frac{d^2\left[\exp(-j\beta r)\,\mathbf{A}(\theta,\varphi;\omega)\right]}{d\omega^2}\right|_{\omega_{RF}} \bullet \frac{d^2\tilde{\mathbf{V}}_\mathbf{T}(t)}{dt^2}\end{aligned} \tag{3.8}$$

This kind of analysis has been found to produce negligible errors for signal bandwidths up to about 10 ÷ 15% of the carrier.

Consequently, the far-field envelope may be computed through (3.8) just as any other LS response. Looking through (3.8), the Taylor expansion in the neighborhood of the carrier includes up to the second-order term. This is necessary in order to accurately account for antenna resonant behaviour.

3.2.2 ANTENNA EMBEDDING

In the analysis approach discussed in the previous sections both for the transmitter and the receiver front ends, it is assumed that the antenna is embedded in the linear subnetwork, and that EM interactions may take place between the entire linear subnetwork and the antenna and/or the environment. This situation is schematically illustrated in fig. 3.2 a); in such case all the linear subnetwork ports are device ports, in the sense that they are used to connect the linear subnetwork with the front-end nonlinear devices. In many practical cases the situation may be simpler than this, in the sense that EM interactions may be limited to a relatively small part of the linear subnetwork, which will be conventionally named the *radiating linear subnetwork* and will be identified by the symbol $\mathfrak{N}_{rad}$. $\mathfrak{N}_{rad}$ must obviously be described layout-wise and treated by full-wave EM analysis as detailed above. The remaining part of the linear subnetwork, which will be called the *non-radiating linear subnetwork* and will be identified by the symbol $\mathfrak{N}_{nr}$, may be treated by conventional circuit analysis algorithms. This has the obvious advantage of reducing the overall number of EM simulations that are required to perform the link analysis. In this case some of the ports of both $\mathfrak{N}_{rad}$ and $\mathfrak{N}_{nr}$ are connection ports used to interconnect the two front-end sections, as illustrated in fig. 3.2 b). From a nonlinear analysis viewpoint, harmonic balance simulation is now carried out by nonlinear segmentation according to the general approach introduced in [17]. While algorithmic details will not be repeated here, for our present purposes it is worth mentioning that segmentation requires the introduction of an auxiliary set of state variables consisting of the voltages at the connection ports [17]. In this case the analysis procedure based on EM simulation is carried out for $\mathfrak{N}_{rad}$ only. On the transmitter side, (3.5) and (3.8) are still valid, with $\mathbf{V_T}$ now representing the vector of the voltage phasors at all the ports of $\mathfrak{N}_{rad}$ (including device and connection ports) at angular frequency ω_{RF}. As a limiting case, $\mathfrak{N}_{rad}$ for the transmitter and the receiver may reduce to the antenna only, as illustrated in fig. 3.2 c). In this situation $\mathfrak{N}_{rad}$ has just one connection port for each front end, and $\mathbf{V_T}(\omega)$ reduces to a scalar voltage, respectively.

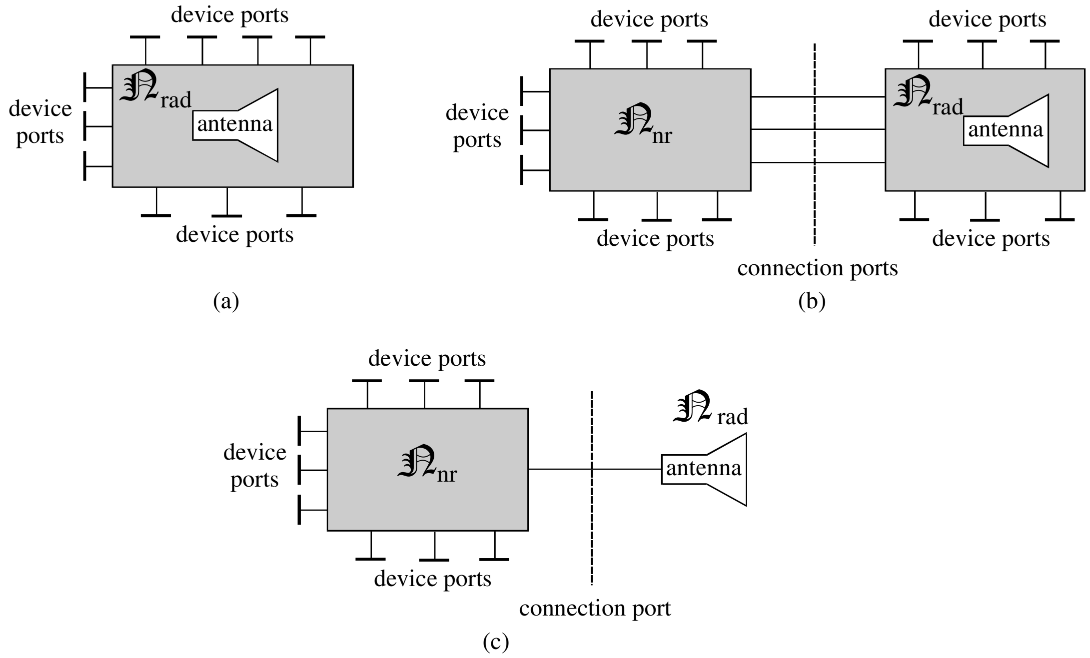

(a) (b)

(c)

Figure 3.2 : Linear subnework; a) antenna as part of the radiating linear subnetwork; b) multiport antenna connected to the non-radiating linear subnetwork; c) 1-port antenna connected to the non-radiating linear subnetwork.

3.2.3 RECEIVING SIDE

The receiver front-end is a nonlinear network described at the circuit level in a way similar to the transmitter. Its input port is connected to the receiving antenna port, as shown in fig.3.1. Once the relevant information on the EM field incident on the receiving antenna has become available, the primary remaining problem is to derive from it a circuit-level description of the receiver excitation. As for the transmitting side, we first consider the case of a purely sinusoidal incident field at a generic angular frequency ω. The distance between transmitter and receiver is assumed to be large enough to provide virtually ideal decoupling, so that the receiving antenna in the presence of the incident field behaves as a linear active one-port network. If we label by the subscript “RA” any electrical quantity pertaining to the receiving antenna port, the antenna equation may be written in the form

$$I_{RA}(\omega) = Y_{RA}(\omega)\, V_{RA}(\omega) + J_{RA}(\omega) \tag{3.9}$$

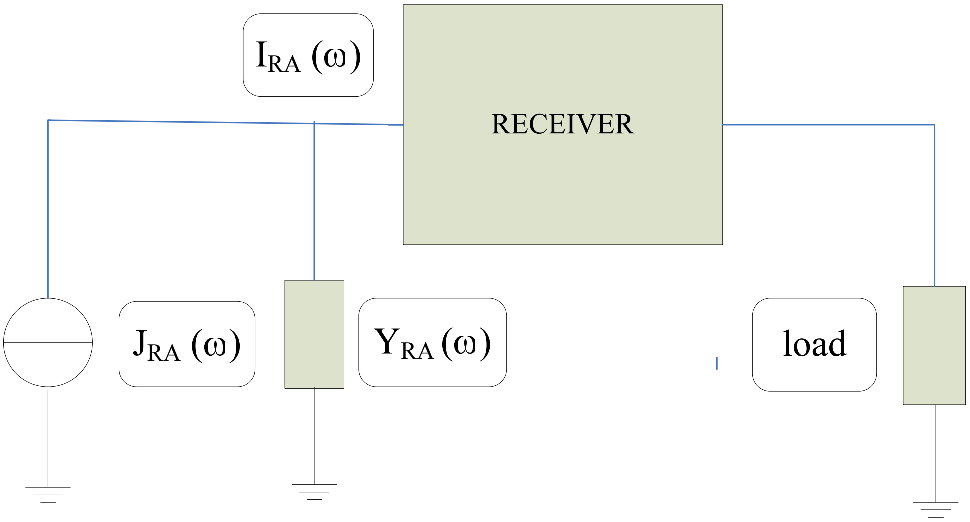

Figure 3.3: Norton equivalent circuit of the active linear subnetwork connected to the receiver

The admittance $Y_{RA}(\omega)$ appearing in (3.9) may be found by EM simulation of the antenna in the absence of any incident field. The problem thus essentially consists in finding the Norton equivalent current source J_{RA}, as in fig. 3.3, which represents the Norton equivalent circuit of the linear subnetwork connected to the receiver. Note that this source only depends on the transmitter electrical regime through the incident field (3.5), and plays thus the role of a free source in the receiver analysis.

In order to compute J_{RA}, we make use of a technique conceptually similar to the one introduced in [3] for interference analysis. We first suppress the incident field and use the receiving antenna in a transmitting mode. In this mode the antenna is excited by an arbitrary current J injected at the antenna port. In such conditions we analyse the antenna by the 3-D EM simulator to derive both the antenna admittance and the distribution of the radiated far field. If we denote by $\mathbf{E_R}$ (r', θ', ϕ'; ω) the radiated far field in a suitable spherical coordinate system (usually different from the previous one), the EM simulator will generate a data base containing the scalar components of the normalized field $\mathbf{E_{Rn}}$(r', θ', ϕ'; ω).

$$\mathbf{E_{Rn}}(\theta',\phi';\omega) = r'\exp(j\beta r')\,\frac{\mathbf{E_R}(r',\theta',\phi';\omega)}{J} \qquad (3.10)$$

Once again, in this simulation we may take into account the presence of any scatterer located in the vicinity of the antenna, so that all relevant near-field effects be included in the results. As a second step, the antenna is used in a receiving mode, in the presence of the incident field $\mathbf{E_T}$. In such conditions, making use of the reciprocity theorem we may directly express the unknown in the following form [3]:

$$\begin{aligned} J_{RA}(\omega) &= j\frac{2}{\eta}\,\lambda\, Y_{RA}(\omega)\; \bullet \\ &\bullet\, \mathbf{E_{Rn}}(\theta_I',\phi_I';\omega) \bullet \mathbf{E_T}(r,\theta_I,\phi_I;\omega) \end{aligned} \qquad (3.11)$$

where (θ_I, ϕ_I), (θ_I', ϕ_I') are the angular coordinates of the direction of incidence in the two reference frames. If we now assume that only the signal received at ω_{RF} is significant and make use of (3.5), (3.6), we obtain the key result

$$\begin{aligned} J_{RA}(\omega_{RF}) &= j\frac{2}{\eta}\,\lambda\, Y_{RA}(\omega_{RF})\,\frac{\exp(-j\beta r)}{r}\; \bullet \\ &\bullet\, \mathbf{E_{Rn}}(\theta_I',\varphi_I';\omega_{RF}) \bullet \left[\mathbf{A}(\theta_I,\varphi_I;\omega_{RF}) \bullet \mathbf{V_T}(\omega_{RF})\right] \equiv \qquad (3.12) \\ &\equiv \mathbf{B}(\omega_{RF})\,\mathbf{V_T}(\omega_{RF}) \end{aligned}$$

relates the receiver exciting source to the transmitter electrical regime through a set of complex transfer functions (the n_{DT} entries of the row matrix **B**) that include a most general and rigorous way the performance of both the transmitting and receiving antenna as generated by EM simulation. $\mathbf{B}(\omega)$ is named "link transfer function". Note that (3.12) is valid for free-space propagation only, but the analysis can easily be extended to realistic channel models. As for this extension, it will be outlined in chapter 5. When the incident field is modulated with a carrier frequency ω_{RF}, constant complex phasors in (3.11) are replaced by time-dependent complex envelopes. By an argument similar to the one developed in the previous section, we may cast the Norton source envelope in the form

$$\begin{aligned} \tilde{J}_{RA}(t) \approx \mathbf{B}(\omega_{RF})\,\tilde{\mathbf{V}}_{\mathbf{T}}(t) - j\left.\frac{d\mathbf{B}(\omega)}{d\omega}\right|_{\omega_{RF}} \frac{d\tilde{\mathbf{V}}_{\mathbf{T}}(t)}{dt} - \\ - \left.\frac{d^2\mathbf{B}(\omega)}{d\omega^2}\right|_{\omega_{RF}} \frac{d^2\tilde{\mathbf{V}}_{\mathbf{T}}(t)}{dt^2} \end{aligned} \qquad (3.13)$$

At this stage, a nonlinear analysis of the receiver front-end in presence of the incident field may be carried out by the MHB technique. The primary receiver excitations are represented by a local oscillator of angular frequency ω_{LOR} and by a modulated sinusoidal current source of angular frequency ω_{RF} and modulation law expressed by (3.13), connected in parallel to the antenna terminals. In the multitone HB analysis associated with each envelope sampling instant, the spectral lines are located at the IM products of ω_{RF}, ω_{LOR}, and the antenna port is loaded by the admittance $Y_{RA}(\mathbf{\Omega_k})$ computed by EM simulation. The MHB analysis then provides the complex envelopes of all signals supported by the receiver, including the IF output voltage. In addition, since the MHB approach allows modulation to be simultaneously applied to any harmonic including DC [2], both low-frequency and RF noise sources can be added to the analysis, including LO noise.

Noise modulation laws are described as complex random signals directly in the time domain. Finally, any interfering signals incident on the antenna, either sinusoidal or modulated, can be treated in much the same way as the desired signal. Each interferer will add one independent tone to the receiver multitone excitation.

3.3 NUMERICAL EXAMPLE OF APPLICATION

In order to give a feeling of the performance of the method, in this paragraph I will discuss a representative numerical example. In the next paragraphs, there will be a detailed description of the basic blocks shown in fig. 3.1.

3.3.1 TRANSMITTER

We consider a single-conversion transmitter front-end including a doubly-balanced quadrature mixer arranged in a lower sideband suppressing configuration, amplifiers, passive coupling circuits, and several linear parasitics. Let us now comment the figure 3.4 , which shows the mixer in terms of its functional blocks. After an IF preamplifier, a lumped quadrature coupler splits the signals in two different paths. Another amplifier, for each way, precedes the doubly-balanced mixer, whose task is to up-convert the IF signal to RF. In order to fulfil its function, the mixer makes use of a local oscillator (LO) signal at high power. Finally, the two signals are phased and combined by an in-phase power combiner, then the resulting RF signal is amplified before flowing out at the transmitter output port.

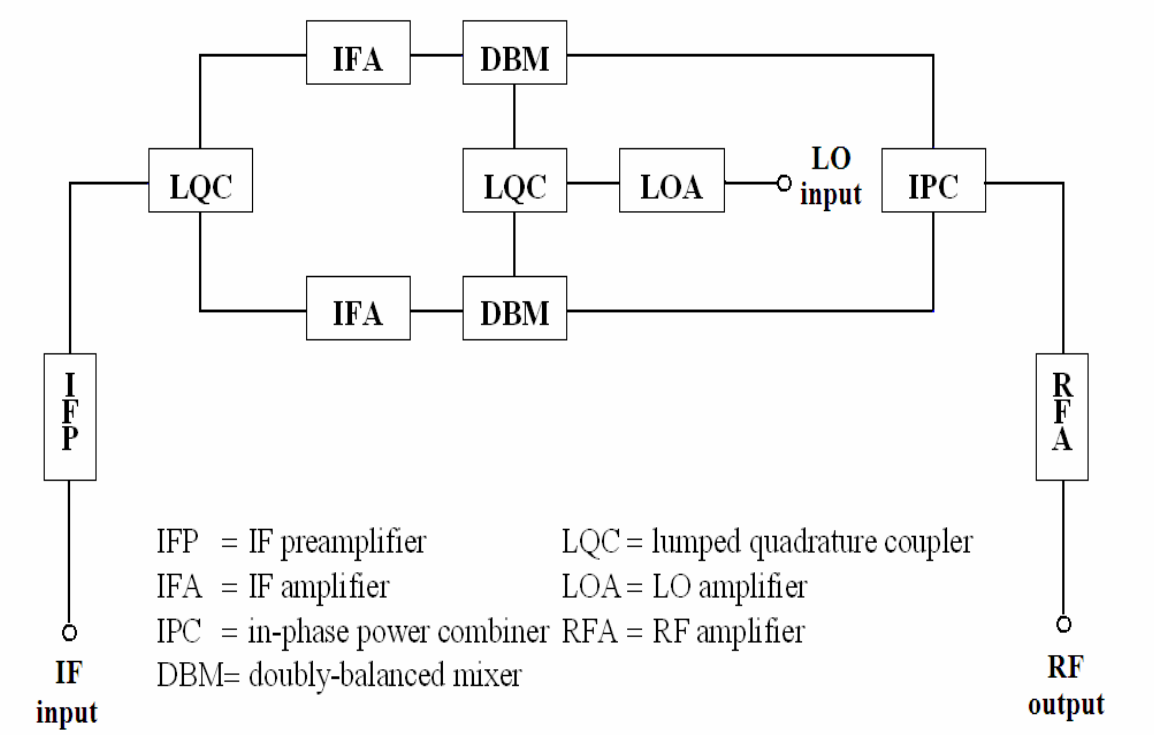

Figure 3.4: Transmitter in terms of its functional blocks

For the sake of characterizing the transmitter quantitatively, it's worth saying that the nodes are 1185, and 98 device ports are present. Therefore the number of nonlinear components in the transmitter is relatively large: 45 FET and 8 diodes. The input 45 MHz IF carrier is phase and amplitude modulated according to the π/4-DQPSK format. The LO signal is sinusoidal with -6 dBm available power at 855 MHz. 4 LO harmonics plus one lower and one upper sideband per LO harmonic are taken into account. The total input IF power is -26 dBm, whereas the total RF power is 23 dBm; consequently, the small signal gain of the transmitter is more than 49dB, and it works at the 4-dB compression point (fig. 3.5). This operation point has been chosen in order to show the effect of the nonlinearities onto the link figures of merit.

In the end, the bit-.rate of the signal propagating through the radiolink is 48.6Kbit/s.

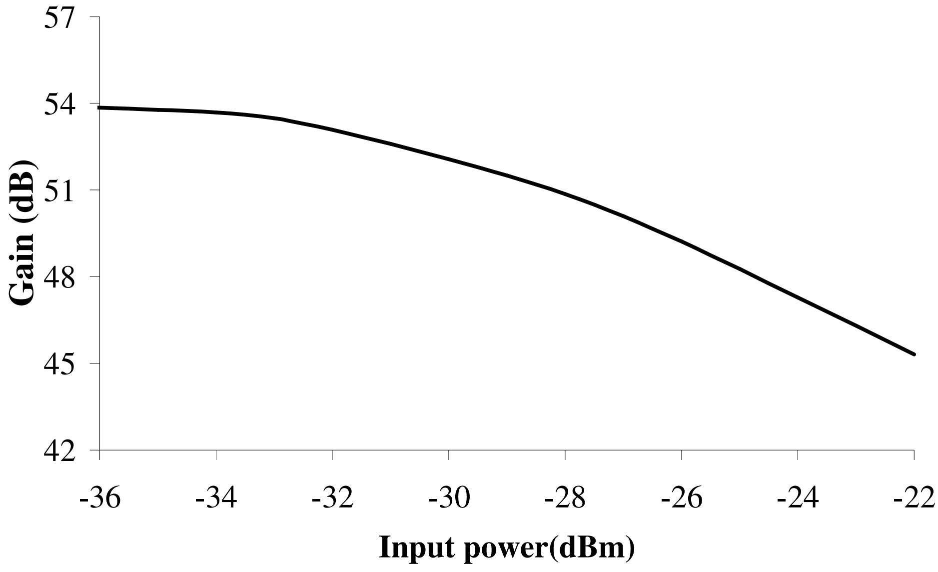

Figure 3.5: Compression gain.

Note that a large number of nonlinear components are present in the transmitter. Besides, it's well known that to obtain an adequate spectral resolution, Δf, we need a large number of envelope sampling instants Δt. In fact,

$$\Delta f = \frac{1}{T} = \frac{1}{N_s \cdot \Delta t} \qquad (3.14)$$

So, combining these two separate information, a consideration comes up: it's not possible to resort to conventional HB approach to analyze the transmitter; for the sake of numerical efficiency, nonlinear analyses must carried out by a model order reduction technique based on Krylov subspaces [13].

3.3.2 TRANSMITTING ANTENNA

The transmitting antenna is a typical radiating element used in mobile communications field. It's a planar inverted-F antenna (PIFA), which is suitable for cell phones at GSM frequencies. It has been modelled for GSM900 and GSM1800 up-link bandwidths, even if the link has been analysed only at 900MHz frequency.

The standard dimensions of the PIFA antenna have been initially calculated through the formula

$$f_{01} = \frac{c}{4(b+c)}$$

$$f_{02} = \frac{c}{4(a+d)} \qquad (3.15)$$

Where f_{01} and f_{02} are the resonant frequencies. Then, an optimization on other seven antenna critical parameters leads to the final results. The seven optimization variables include the shorting pin radius (the same for every pin), the feeding pin radius (one variable), the position of both the feeding pin (four variables) and the gap between the patches.

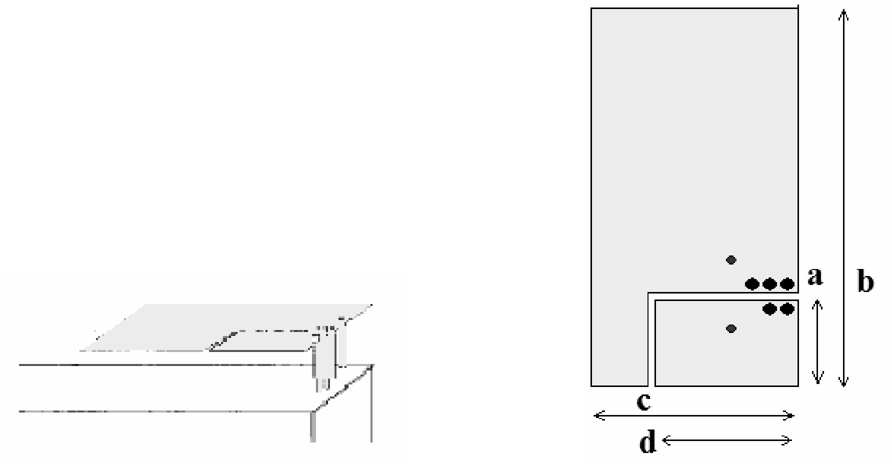

Figure 3.6 : PIFA antenna; a) perspective view; b) top view.

In fig.3.6 a) and b) a perspective and top view of the dual-band antenna are shown.

The dimensions of the proposed antenna are a=50mm, b=14mm, c=32.4mm, d=24.5mm. The gap is 1mm wide.

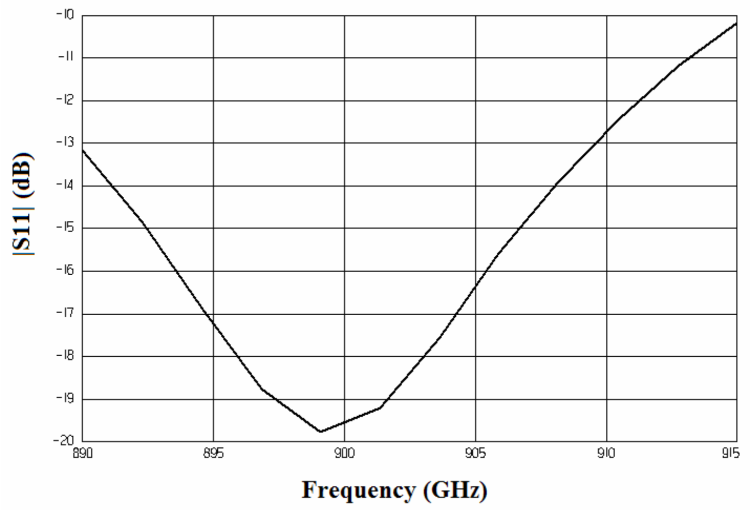

Figure 3.7: |S11| at GSM900 bandwidth

As for the performances, the targeted bandwidth at -6dB (mobile communication standard) is 890-915MHz. The requirements are fulfilled at -10dB threshold, as we can see in fig. 3.7. In fig. 3.8, the reflection coefficient in GSM1800 bandwidth is shown. The targeted bandwidth is 1710-1785MHz. and the requirements are fulfilled at -6dB threshold.

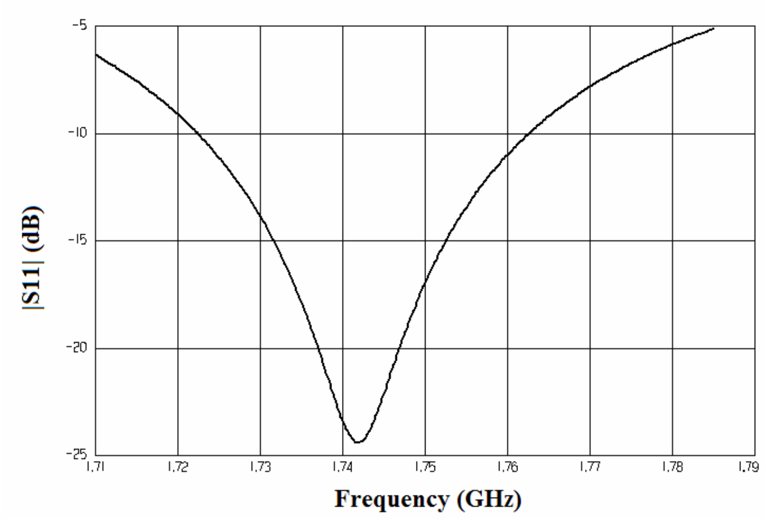

Figure 3.8 : reflection coefficient in GSM1800 bandwidth.

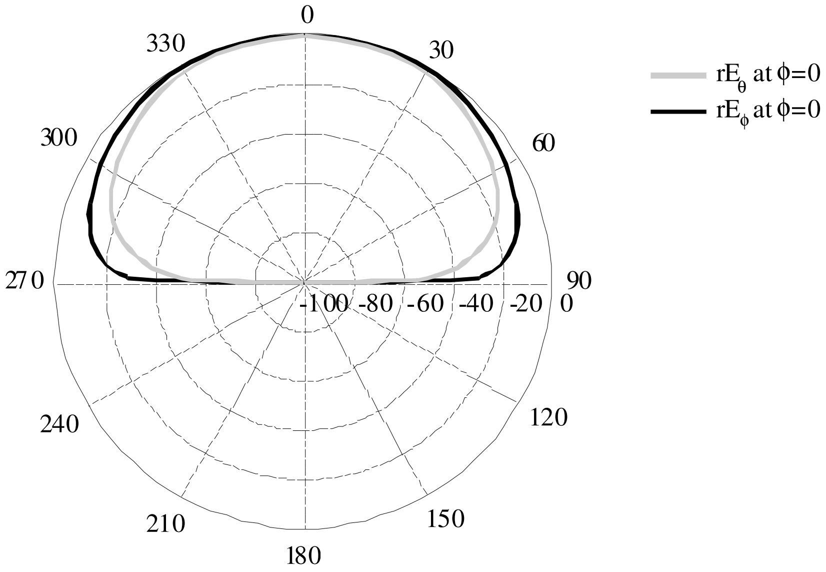

Figure 3.9: E-plane and H-plane radiation patterns of a PIFA mounted on a handset; sweep of θ angle

The typical radiated field of a patch antenna is shown by simulation in fig. 3.9. The electromagnetic tool utilized to calculate the antenna S-parameters and radiated field is the 2D and a half EM tool Ansoft Designer. The total radiated power is 220mW.

This planar antenna, designed in x-y plane, radiates in the broadside direction. The maximum of its radiated field is in the orthogonal direction θ=0, as it may be understood looking at fig.3.9.

3.3.3 RECEIVING ANTENNA

As for the receiving side, a classical vertical dipole array has been chosen (fig. 3.10). The dimension of each dipole composing the array is L =0.475λ. The gain of the proposed array is around 4.4dB , and its radiation pattern is omnidirectional in the plane orthogonal to dipole axis z (fig. 3.11). Such plane is θ=90° plane.

The link is calculated in one direction, which is visualized through the arrow in fig**.** 3.12. The PIFA antenna is rotated towards θ positive direction (90°), so that the new maximum of the radiated field can be found at θ=90°, for both the antenna systems. The distance between the antenna phase centers is 5 km, and free-space propagation is assumed.

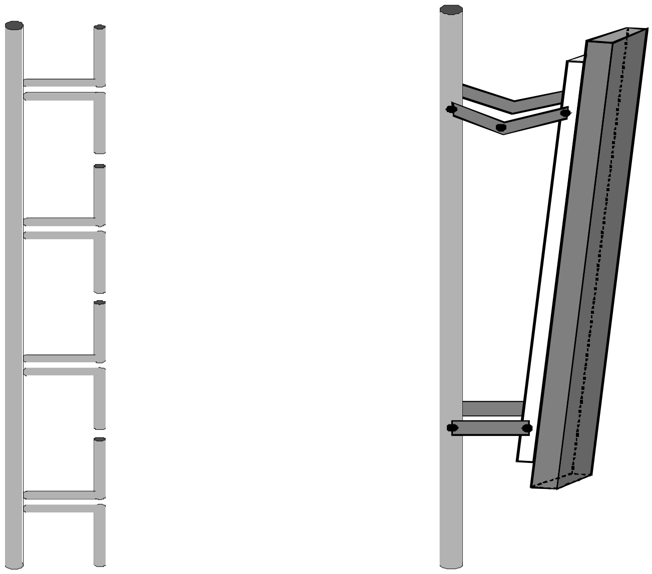

Figure 3.10 : Receiving dipole array; a) four collinear dipoles; b) array mounted on a support

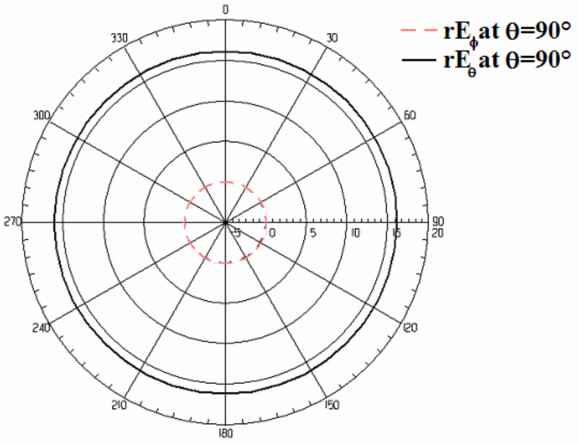

Figure 3.11: H-plane radiation patterns of the dipole array; sweep of ϕ angle

The assumption according which the link is computed only in the maximum power direction is not restrictive; in fact, a general the 3D case study of the link involves only an additional computational effort(i.e. implementation of the same method for every combination of θ and ϕ angles), and no further conceptual issues.

Note that in order to analyze the link in a generic condition (i.e., with an arbitrary orientation of the handset with respect to the link direction), we need not only the radiation diagrams, but also the frequency-dependent polarization and phase of the transmitted far field in any direction of space. It is then clear that EM simulation is a must whenever it is desired to take into account the effects of real-world antenna systems.

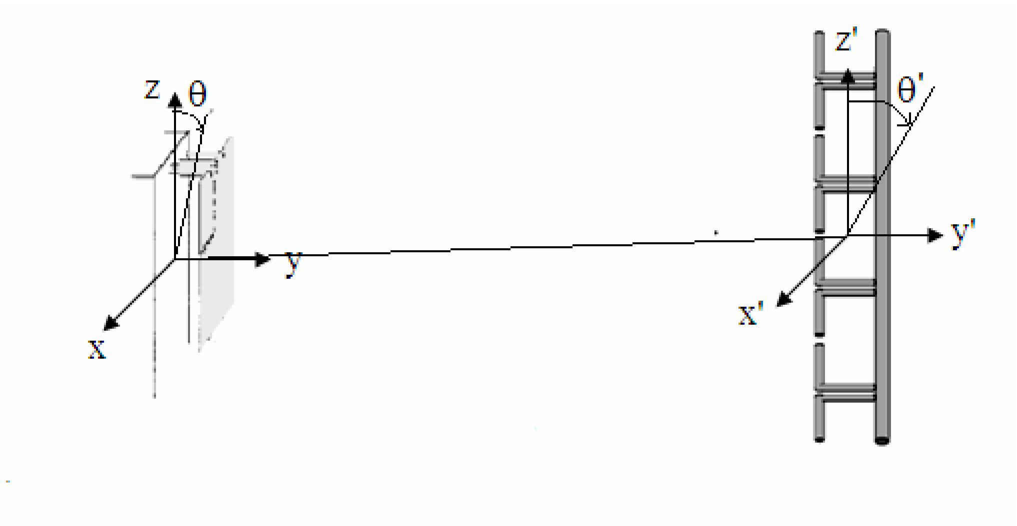

Figure 3.12: Link direction

3.3.4 RECEIVER

After the signal have been received from the 4-ports dipole array, a proper Wilkinson power combined is inserted at the section between the antenna and the receiver.

Subsequently, the receiver presents an architecture similar to that of the transmitter (fig. 3.13). The RF signal, which has total power equal to -80dBm at 900MHz, flows out from the combiner, it is filtered and then amplified thanks to a LNA. After that, an in-phase power divider splits the signal in two different paths, and, before being down converted by the doubly-balanced mixer, each signal is again amplified. The mixer makes use of a 0 dBm local oscillator signal. A lumped quadrature coupler then recombines the two paths into the same signal, which is now at 90MHz intermediate frequency. In the end, the last steps consists in filtering and amplifying the IF output signal. The small signal gain of the receiver is around 60 dB, so that the RF ouput power is equal to -20dBm.

Similarly to the transmitter, the receiver has a large number of nonlinear components; 208 device ports and 1745 nodes confirm the high complexity of this nonlinear system. The analysis carried out is the same performed for the transmitter.

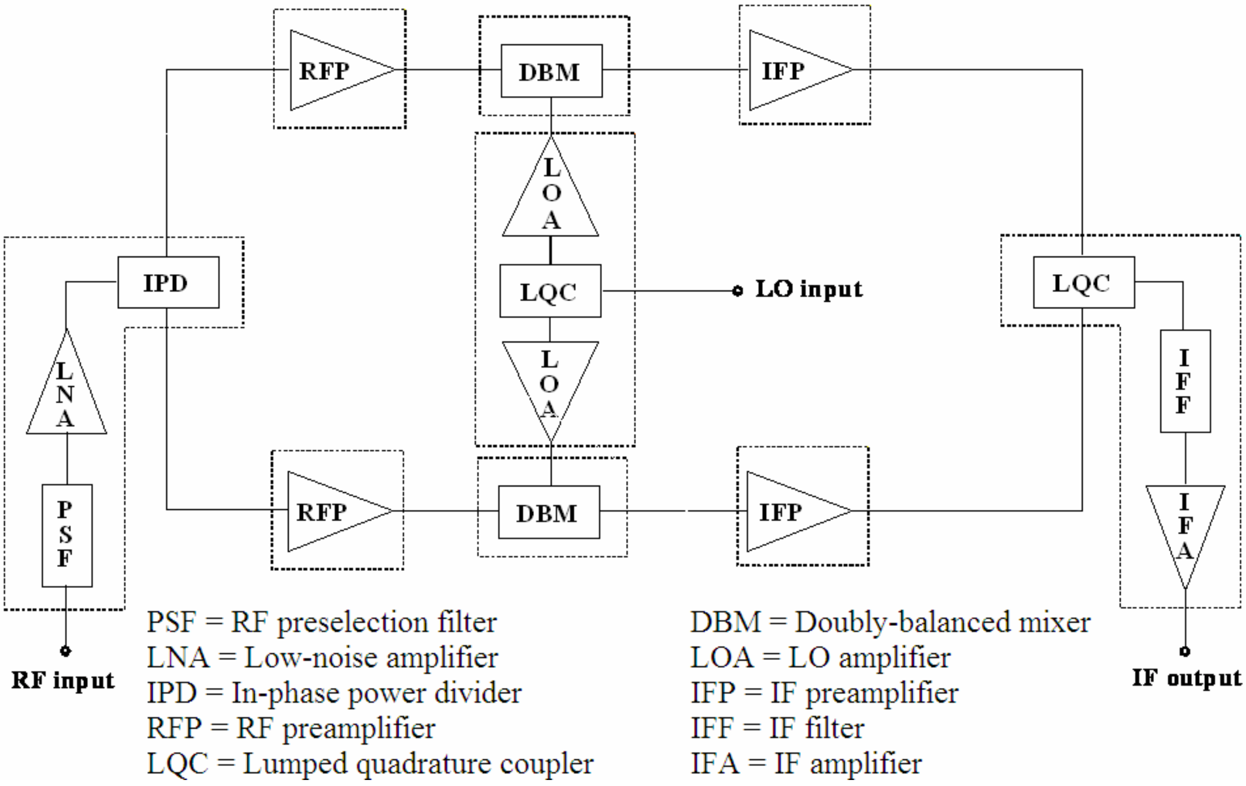

Figure 3. 23 : Block diagram of the receiver

3.3.5 RESULTS

Let us give now some information on simulation time. On a modern PC, the EM analysis of each antenna takes about 50 minutes, and is carried out once for all. A “local” nonlinear analysis of the entire link takes 7 seconds per envelope sampling instant, therefore the entire simulation takes about 530 minutes. This is a reference figure that was obtained by carrying out a conventional Krylov-subspace HB analysis at each of the 4096 sampling instants. Note that model-order reduction techniques become a must in order to keep the CPU time within reasonable limits, because of the problem sizes.

Nevertheless, this reference figure could be significantly reduced thanks to recent algorithmic improvements, such as harmonic balance based on automatic domain decomposition [8]. In addition, previous experience shows that after exactly computing the system response at a number of sampling instants of the order of 100, the available information is sufficient to train a recursive neural network which is able to accurately determine the response at all subsequent instants. In this way very long bit sequences can be cheaply generated.

The numerical results found by means of the Co-simulation technique developed are shown in the following pictures. First of all, figs. 3.14 and 3.15 show a comparison between the in-phase I(t) and quadrature Q(t) components of the normalized signal envelopes at the transmitter input (grey line) and at the receiver output (black line). In both cases, note that the output is clearly distorted; there are two reasons explaining this phenomenon. The first has to do with nonlinearities: since both the transmitter and the receiver operate in nonlinear regions, consequently these devices distort their input signal.

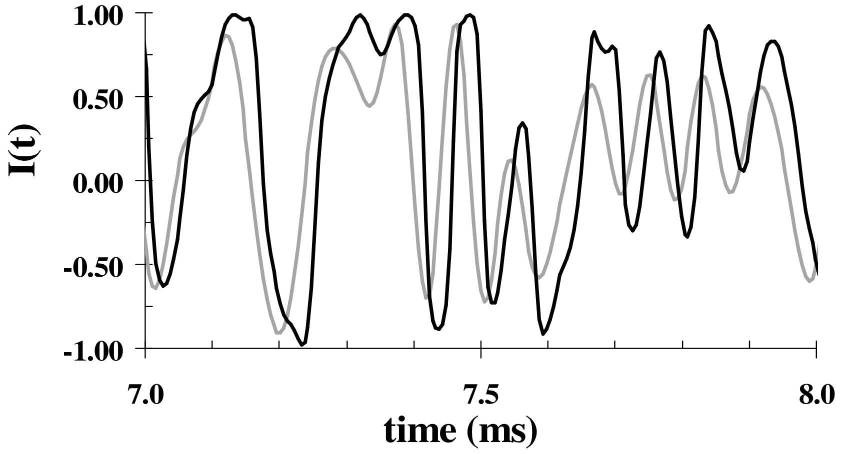

Figure 3.14: In-phase component of the normalized signal envelopes at the transmitter input (grey line) and at the receiver output (black line)

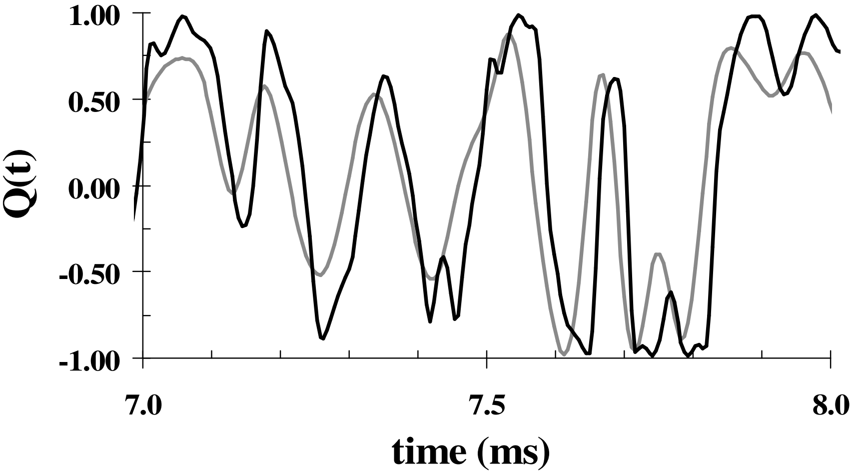

Figure 3.15 : Quadrature component of the normalized signal envelopes at the transmitter input (grey line) and at the receiver output (black line)

The second reason regards the linear part of the link: in particular, since the antenna are frequency selective elements, every frequency of the spectrum of the signal radiated by the antenna is attenuated in a different way; the correspondent time-domain envelope shape is consequently distorted. Finally, note that the distortion presents two natures , on one side nonlinear, on the other linear respectively.

If we analyze now the shapes of the radiated field (fig. 3.16 and 3.17, black lines) for both in-phase and quadrature components, we may understand how this envelope shape is very different from the one at the input at the transmitter (fig. 3.14 and 3.15, grey lines) . Actually, the seeming disagreement is justified by the consideration that the transmitting antenna acts as a signal differentiator, as it appears looking at the $\mathbf{E_T}(\omega)$ formula [18]; in fact, the complex “j” in frequency domain corresponds to a time-domain derivative. Such derivative, traced as a grey line, has been superposed to the radiated field curve, both in fig 3.16 and 3.17 . The agreement is good, so that the above mentioned explication is demonstrated.

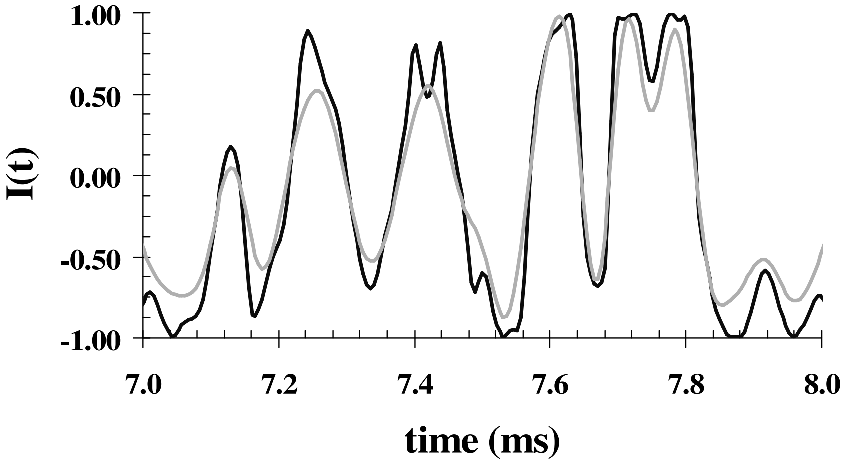

Figure 3.16: In-phase normalized input signal derivative (grey line) and radiated far-field envelopes (black line)

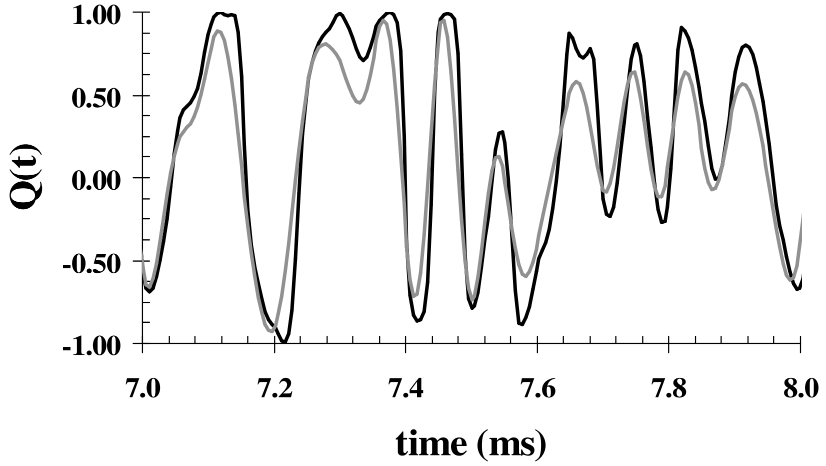

Figure 3.17: Quadrature normalized input signal derivative (grey line) and radiated far-field envelopes (black line)

Other figures of merit to be analyzed are the IF spectra at the transmitter input and at the receiver output. They are shown in figure 3.18 and 3.19. The input voltage spectrum shows a bandwidth equal to 48.6 KHz as expected; obviously, the signal is not distorted, and in fact no sideband can be observed in the spectrum. On the contrary, the output voltage spectrum, shows a typical nonlinear phenomenon, which is the spectral regrowth. This is due to the nonlinearities generated by both front-end and it may be quantified looking through the sidebands. Since the step between the main bandwidth and the first sideband is more than 20dB, we conclude that, as expected, the distortion is not dramatic, but not negligible.

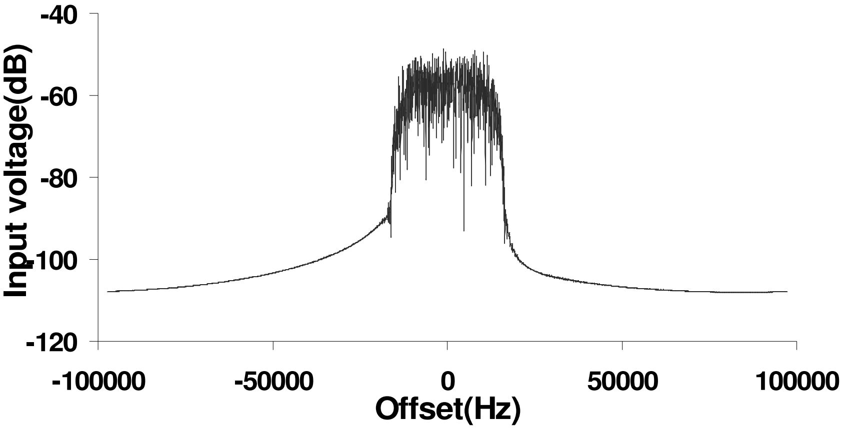

Figure 3.18 : transmitter input spectrum

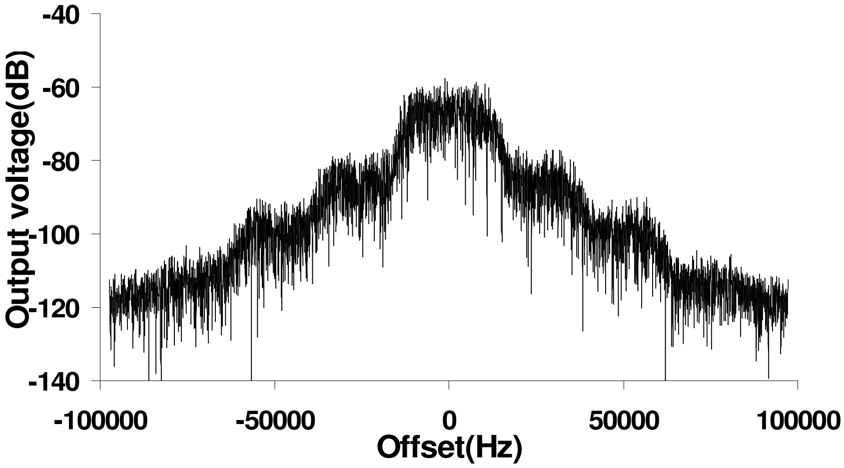

Figure 3.19: Receiver output spectrum

The constellations of the IF input and output signal envelopes, are shown in fig. 3.20 and 3.21 respectively. The input signal shows a clear π/4-DQPSK constellation. Because of the above mentioned distortion, the eight states of the constellation are not visible anymore at the receiver output.

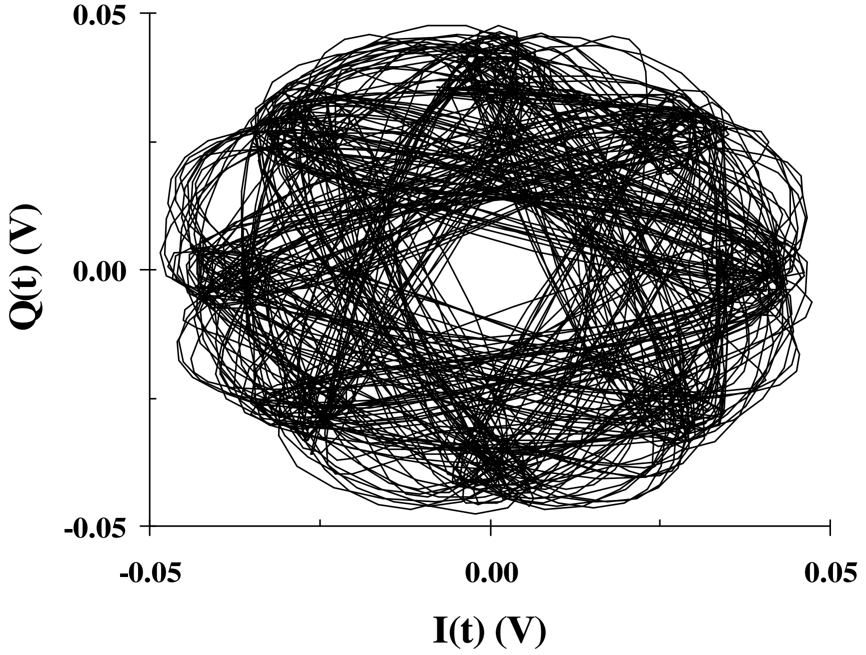

Figure 3.20 : Transmitter input constellation

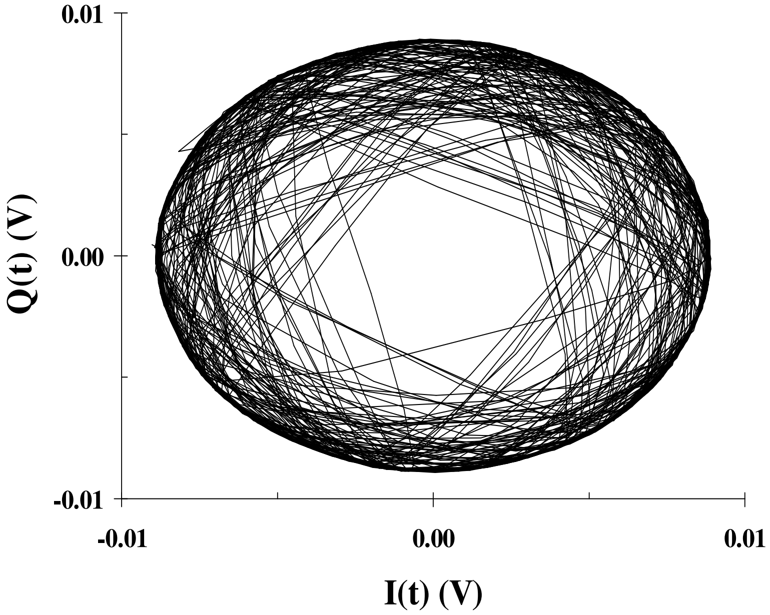

Figure 3.21: receiver output constellation

4.1 INTRODUCTION

This new chapter handles the extension of the general and rigorous link analysis method developed in the previous chapter.

In chapter 3, full-wave EM analysis was limited to the antennas that were treated in the conventional way, i.e., as a one-port components interacting with the transceivers exclusively through their connection ports. In this way field-circuit interactions were not considered. In the next paragraphs I adopt an advanced viewpoint, whereby each antenna may be described as part of an integral linear subnetwork that interacts with environmental EM fields as a whole, thus providing a unified approach to the treatment of ordinary transmission, active and passive interference, and EM compatibility. On the transmitter side, the radiated field is directly related to the transmitter front-end state variables, so that its complex envelope may be directly computed by envelope-oriented harmonic balance when the transmitter IF input is driven by a modulated signal. On the receiver side, the connection is established by deriving the circuit-level receiver excitation through EM theory, starting from the complex envelope of the field incident on the receiver linear subnetwork, which includes the receiving antenna. This is equally valid for the desired (transmitted) field and for any other (interfering) field existing in the receiver environment. In this way the most commonplace quality indicators for the link, such as eye diagrams and power spectra (both with and without interference), can be directly computed. Special attention is devoted to bit-error-rate (BER) calculation, which poses the additional problem of exceedingly long CPU times. In chapter 3, BER calculation was not considered; in these paragraphs it is made possible by resorting to an artificial neural network (ANN) allowing the extension of a relatively short sequence of output samples generated by simulation, both in the absence and in the presence of noise.

The proposed analysis approach is validated by comparing the link performance computed by our technique with the results generated by direct time-domain analysis. This is done for a reference link whose transceivers are small enough (8 transistors overall) to fall within the reach of SPICE-like simulation. A full demonstration of the capabilities of the method is then provided by simulating the transmission of a 16-QAM signal through an RF link with realistic front-end topologies (over 150 transistors), and computing the system BER as a function of drive level and signal-to-noise ratio.

The unavoidable problem of high CPU times is, once again, solved by an envelope-oriented harmonic-balance technique based on Krylov-subspace model-order reduction be efficiently handled.

4.2 DESCRIPTION OF THE SIGNAL FLOW

The description of the co-simulation technique has been given in §3.2. This has been developed from the IF transmitter input to IF receiver output, as shown in figure 3.1. In this paragraph, I will give a description of the simplified approach describing the signal flow from the bit generator to the IF transmitter input, and, similarly, from the IF receiver output to the bit error rate meter. It's a system-level approach, which describes the baseband components in a simplified way.

Let us assume that the link described in fig. 3.1 is the box indicated with the label "IF-RF LINK", which clarifies that the frequencies involved in the block are from IF to RF. In fig. 4.1, an End-to-End block diagram is proposed. From left to right, the first block is the bit generator, whose output is a random bit streams at a fixed bit rate. After that, the bit sequence is transformed into a symbol sequence by a mapper, which is different according to the modulation law used. The digital signal is now ready be transformed into an analog signal, thanks to a modulator. Average power, pulse shaping filter type and center frequency of the output envelope signal have to be specified in this block. The modulator output is the IF complex envelope waveform.

In the receiver chain, the dual components are used in order to transform the receiver IF output to its corresponding bit streams. Successively, a demodulator convert the signal in a symbol sequence, a detector takes the demodulator output and converts it in a bit sequence, and, in the end, a bit error rate meter tests whether the received bit streams corresponds to the transmitted one.

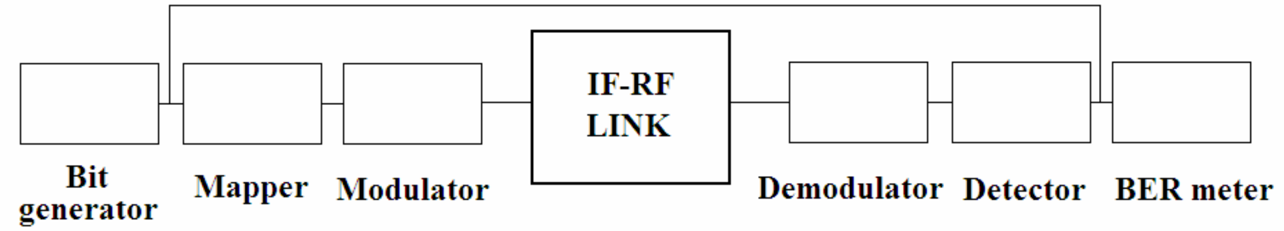

Figure 4.1 : End-to-End link - block diagram

4.3 NEURAL NETWORK APPROACH FOR BER COMPUTATION

BER computation introduces an additional problem, since it is well known that a very large number of symbols of the order of several hundred thousands need be considered in order to obtain meaningful results [19]. This would lead to unrealistic CPU times even with advanced nonlinear simulation algorithms based on model-order reduction techniques. In order to overcome this difficulty, we resort to ANN modeling. The model features that we are looking for are high accuracy and low identification time, as well as the ability to achieve a reliable training making use of a small-size training set. On the other hand, for our present purposes generality is not an issue. In other words, we do not seek a link model allowing the response to be computed under arbitrary input drive conditions, but rather an ANN that can extend a short sequence of output samples generated by simulation *for a specific modulation format and input drive level*. In addition, we are not looking for a cascadable system model, but only for a model of the system operating between known terminations. Referring to [19], we thus use only the input and output voltages and their time derivatives as state variables. In a discrete-time environment this can be simply done by resorting to a recursive ANN of the kind discussed in [20], [21]. Specifically, at a given envelope sampling instant t_n, we feed to the network input the input signal envelope samples computed at t_n and the input and output samples computed at a finite number m of preceding instants, namely, t_{n-1}, t_{n-2}, ….., t_{n-m}. The ANN thus has 2(2m + 1) inputs and 2 outputs, and its I/O maps may be cast in the form

$$\begin{aligned}
I_{out}(t_n) &= F_I\big[I_{in}(t_n), Q_{in}(t_n), I_{in}(t_{n-1}), Q_{in}(t_{n-1}), \ldots\, I_{in}(t_{n-m}), Q_{in}(t_{n-m}), I_{out}(t_{n-1}), Q_{out}(t_{n-1}), \ldots \\
&\quad \ldots\, I_{out}(t_{n-m}), Q_{out}(t_{n-m})\big] \\
Q_{out}(t_n) &= F_Q\big[I_{in}(t_n), Q_{in}(t_n), I_{in}(t_{n-1}), Q_{in}(t_{n-1}), \ldots I_{in}(t_{n-m}), Q_{in}(t_{n-m}), I_{out}(t_{n-1}), Q_{out}(t_{n-1}), \ldots \\
&\quad \ldots\, I_{out}(t_{n-m}), Q_{out}(t_{n-m})\big]
\end{aligned} \tag{4.1}$$

where $I_{in}(t) + jQ_{in}(t)$ and $I_{out}(t) + jQ_{out}(t)$ are the complex envelopes of the input and output IF signals, respectively. The nonlinear functions F_I, F_Q are implemented by a standard feedforward three-layer perceptron [20], and the total number of state variables is defined by the integer m. In principle, the optimum value of m should be determined by the embedding process [19], whose application to a large system would require long CPU times. However, the very stringent restriction imposed on the input excitation (fixed modulation and power) justifies the heuristic conjecture that only a small number of internal states be excited, and consequently a small number of state variables be needed. Thus only m = 1, m=2 and m=3 have been tested for several circuits, and it has been found that m = 1 and a set of several hundred samples appear to be sufficient to train an ANN that is able to accurately determine the link response to the specific selected excitation at all subsequent instants. A number of hidden-layer neurons of the order of 20 to 30 are normally sufficient to achieve excellent results. Training is then performed by the Levenberg-Marquardt algorithm coupled with a stop criterion based on cross-validation in order to minimize the generalization error [21].

4.4 NUMERICAL EXAMPLE

A representative numerical example on the application of the method will be explained in the next two paragraph. In the first one, an end-to-end characterization of the link under a modulated drive approximated by a 2048 bit stream is shown. In the second paragraph, we will treat the analysis extension to a 800,000 bit sequence.

4.4.1 END-TO-END CHARACTERIZATION FOR A 2048-BIT SEQUENCE

A random 2048-bit sequence at a fixed bit rate (5.12 Mb/sec) is first generated. This stream is the 16-QAM mapper input. In this way, we may obtain a 16 points constellation, which can be seen in terms of phase trajectories in fig. 4.2. The correspondent eye diagram is pictured in fig. 4.3.

The modulator takes on the symbol stream and its output is the complex envelope representation of the modulated signal at center frequency $f_{c.}$. The oversampling is now 8 samples per symbol (2 samples per bit), a typical value to characterize a waveform in the time-domain. The modulator in terms of its functional blocks is shown in fig. 4.4. In particular, a pulse shaping filter is used into the modulator to avoid intersymbol interference, which is a quite annoying phenomenon appearing for wideband signals. In fact, when the signal bandwidth becomes larger than the channel bandwidth, as in the case study, the channel starts to introduce distortion to the signal. This distortion is usually seen as intersymbol interference.

After the pulse shaping filter, a baseband to IF conversion is performed, through a nonlinear multiplication with a signal at f_c center frequency. At this stage, this signal is taken on by the transmitter.

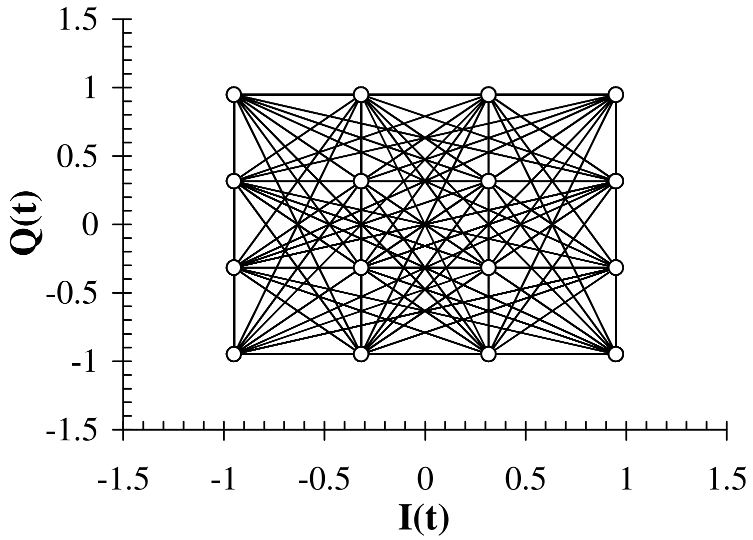

Figure 4.2 :16-QAM constellation

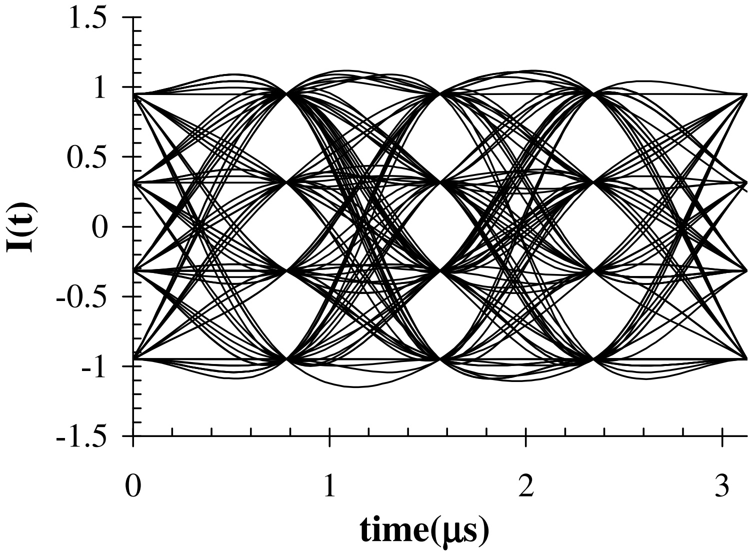

Figure 4.3 : Input eye diagram

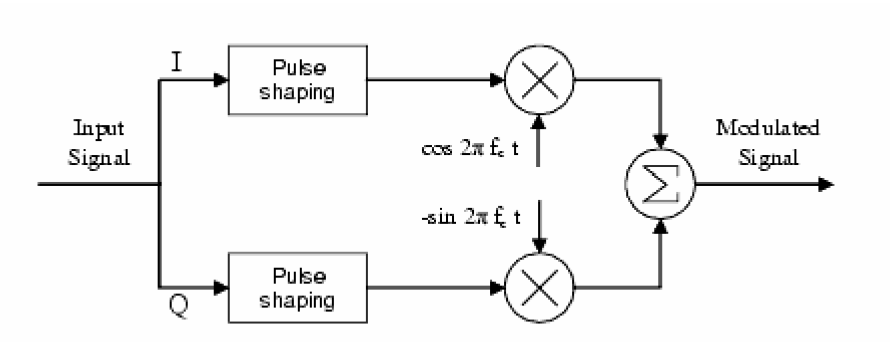

Figure 4.4: Modulator scheme

The transmitter topology is the one used in fig. 3.5. The input 45 MHz IF carrier is phase- and amplitude- modulated, but now a wide-band (5.12 Mb/sec) analysis is carried out with a 16-QAM format. The total input IF power is -22 dBm. The LO signal is sinusoidal with -6 dBm available power at 855 MHz. 4 LO harmonics plus one lower and one upper sideband per LO harmonic are taken into account in each harmonic balance analysis. The link distance is D = 5 km, and the total radiated power is 220 mW.

In figs. 4.5 and 4.6 we plot the in-phase and quadrature components of the transmitter IF

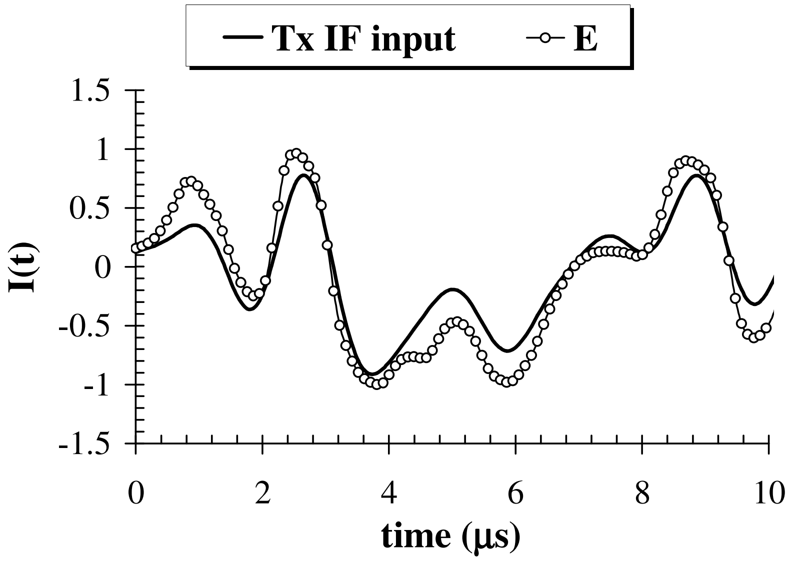

Figure 4. 5 : Normalized in-phase components of the transmitter input signal and of the far field complex envelopes (50-bit slot).

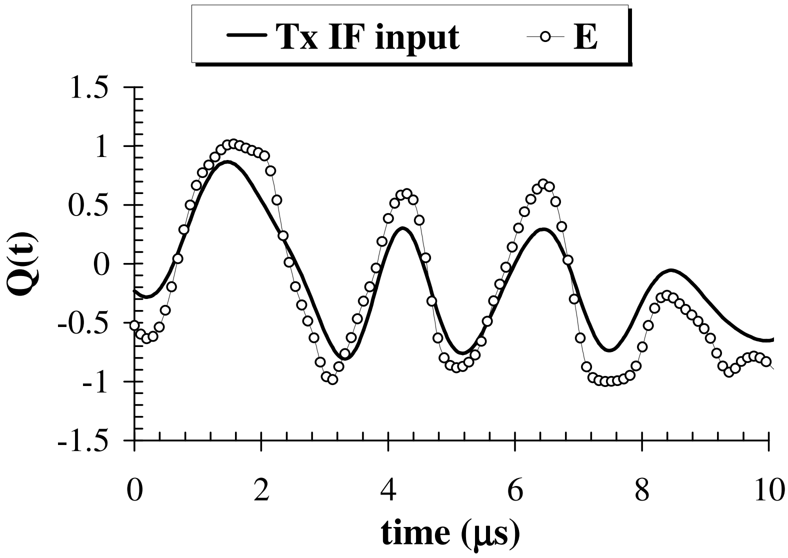

Fig. 4.6 : Normalized quadrature components of the transmitter input signal and of the far field complex envelopes (50-bit slot).

input signal and of the far field complex envelopes in a 10 μs time slot, showing distortion in the transmitting chain. For the sake of comparison, the field envelope in these figures has been shifted by the total group delay between the front-end input and the field observation point.

A block diagram of the receiver front end is given in fig. 3.14. The circuit is arranged in an image-rejection configuration and has a total of 208 device ports and 1745 nodes. The output IF is 90 MHz and the small-signal gain is 60 dB. At this stage, the in-phase and quadrature waveforms are plotted in figs. 4.7 and 4.8, where the combined effects of linear and nonlinear distortion is evident. Moreover, in fig. 4.11 the power spectrum is shown; note that the spectral regrowth in the sidebands, due to the nonlinearities, is significant.

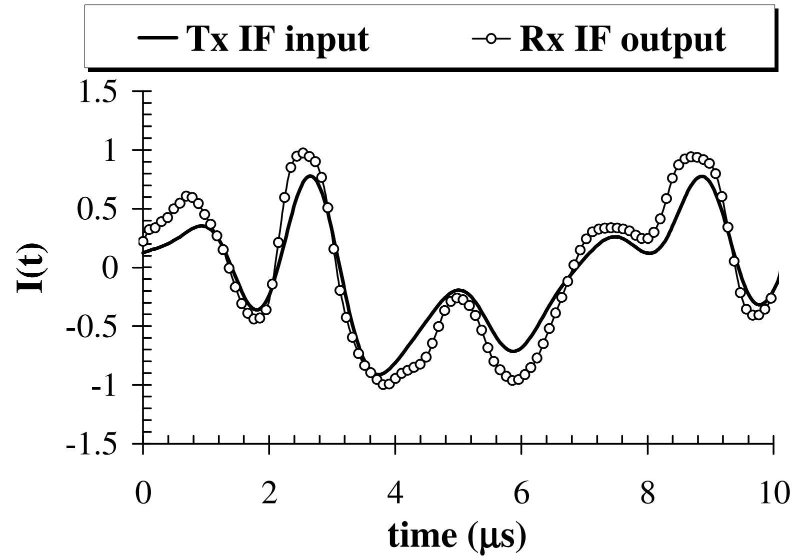

Figure 4.7 : Normalized in-phase components of the link I/O signal envelopes (50-bit slot).

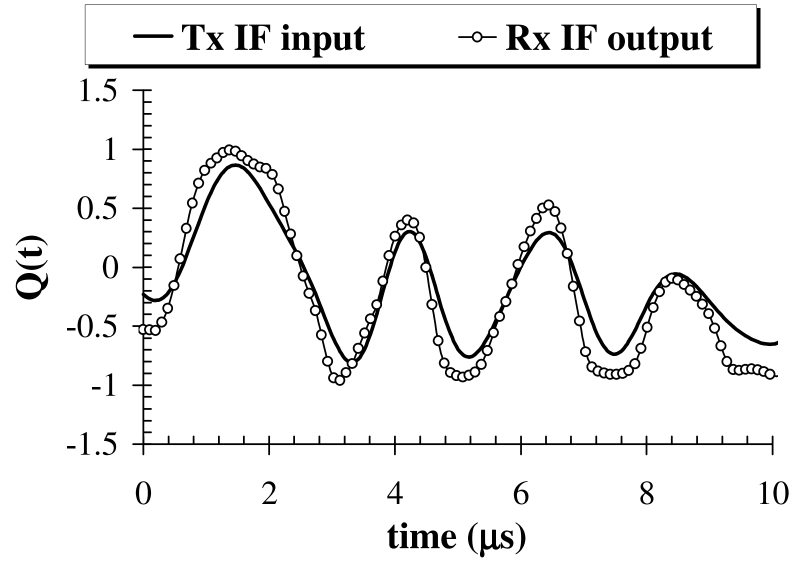

Figure 4.8 : Normalized quadrature components of the link I/O signal envelopes (50-bit slot).

At this stage, a new step involves the system-level simulation. The 90 MHz IF signal is demodulated by a coherent correlating demodulator. Its output consists in a symbol stream.

After the demodulator, a 16-QAM detector transforms the symbol sequence in a bit stream; finally, the received sequence can be compared to the transmitted one, in order to compute the link bit error rate.

For the transmitter front end the with ordinary Krylov-subspace methods, the average CPU time required for the overall nonlinear analysis is again 7 seconds per envelope sampling instant on a DELL Latitude C480 PC.

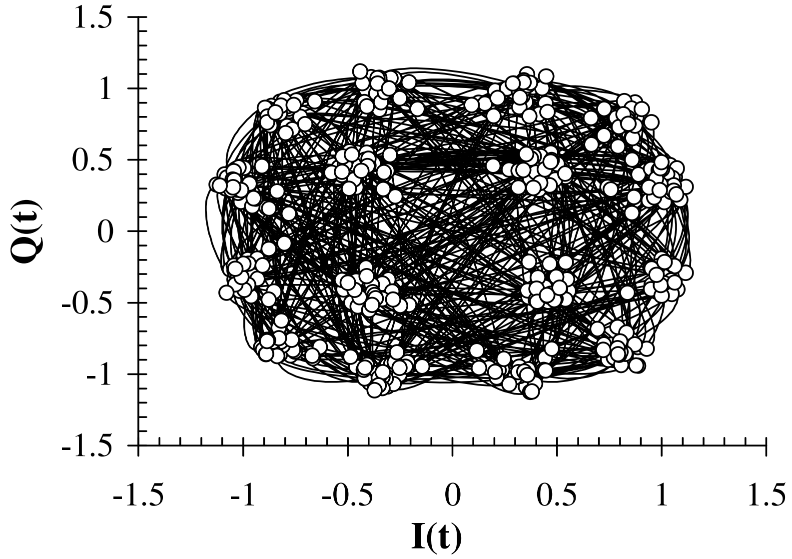

Figure 4.9 : Phase trajectories of the link output signals.

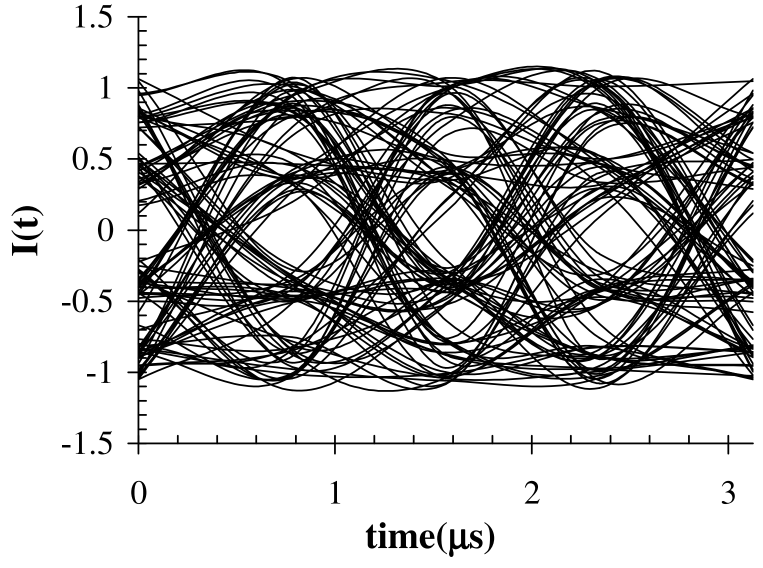

Figure 4.10: Eye diagrams of the link output signals

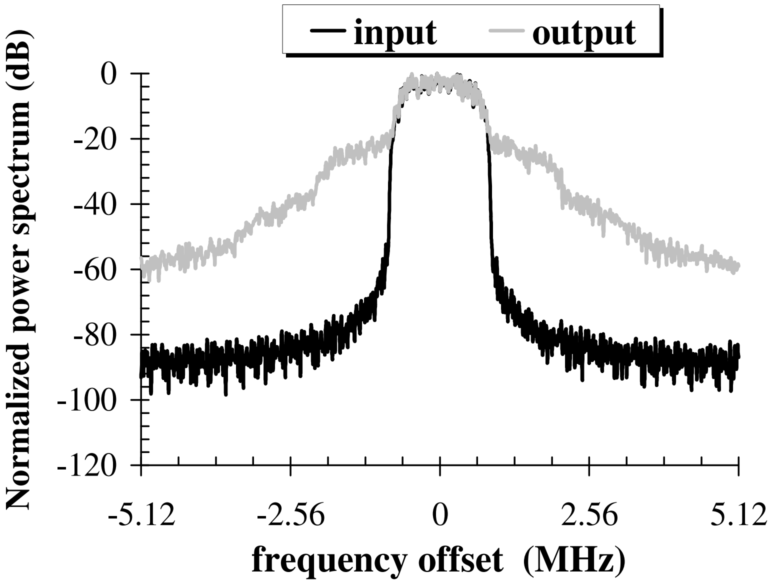

Figure 4.11: Normalized power spectra of the link I/O signals

4.4.2 BER COMPUTATION FOR A 800000-BIT SEQUENCE

In order to demonstrate the method explained in §4.3, we first carry out the BER calculation for the link described in §4.4 in the absence of noise. The input sequence at the transmitter IF port is a sequence of 200,000 symbols which are sampled at a rate of 8 points per symbol, for a total of 1.6 million samples that would approximately require 11 million s of CPU time on a 3 GHz PC. Following the proposed procedure, for each input power level the simulation is stopped after 512 symbols or 4096 samples, and takes about 28600 s.

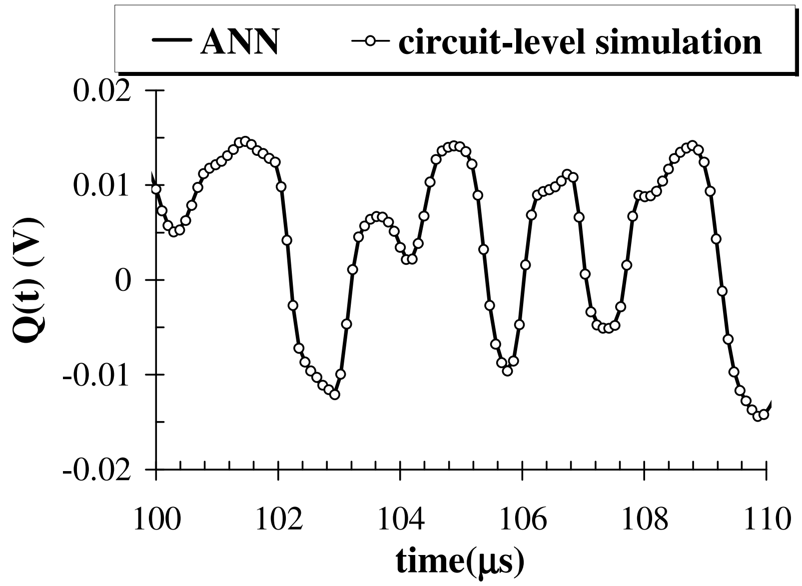

Figure 4.12 : Comparison between ANN and in-phase component of the link output signal envelope (50-bit slot)

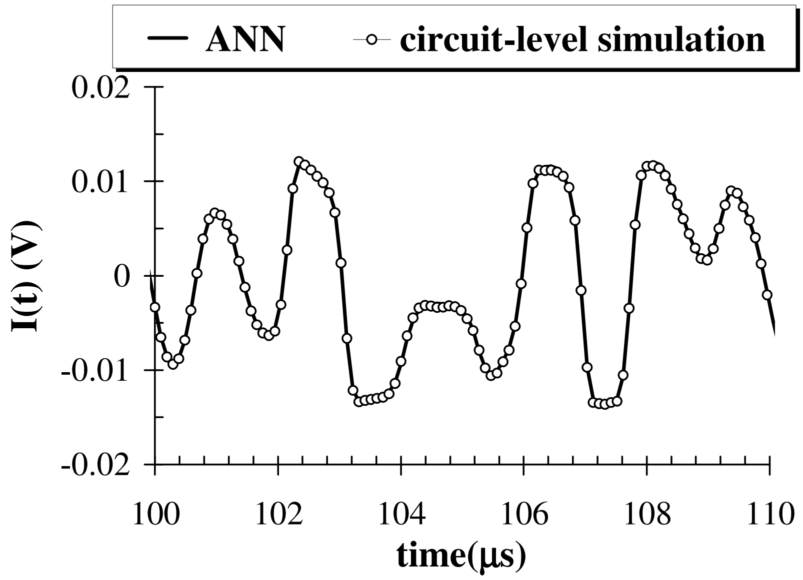

Figure 4.13 : Comparison between ANN and quadrature component of the link output signal envelope (50-bit slot).

A set of 512 consecutive samples extracted from this sequence is used as the training set for an ANN with 21 hidden neurons, and all the remaining samples are used for validation. The overall training and validation time is about 7 s. The validation results are reported in figs. 4.12, 4.13 showing a comparison between the in-phase and quadrature components of the receiver IF output voltage envelope computed by simulation and by the ANN model in a 50-bit slot *extracted from the validation set*, but not belonging to the training set. At an input signal power level of -22 dBm across the channel, the RMS error vector magnitude (EVM) has been calculated. Let us assume that z_k is the k-sample of the complex envelope signal, s_k the ANN k-sample and N the number of samples; EVM_{RMS}, defined in (4.2), has been found to be less than 1% .

$$EVM_{RMS} = \frac{1}{N}\sqrt{\frac{\sum_{k=1}^{N} | z_k - s_k |^2}{\sum_{k=1}^{N} | z_k |^2}} \cong 0.97\% \qquad (4.2)$$

In order to double-check this result, we carried out a similar comparison in a further time slot of the same duration, but located very far away from the training set, i.e., after *one million samples* have elapsed since the beginning of the observation. The results are reported in figs. 4.14, 4.15 showing that the agreement is still perfect. These comparisons are believed to provide an indirect but very credible confirmation of our heuristic conjecture. Note that this is in reality the only proof we need, since we are not interested in the system response to a different excitation. Furthermore, it is worth observing that the range of values that the I/O signals take on within the training sequence remains substantially stable even after a very long time. This implies that the ANN does never work in an extrapolating mode, but always in the canonical interpolating mode.

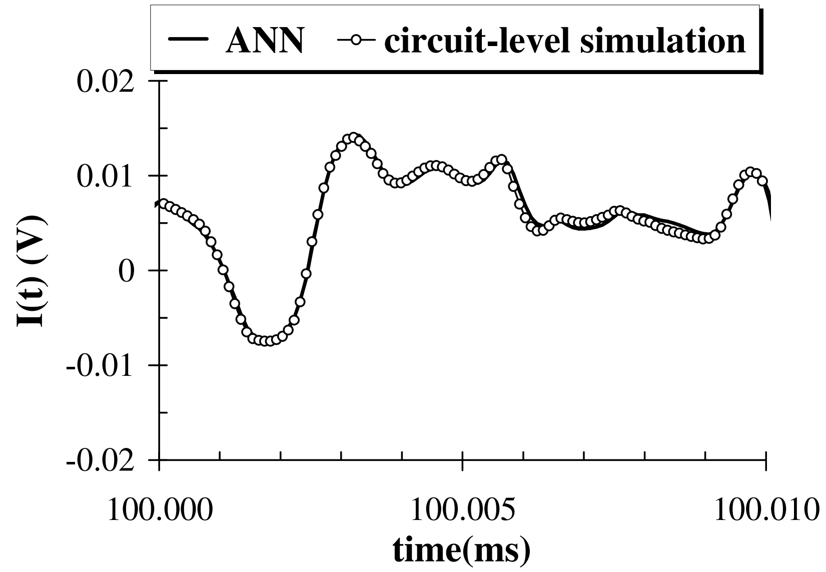

Fig. 4.14: Comparison between ANN and in-phase component of the link output signal envelope (50-bit slot located 1 million bits apart from the time origin).

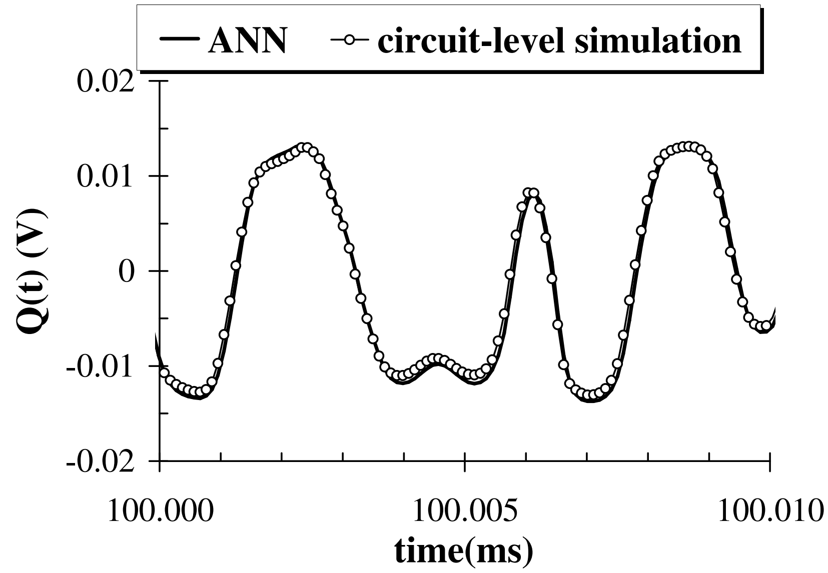

Fig. 4.15: Comparison between ANN and circuit-level results in terms of quadrature component of the link output signal envelope (50-bit slot located 1 million bits apart from the time origin).

At this stage, the computation of 1,600,000 samples by the ANN then takes about 590 s, and the BER is estimated by direct I/O comparison. The whole procedure is then repeated at several input power levels to generate the distortion-related BER curve given in fig. 16. Here, the -27 dBm power level roughly corresponds to the receiver 2.5-dB compression point, while the -18 dBm level corresponds to a strong compression of about 12 dB.

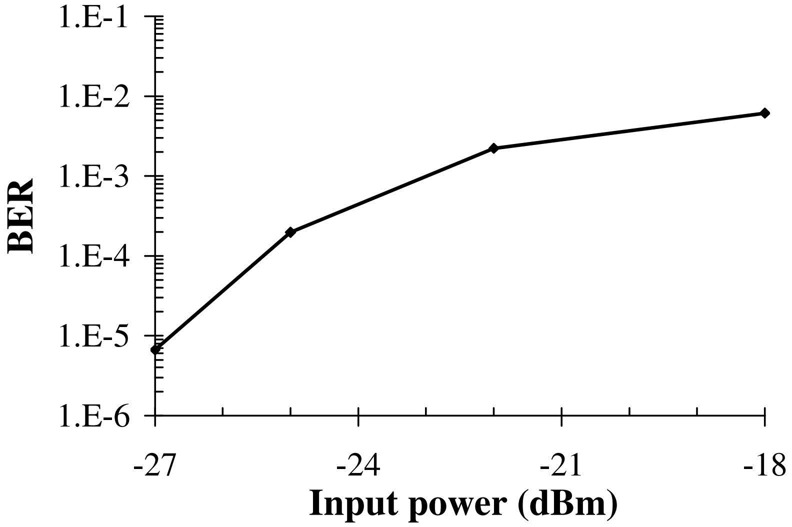

Figure 4.16 : Link BER vs. input power level.

We now show that the same procedure can also be applied to BER computation in the presence of noise. Performing an accurate and general link noise analysis is a delicate and complex task, and is out of the scope of this paper, so for the time being we will limit ourselves to the consideration of a simple additive white Gaussian noise (AWGN) model. This model can be simply implemented by introducing an additional noise current source connected in parallel to J_R (which exactly corresponds to J_{RA} quantity, defined in §3.2.3) at the receiving antenna port. The constant spectral density of this source (in A^2s/rad) will be denoted by G. According to classic noise theory [22], if we now subdivide the signal band into a relatively large number, say 2H + 1, of sufficiently small intervals $\Delta\omega$, the noise components whose spectrum fall inside one of such intervals may be represented by a pseudo-sinusoidal signal with deterministic amplitude and frequency, but random phase. The noise signal source may thus be represented in the form [22]

$$J_N(t) \approx \sqrt{2G\Delta\omega} \sum_{h=-H}^{H} \cos\left[(\omega_{RF} + h\Delta\omega)t + \phi_h\right] \tag{4.3}$$

where the ϕ_H are independent random variables with uniform probability distribution over the interval [0 2π]. (4.3) is obviously equivalent to a sinusoidal carrier of angular frequency ω_{RF} phase- and amplitude-modulated with random modulation laws. Specifically, if we write

$$J_N(t) = I_N(t)\cos\omega_{RF}t - Q_N(t)\sin\omega_{RF}t \tag{4.4}$$

the in-phase and quadrature components of the complex envelope are given by

$$\begin{aligned} I_N(t) &= \sqrt{2G\Delta\omega}\sum_{h=-H}^{H}\cos(h\Delta\omega t + \phi_h) \\ Q_N(t) &= \sqrt{2G\Delta\omega}\sum_{h=-H}^{H}\sin(h\Delta\omega t + \phi_h) \end{aligned} \tag{4.5}$$

It has been found that very good results (in the statistical sense) can be obtained with H of the order of a few hundreds and a sequence of ϕ_H values extracted by a random number generator [23].

Suppose that we want to evaluate the link BER at a fixed input power level, say -27 dBm, and for several values of the signal-to-noise ratio. The latter is defined as E_S/N_O, where E_S is average received energy per symbol, and N_O is the noise power spectral density $2\pi R_O G$ (in W/Hz) with a system impedance level $R_O = 50\ \Omega$. For this purpose the link is modeled as the cascade connection of two ANN's of the kind described above. The input to the first ANN is the transmitter IF input envelope, while its output is the receiver exciting source envelope defined by (3.13).

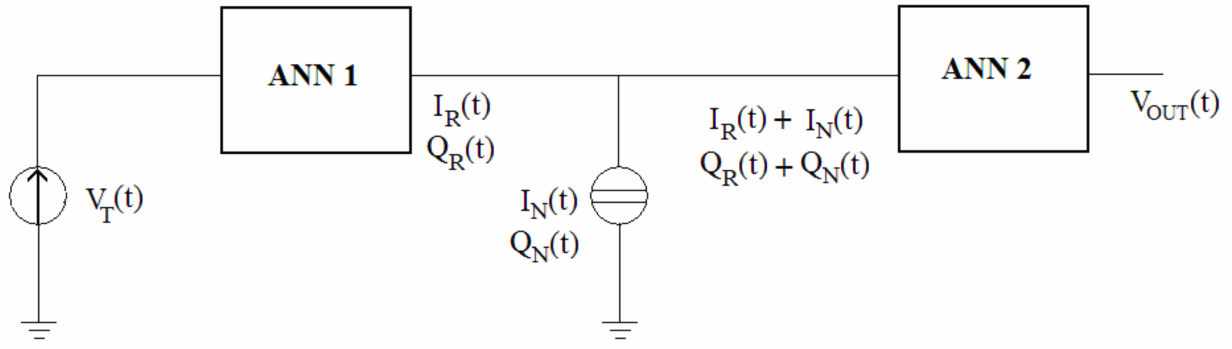

Figure 4.17 : Representation of the two cascadable ANN.

Its map is thus given by (4.1) with $I_{out}(t)$, $Q_{out}(t)$ replaced by $I_R(t)$, $Q_R(t)$, respectively, where $I_R(t)=\mathcal{Re}\{J_{RA}(t)\}$ and $Q_R(t)=\mathcal{Im}\{J_{RA}(t)\}$. The input to the second ANN is the superposition of signal (3.13) and noise (4.5), while its output is the receiver IF output envelope. Its map is thus again given by (4.1) with $I_{in}(t)$, $Q_{in}(t)$ replaced by $I_R(t) + I_N(t)$, $Q_R(t) + Q_N(t)$, respectively. The first ANN is trained once for the given input power in the way discussed above.

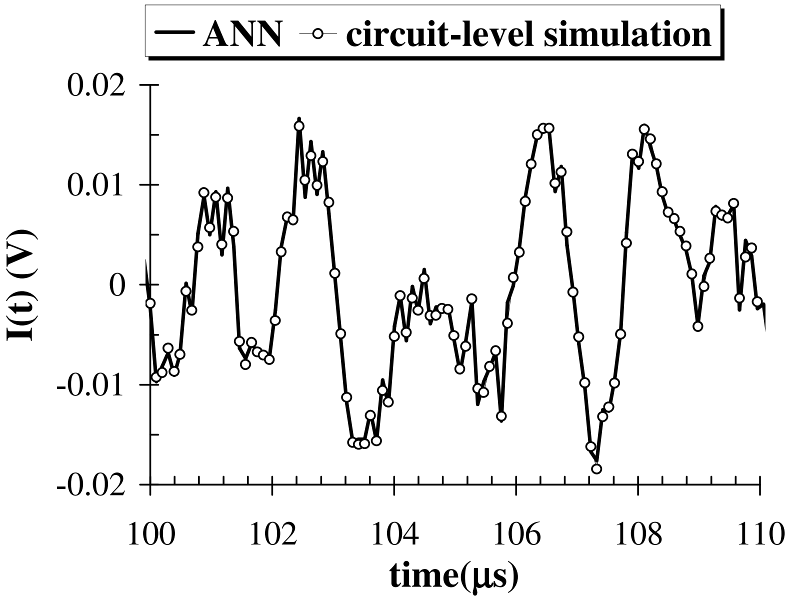

Fig. 4.18 : Comparison between ANN model and circuit-level results in terms of in-phase components of the link output signal envelope for an AWGN channel (50-bit slot).

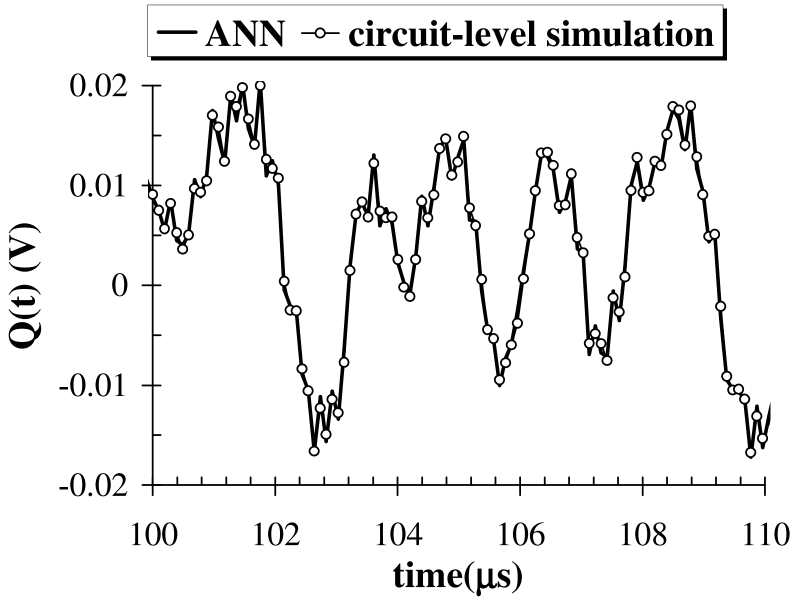

Fig. 4.19 : Comparison between ANN model and circuit-level results in terms of quadrature components of the link output signal envelope for an AWGN channel (50-bit slot).

The second ANN training proceeds in a similar way, but is repeated for each different noise level. As a representative example, the validation results for the entire noisy link are reported in figs. 4.18, 4.19 showing a comparison between the in-phase and quadrature components of the receiver IF output voltage computed by simulation and by the twin-ANN model.

The signal-to-noise ratio is 20 dB, and an EVM_{RMS} error of less than 6% is obtained in this case, showing a satisfactory agreement in the presence of noisy waveforms, as well. Finally, fig. 4.20 shows the BER estimated in this way as a function of E_S/N_0.

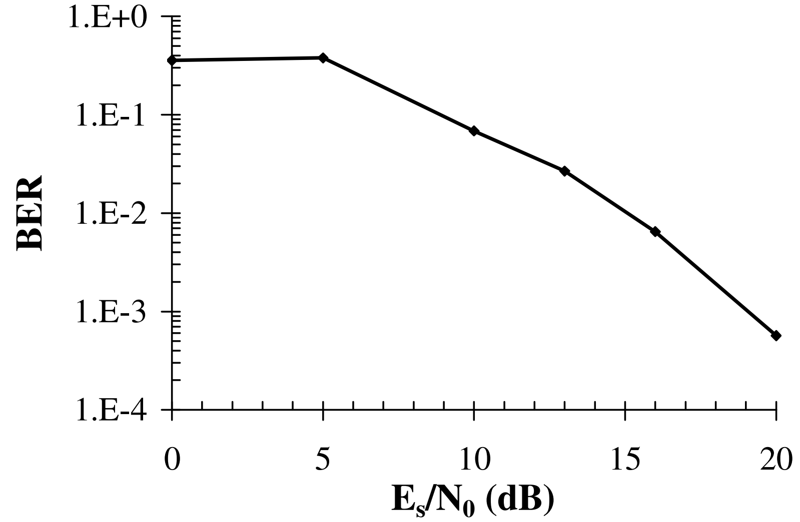

Fig. 4.20 : Link BER vs. signal-to-noise ratio evaluated by the ANN model at an input power level of -27 dBm.

4.5 VALIDATION OF THE ANALYSIS APPROACH

In order to validate our analysis approach, in this section we present a comparison between the results of a link analysis performed by the proposed method, and by a SPICE-like time-domain technique. Time-domain analysis provides a reliable and well-established reference, but is computationally slow when digitally modulated RF carriers must be handled. For validation purposes we thus consider a relatively small-size problem. The transmitter consists of an active up-converter (one FET) followed by a three-stage power amplifier. The receiver includes a low-noise amplifier, an active down-converter, and a two-stage IF amplifier. The total number of transistors in the link is thus equal to 8 (16 device ports overall). In addition, we choose as the transmitting and receiving antennas two identical collinear thin dipoles that can be mathematically analyzed in closed form [24]. The front-end topology is the one represented in fig. 3.3 c) both on the transmitter and on the receiver side, so that the link transfer matrix reduces to a scalar B(ω) which can be computed analytically. The antennas and the reference frames are schematically illustrated in fig. 4.21.

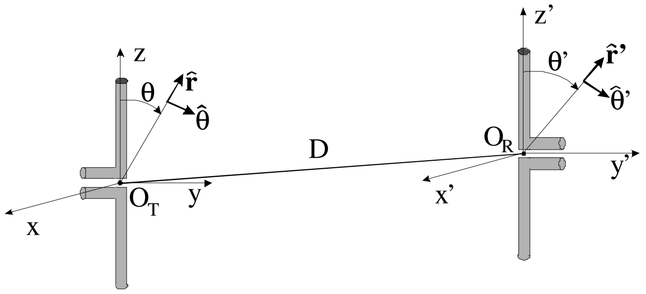

Figure 4.21 : Dipoles as transmitting and receiving antennas.

Referring to §3, when the transmitting antenna is excited by a unit-voltage sinusoidal source of angular frequency ω, its input current is numerically coincident with the dipole radiation admittance $Y_t(\omega)$. The radiated far field is then given by

$$\mathbf{E_T}(r, \theta, \varphi; \omega) = j\eta\, Y_t(\omega)\frac{\exp(-j\beta r)}{2\pi r}\; \frac{\cos(\beta\, L\cos\theta) - \cos\beta L}{\sin\beta L\, \sin\theta}\; \hat{\boldsymbol{\theta}} \tag{4.6}$$

where 2L is the dipole length. Equation (3.1) then yields

$$\begin{aligned} A_\vartheta(\theta', \varphi'; \omega) &= j\,\frac{\eta}{2\pi}\cdot\frac{\cos(\beta L\cos\theta') - \cos\beta L}{\sin\beta L\,\sin\theta'}\, Y_t(\omega) \\ A_\varphi(\theta', \varphi'; \omega) &= 0 \end{aligned} \tag{4.7}$$

In turn, when the receiving dipole is excited by a unit-voltage sinusoidal source, by a similar argument we get the same coefficients in (4.7), but with $Y_{RA}(\omega)$ instead of $Y_t(\omega)$.

Referring to fig. 3.13, in the link direction we have $\theta_I = -\theta_I' = \pi/2$, so that by (4.7) the link transfer function coming out from (3.12) becomes

$$B(\omega) = -j \, \frac{\eta \lambda}{2} \, \frac{\exp(-j\beta L)}{D} \left[\frac{Y_t(\omega) \, (1 - \cos \beta L)}{\pi \sin \beta L} \right]^2 \tag{4.8}$$

If we now connect the transmitter to the first dipole and the receiver to the second one, we are in a position to carry out the link simulation in either of two different ways, i.e., by the EM-based all-numerical procedure discussed in chapter 3 , and by time-domain analysis using SpectreHDL.

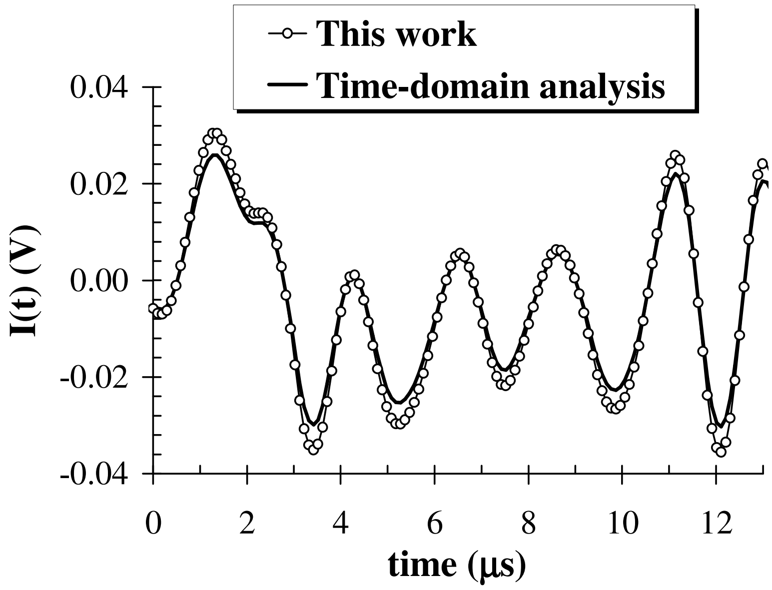

Figure 4.22: Comparison between in-phase components of a link output signal envelope computed by nonlinear/EM co-simulation and by time-domain analysis (64-bit slot).

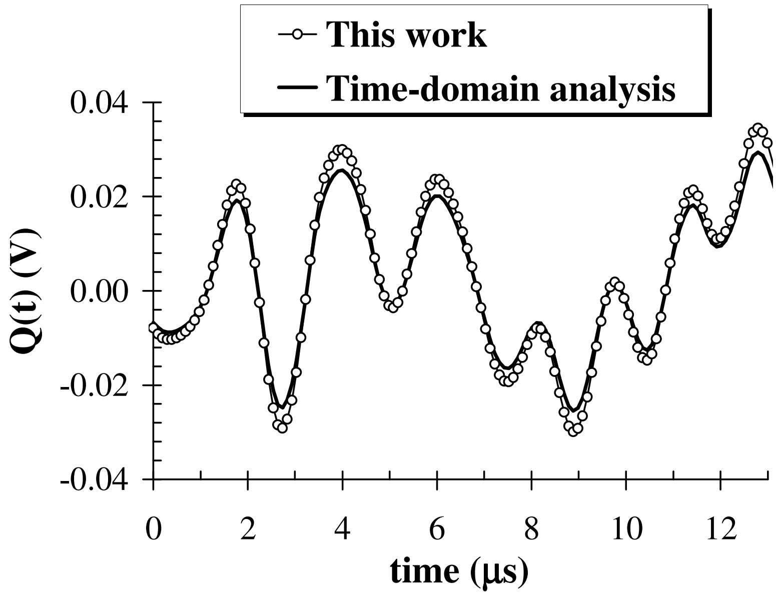

Figure 4.23 : Comparison between quadrature components of a link output signal envelope computed by nonlinear/EM co-simulation and by time-domain analysis (64-bit slot).

For SpectreHDL, we use the analytic channel description provided by (4.8), and perform frequency-to-time-domain conversion by the procedure discussed in [25]. In this way, completely independent algorithms are used in the two simulations Making use of the 16-QAM input signal defined in §4.4, we obtain the in-phase and quadrature components of the output signal envelope displayed in figs. 4.22, 4.23. The waveforms generated by the two calculations are very close to each other except for minor details, with an RMS error of about 3 x 10^{-4}.

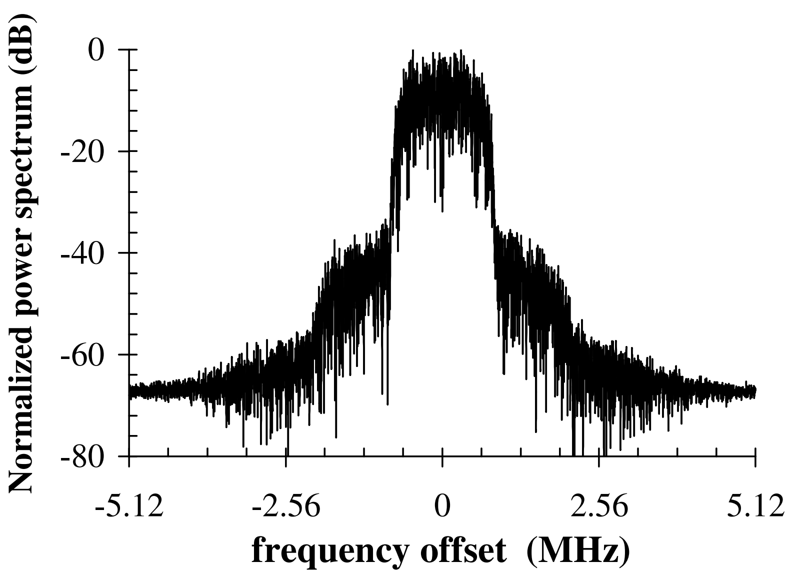

Figure 4.24: Spectrum of a link output signal computed by nonlinear/EM co-simulation (b).

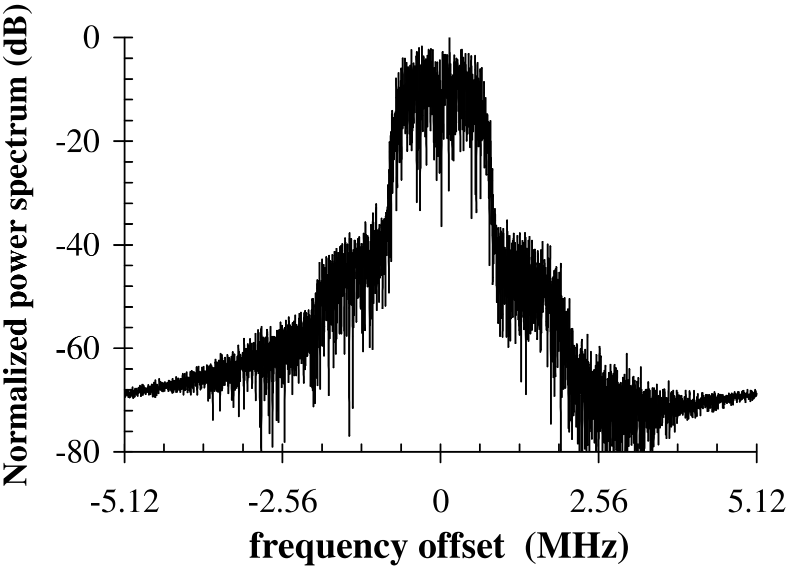

Fig. 4.25 : Spectrum of a link output signal computed by by time-domain analysis (b).

Good agreement is also observed between the output signal spectra reported in figs. 4.24 and 4.25 showing a small gain offset and some marginal differences confined to the noisy regions of the spectra. These small discrepancies are most likely due to slight differences in the nonlinear device models and to the fact that time-domain results are obtained under the assumption of ideally thin dipoles, while for the EM analysis a small but finite conductor diameter must be used. In addition, the radiation susceptance $\mathrm{Im}[Y_t(\omega)]$ is not computed exactly, but is obtained by a variational method [25]. It is noteworthy that even with the small size of the test problem, time-domain analysis is about 22000 times slower than the nonlinear/EM approach.

5.1 INTRODUCTION

This chapter introduces another new feature in the link analysis procedure. So far, the channel has been considered ideal. Now, different link analyses have been carried out taking into account all the environmental factors which are experienced by the signal during the propagation. Therefore, the aim of this chapter is to address a nonlinear analysis of RF/microwave links by combining rigorous circuit-level non-linear analysis of the transmitting and receiving front ends, electromagnetic (EM) characterisation of the antennas, and *realistic description* of the radio channel. The latter is a multipath model based on a 3-D ray tracing (RT) approach. The connection between transmitter and receiver is established by a full EM computation of the radiated far field under modulated input drive.

5.2 DESCRIPTION OF THE METHOD

For instance, a full-wave simulation of the transmitting antenna is performed, thanks to an electromagnetic simulator, such as CST Microwave Studio; the coefficients appearing in (3.5), extracted from EM simulation, are inserted in the linear subnetwork of transmitter; subsequently, nonlinear analyses are carried out by means of MHB technique, in order to produce the radiated field envelope. This information is input to a RT-based radio channel model to obtain the received field in realistic propagation conditions. Finally, by means of EM analysis of the receiving antenna, the receiver excitation is computed and its circuit-level nonlinear analysis is again performed by MHB. We may refer to fig. 3.1 to visualize the conceptual blocks involved in the link analysis.

5.3 RAY TRACING APPROACH

A deterministic approach based on Ray Tracing (RT) simulation has been adopted to describe the whole radio channel in realistic propagation conditions. Frequency dispersion due to propagation impairments is modelled by means of the following channel transfer function:

$$B(\omega) = \sum_{i=1}^{N_p} B_i(\omega_{RF}) = \sum_{i=1}^{N_p} \rho_i \exp(-j\omega\, \tau_i) \qquad (5.1)$$

where N_p is the required number of multipath components, and ρ_i, τ_i are the i-th path complex amplitude and propagation delay, respectively. Note that these parameters are not *a priori* established, but are varied, by means of RT simulations, for specific topography and environmental cases, such as urban sites. The computation of (5.1) is based on an image RT technique [26]: a full 3D approach is adopted to include the effects of far but prominent buildings, which could not be covered by a 2D or 2-and-a-half-D approach. The computation consists of two main steps, i.e., the creation of the *visibility tree* and the *backtracking procedure* [26]. Once the rays have been tracked, each path is associated with its *coherent vector field*, $\mathbf{E}_i$, which depends on reflection and diffraction coefficients; depending on the undergone interactions with the propagation environment. In particular, reflection and diffraction are modelled according to geometric optics and the uniform theory of diffraction, respectively. Each propagation delay τ_i depends on the i-th path total length r_i as

$$\tau_i = \frac{r_i}{v_p} \qquad (5.2)$$

$$\rho_i = \frac{J_{RAi}(\mathbf{E}_i)}{I_{TA}} \qquad (5.3)$$

where v_p is the free-space phase velocity. The complex amplitude ρ_i is determined as the ratio between the received current phasor in the presence of the i-th path only (J_{RAi}), and the transmitting antenna input current phasor (I_{TA}), defined in chapter 3.

For each incoming ray, I_{RAi} is computed by means of the reciprocity theorem [3], taking into account the gain and the polarisation vector of the receiving antenna in the direction of the selected ray. In the end, the final step consists in the superposition of all the contributions given by every single ray, as indicated in (5.1). The Norton equivalent driving source $J_{RA}(\omega)$ at the receiver can be written as

$$J_{RA}(\omega) = \left[\sum_{i} \mathbf{B}_i(\omega) \right] \mathbf{V_T}(\omega) \tag{5.4}$$

where $V_t(\omega)$ is the complex envelope voltage at the transmitter RF output.

For each transmitter and receiver location in a defined topographical environment, the entries of (5.1) are provided by 3D RT simulation. In this work the channel transfer function has been computed in the case of single transmitting and receiving antennas for illustrative purposes (SISO). This work is extended in chapter 7, which will be devoted to investigate the channel characterisation in the case of multiple-antenna links (MIMO systems). In that case, the transfer function will become a complex matrix with size M x N, where M is number of transmitters, N the number of receivers.

5.4 NUMERICAL EXAMPLE OF APPLICATION

As an illustrative example, we consider the link schematically represented in fig. 5.1. The link includes: i) a single-conversion transmitter front-end arranged in a lower sideband suppressing configuration, described as a nonlinear circuit with a total of 98 device ports and 1185 nodes; the small signal gain of the receiver is 50.4 dB; ii) as for the antennas, single half wavelength dipoles, analized by 3D EM simulator have been used both at the transmitting and at the receiving side; iii) a realistic channel described by a 3D-RT model including the EM characterisation of the antennas; iv) a single-conversion receiver front-end with an image-rejection architecture, having a total of 208 device ports and 1745 nodes. The input 45 MHz IF carrier is phase- and amplitude-modulated according to the 16 QAM format. 2 samples/bit is chosen as oversampling factor. The small signal gain of the receiver is 60dB.

We studied 6 deterministic cases over urban environment; we considered three different links: first, transfer matrix B(ω) was computed in Free-Space, then in Non-Line-of-Sight (NLOS), finally in Line-of-Sight; the realistic 2D-map represents Helsinki city, the "scenario" taken into consideration (fig. 5.1).

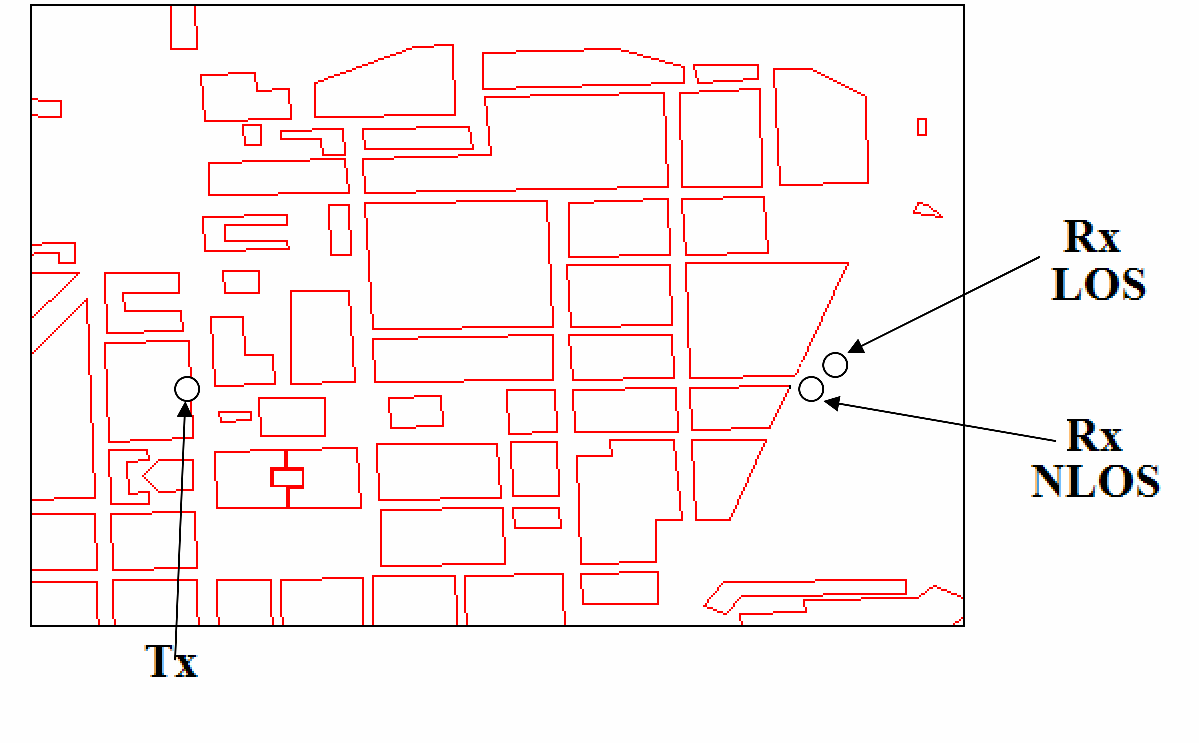

Figure 5.1: Scenario for the ray-tracing simulation

The average input IF power is -28 dBm, in both cases. This value corresponds a slightly more than 2dB compression point; this relatively low value has been chosen on purpose, in order to show above all the linear distortion effect of the channel than the one caused by front-end nonlinearities. The LO signal is sinusoidal with -6 dBm available power at 855 MHz. The output IF is 90 MHz. A spectrum of 4 LO harmonics plus one lower and one upper sideband per LO harmonic is taken into account in the analysis of each front end. Different RT simulations are performed in a typical macrocellular radio network configuration, with the transmitter placed over the rooftop of a building 30 m high. The total number of received paths to be taken into account is found to be about 600. The CPU time required to compute the channel transfer function is 31000 s on a DELL Latitude C840 PC. The ray tracing simulations have been performed with a number of paths N_P equal to 600. Figs. 5.2, 5.3 show similar plots for the Line-Of-Sight (LOS) propagation conditions. As expected, the latter result in a higher (2-order of magnitude) transfer function magnitude and in a weaker dispersive effect, with respect to the former. Figs. 5.4, 5.5 show the frequency dependence of the channel transfer function, in the case of Non-Line-Of-Sight (NLOS) propagation: the selective fading due to the channel is quite evident.

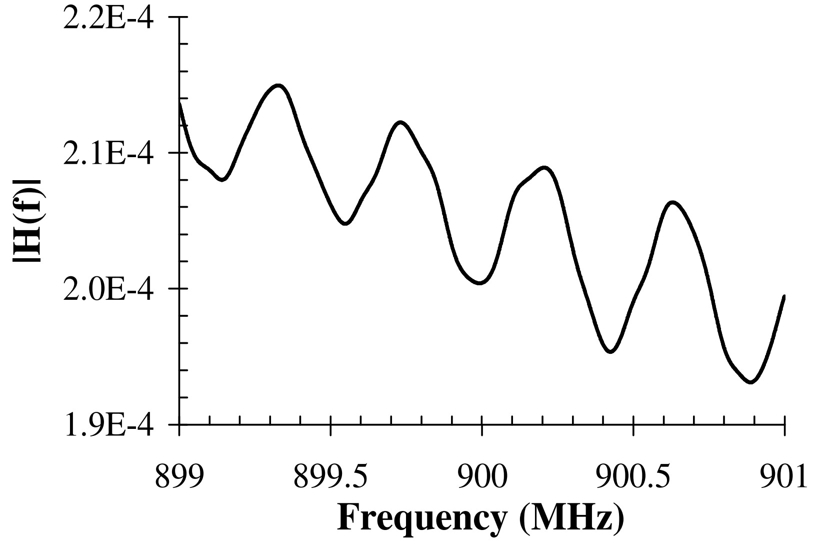

Figure 5.2 : Frequency dependence of the channel transfer function amplitude (LOS case)

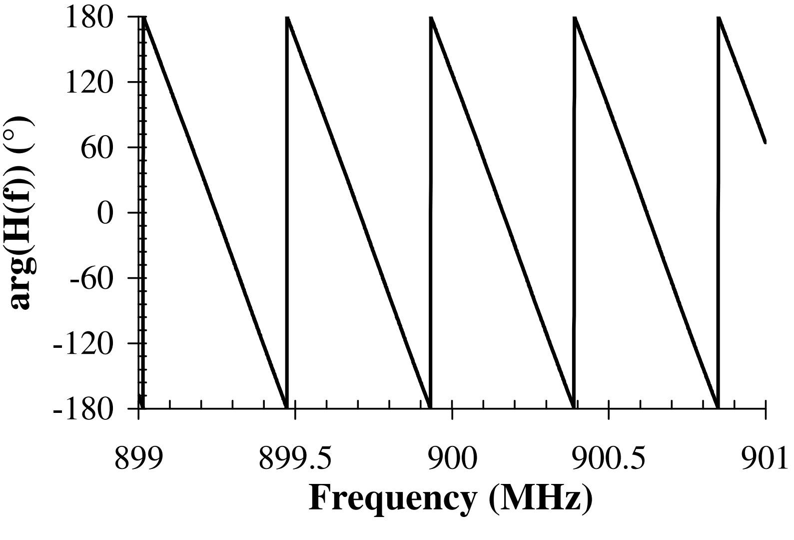

Figure 5.3 : Frequency dependence of the channel transfer function phase (LOS case)

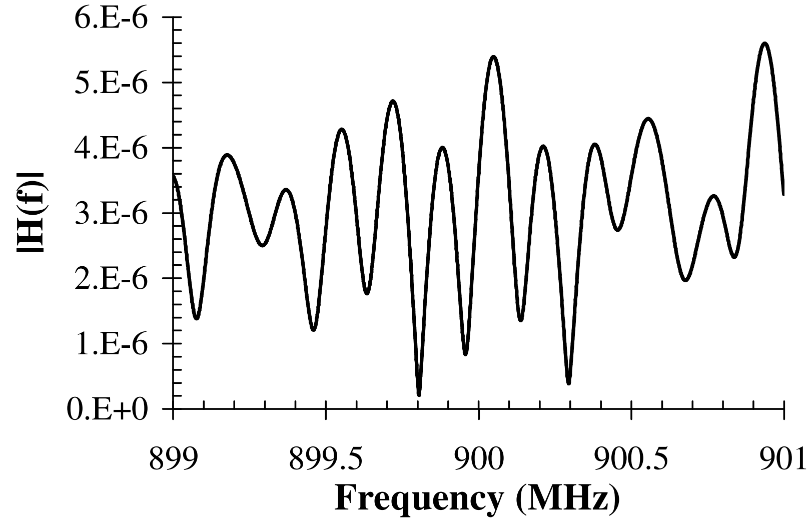

Figure 5.4 : Frequency dependence of the channel transfer function amplitude (NLOS case, bit-rate=72 kb/s)

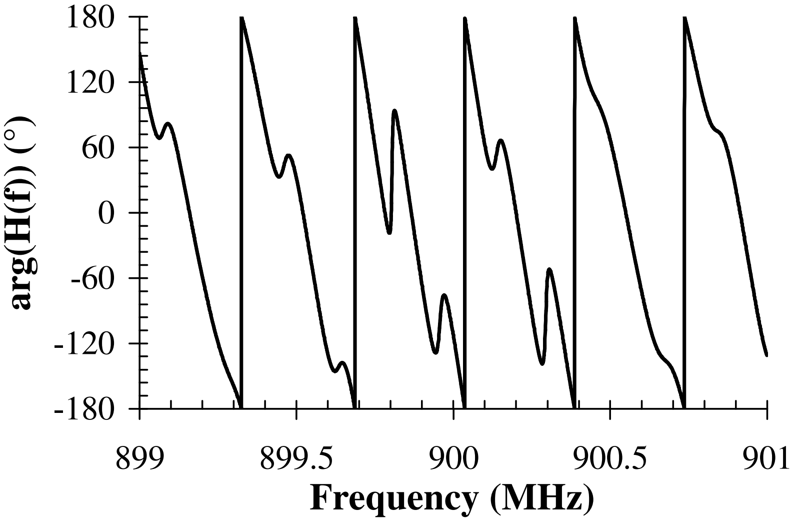

Figure 5.5 : Frequency dependence of the channel transfer function phase (NLOS case, bit-rate=72 kb/s)

The effects of channel dispersion is also investigated by means of an End-to-End circuit-level envelope analysis in three different propagation conditions: free-space (FS), LOS and NLOS, with about the same transmitter-to-receiver distance for the two bit-rates. Figs. 5.6, 5.7 show the corresponding normalised envelope amplitudes for the IF transmitter input current $\tilde{I}_{TA}(t)$ and IF receiver output $\tilde{I}_{OUT}(t)$ (32-bit sequence) in the 72 kbit/s case.

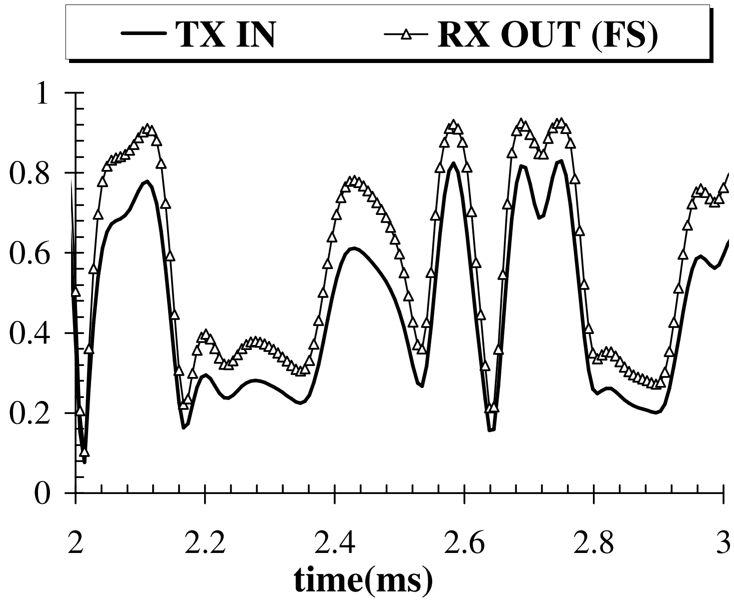

Figure 5.1 : Normalised signal envelope amplitudes at the link I/O ports with free-space propagation (bit-rate=72 kb/s)

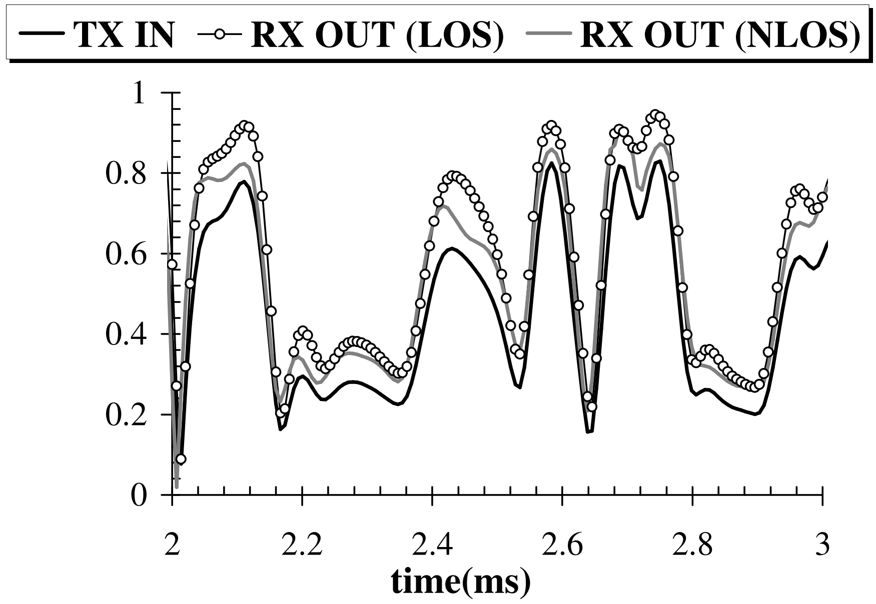

Figure 5.2 : Normalised signal envelope amplitudes at the link I/O ports for two realistic channel descriptions (bit-rate=72 kb/s)

Due to the small signal bandwidth, the LOS channel introduces just a small perturbation with respect to free-space propagation, as predicted by the plots of figs. 5.2, 5.3.

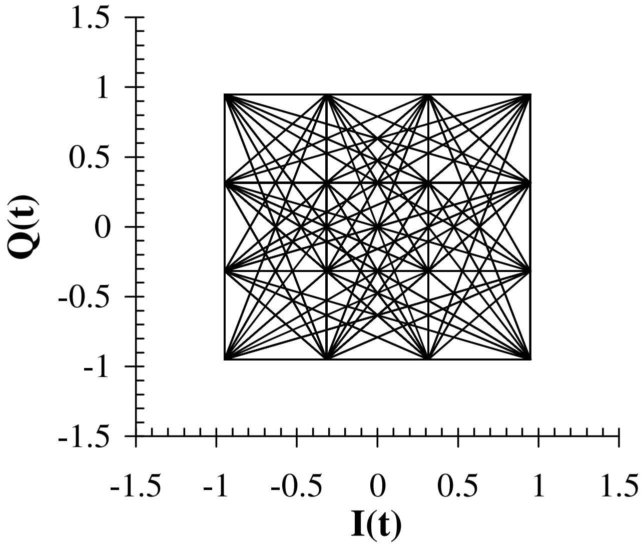

Figure 5.3 : Phase trajectories of the transmitter input signal envelope

On the contrary, the link analysis for the NLOS case clearly shows a significant channel contribution to the envelope shape. The overall link distortion can be clearly observed in figs. 5.8, 5.9, 5.10, where the phase trajectories of $\tilde{I}_{TA}(t)$, $\tilde{I}_{OUT}(t)$ in LOS case, $\tilde{I}_{OUT}(t)$ in NLOS case and are plotted. Note a slight difference between the LOS and NLOS propagation conditions.

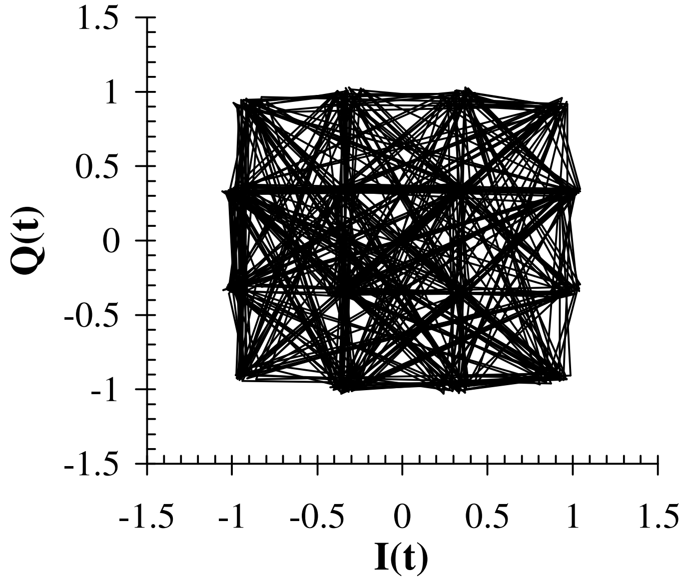

Figure 5.4 : Phase trajectories of the transmitter output signal envelope (LOS case, bit-rate 72Kb/s)

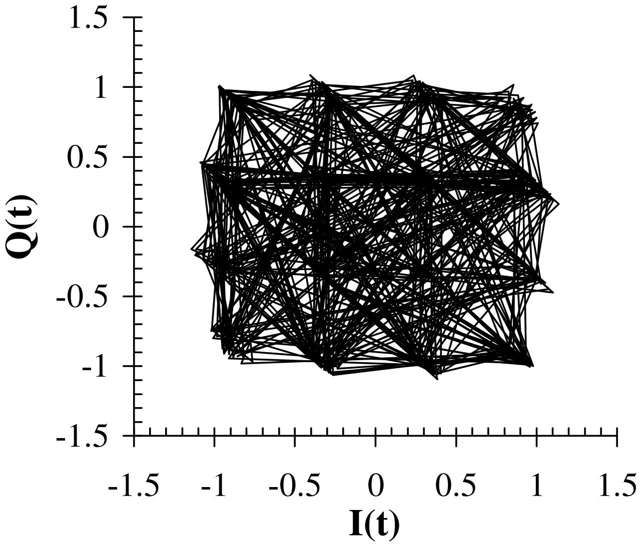

Figure 5. 5 : Phase trajectories of the transmitter input signal envelope (NLOS case, bit -rate 72Kb/s)

Let us treat now the wideband case. Figs. 5.11, 5.12 show the results of the analysis carried out at a bit rate of 1.28 Mb/s (32-bit sequence). By comparison of fig. 5.6 and fig. 5.11 it is clear that the channel behaviour is strongly dependent on the bit rate, apart from the free-space propagation condition, which, by the way, is an ideal operating state (comparison between figs. 5.5 and 5.10). The high distortion level can be seen in terms of phase trajectories in figs. 5.13, 5.14 ($\tilde{I}_{TA}(t)$, $\tilde{I}_{OUT}(t)$ in LOS case, $\tilde{I}_{OUT}(t)$ in NLOS case respectively). In this case, by comparing figs. 5.13 and 5.14, note that distortion is slightly more evident in the NLOS case than in LOS case.

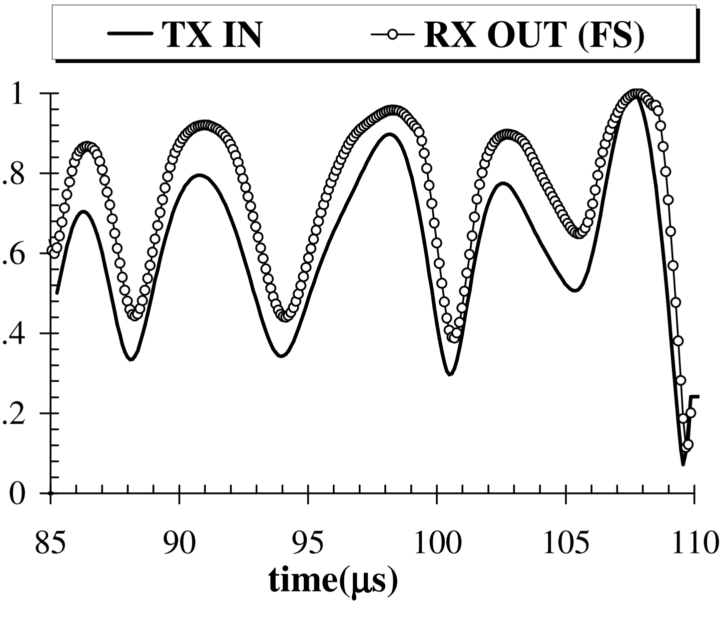

Figure 5. 6 : Normalised signal envelope amplitudes at the link I/O ports with free-space propagation (bit-rate=1.28 Mb/s)

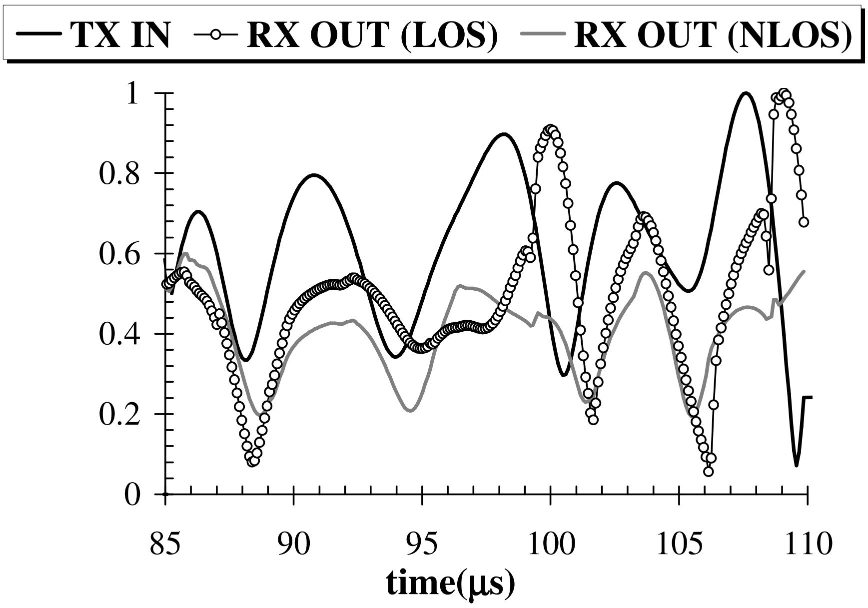

Figure 5.7 : Normalised signal envelope amplitudes at the link I/O ports for two realistic channel descriptions (bit-rate=1.28 Mb/s)

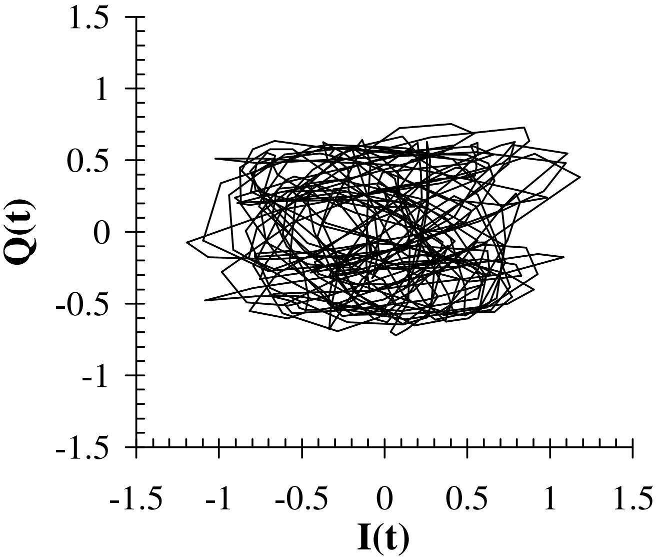

Figure 5.8 : Phase trajectories of the transmitter input signal envelope (LOS case, bit-rate 1.28Mb/s)

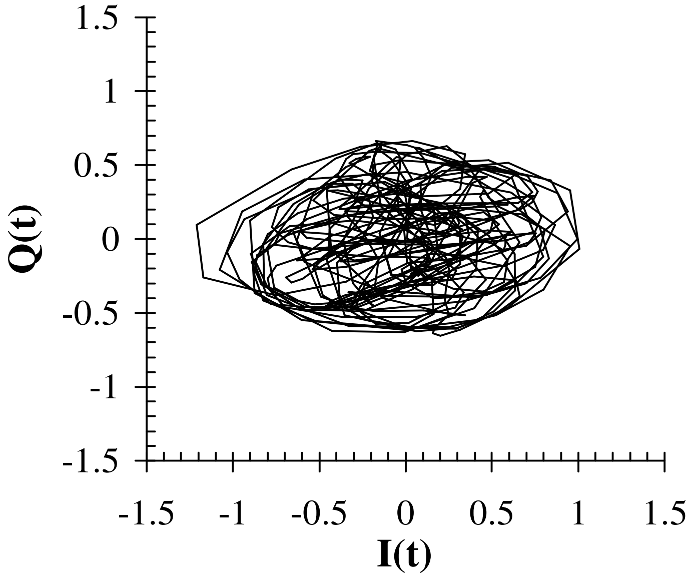

Figure 5.9 : Phase trajectories of the transmitter input signal envelope (NLOS case, bit-rate 1.28Mb/s)

As for the simulation time, the average CPU time required for the overall circuit-level analysis is about 7 seconds per envelope sampling instant on a DELL Latitude C840 PC. The total EM simulation time for each antenna is about 10 minutes; Ray Tracing simulation time is 240 minutes in order to have an accurate transfer function. Therefore, the simulation time of the entire link takes about 730 minutes (4096 envelope sampling points). As for the nonlinear analysis, the simulation time is reduced by a factor 4 if an ultra-modern PC (16GB RAM) is utilized; in such a way the overall simulation would take 370 minutes.

6.1 INTRODUCTION

This chapter present a novel approach to treat multiple-input multiple-output (MIMO) systems; the novelty consists that for the first time a CAD procedure for the circuit-level simulation of an entire MIMO link is available.

Many recently developed communications systems make use of multiple antenna elements both in the base station and the terminals (MIMO systems) in order to improve link capacitance and BER performance by exploiting spatial diversity and multipath propagation. In order to accurately predict MIMO performance it is of primary importance that the following effects be simultaneously accounted for: 1) near-field coupling effects between antenna elements; 2) far-field radiating behavior of the antenna array for specific channel scenarios. The former are needed to accurately describe port mismatch and power transfer effects between the antenna elements and the nonlinear subsystems, as well as the dependency of antenna impedances on frequency [27]. The latter are needed for a realistic computation of the channel transfer matrix and hence of the MIMO system capacitance.

In the following chapters, for the first time we apply the general and rigorous CAD procedure that provides a systematic answer to all the above needs by combining nonlinear, electromagnetic (EM), and propagation analysis tools. This opens the way to a circuit-level nonlinear/EM co-simulation of MIMO systems. With this method, the multiple transmitter front-ends are analyzed under digital modulated IF drive as a single nonlinear system loaded by a multiport antenna characterized by full-wave EM analysis. As in chapters 3, 4, 5, in order to produce the radiated field envelope, the EM results are interfaced with an envelope-oriented harmonic-balance technique (MHB) based on Krylov-subspace model-order reduction [28]. The far-field radiated by each array element in the presence of the other ones (*embedded field*) is used as the input to an advanced 3D Ray Tracing (RT)-based radio channel model [26], to compute the channel matrix in realistic propagation conditions. Finally, by applying the reciprocity theorem to the multiport antenna system, the receiver excitations are rigorously derived as a function of the incident fields. The circuit-level nonlinear analysis of the multiple receiver treated as a whole is again performed by MHB. A full demonstration of the capabilities of the method is provided by simulating the transmission of a 16-QAM signal through a 2x2 MIMO link and computing the system BER as a function of signal-to-noise ratio and antenna spatial diversity. For a given channel scenario, the method may be used for the nonlinear/EM design of a MIMO link to establish optimum antenna spacing with respect to BER or nonlinear distortion.

6.2 COMPUTATION OF THE TRANSMITTING ANTENNA EXCITATIONS AND FAR-FIELD

Fig. 7.1 shows a block representation of a MIMO transmitter including the antenna array. The multiple RF/microwave transmitter front ends are described as a unique nonlinear system consisting of an arbitrary set of nonlinear devices interconnected by a linear subnetwork. By means of the piecewise harmonic-balance (HB) technique, the circuit is partitioned into a linear and a nonlinear subnetwork that are connected through N_D^T ports (*device ports*) where

$$N_D^T = \sum_{t=1}^{N_T} n_D^t \qquad (6.1)$$

In (6.1), N_T is the number of transmitters and n_D^tn is the number of device ports belonging to the t-th transmitter. The linear subnetwork is referred to as N_{NORAD} fig. 6.1 and is treated by conventional circuit analysis algorithms. The antenna array is referred to as N_{RAD} in fig. 6.1. It is described layout-wise and is analyzed as a linear multiport radiating system by full-wave EM simulation (FIT technique). This analysis simultaneously provides the antenna scattering matrix and three-dimensional far-field radiation pattern at all frequencies of interest. The N_{NORAD} ports may be grouped into three sets, as shown again in Fig. 6.1: N_D^T ports for nonlinear device connection, N_E^T excitation ports, and N_T connection ports to the N_{RAD} network. The voltages or currents at the third group of ports (as computed by nonlinear analysis of the transmitters) represent the antenna array excitation. In this way the array excitation need not be described as a set of a priori known free current sources, which has been shown to have a significant impact on the MIMO channel capacitance estimation [29].

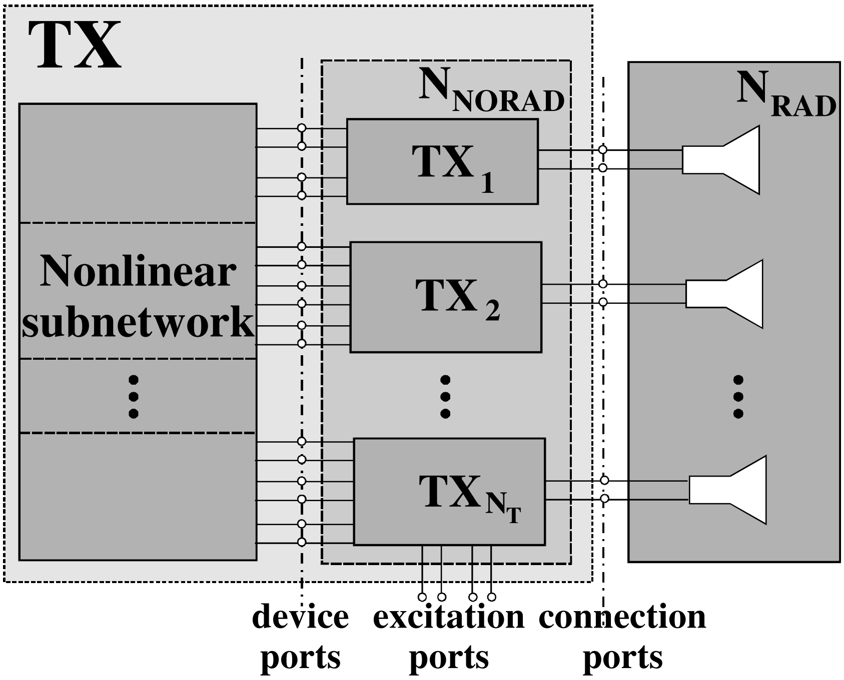

Figure 7. 1: Block diagram of a MIMO system transmitter side.

Let us now assume that each transmitter front-end is excited by a sinusoidal IF signal of angular frequency ω_{IFT} and by a sinusoidal local oscillator (LO) of angular frequency ω_{LOT}. The resulting large-signal regime will be quasi-periodic with spectral lines at all the intermodulation products

$$\Omega_{T,k} = k_1 \omega_{IFT} + k_2 \omega_{LOT}; \qquad \mathbf{k} = [k_1 \quad k_2]^{tr} \tag{6.2}$$

where the k's are integer harmonic numbers. A multitone harmonic balance analysis may be carried out by well-known algorithms to compute the N_D^T-vectors of the transmitter state-variable harmonics, $\mathbf{X}_{T,k}$ at all discrete lines defined by (2). One of such lines is the RF frequency ω_{RF} of the signal to be transmitted, which will be obtained from (6.2) for some **k**, say **k** = **s** ($\omega_{RF} = \omega_{T,s}$). After an HB analysis of the transmitter has been carried out, the complex phasors of the currents flowing out of the N_T connection ports may be expressed from the linear subnetwork equations as

$$\tilde{\mathbf{I}}_{T,s} = \mathbf{Y}_{DT} (\omega_{RF}) \mathbf{X}_{T,s} + \mathbf{Y}_{TT} (\omega_{RF}) \mathbf{V}_{T,s} \tag{6.3}$$

In (6.3), $\mathbf{Y_{DT}}$ is the (N_T x N_D^T) admittance submatrix of the N_{NORAD} network relating the device ports to the connection ports, $\mathbf{Y_{TT}}$ is the (N_T x N_T) admittance submatrix seen from the connection ports, and $\mathbf{V_{T,s}}$ is the vector of voltage phasors at the connection ports. Furthermore, if $\mathbf{Y_{AT}}$ is the (N_T x N_T) admittance matrix of the multi-element antenna resulting from EM analysis, we have

$$\mathbf{I_{T,s}} = \mathbf{Y_{AT}}\,(\omega_{RF})\,\mathbf{V_{T,s}} \tag{6.4}$$

By combining (6.3) and (6.4) we get

$$\mathbf{V} = [\mathbf{Y_{AT}}(\omega_{RF}) - \mathbf{Y_{DT}}(\omega_{RF})]^{-1}\,\mathbf{Y_{TT}}\,(\omega_{RF})\,\mathbf{X_{T,s}} \tag{6.5}$$

For the t-th array element, with the assumption of free-space propagation, we may then express the total radiated field at ω_{RF} similar to (3.2)

$$\begin{aligned}&\mathbf{E}_{\mathbf{T}}^{(t)}(r, \theta, \phi; \omega_{RF}) = \frac{\exp(-j\beta r)}{r}\cdot\\ &\cdot\left[\hat{\boldsymbol{\theta}}\, A_{T\theta}^{(t)}(\theta, \phi; \omega_{RF}) + \hat{\boldsymbol{\phi}}\, A_{T\phi}^{(t)}(\theta, \phi; \omega_{RF})\right] V_{T,s}^{(t)}\end{aligned} \tag{6.6}$$

where $A_{T\theta}^{(t)}$, $A_{T\phi}^{(t)}$ are the scalar components of the normalized field in a spherical coordinate system with origin in the phase center O_T of the transmitting array. Such components are generated by EM simulation with a unit-voltage sinusoidal source of angular frequency ω_{RF} connected to the t-th port and the remaining ports short-circuited. In this way the actual frequency-dependent array admittance and the *embedded radiation pattern* of each array element are available and can be combined with any suitable channel description tool.

In this work a Ray Tracing (RT) algorithm [26] specialized for MIMO channel has been adopted and extended to account for the array near- and far-field performance. A coherent representation of the transmitted electric field corresponding to each radio path (r_k) is computed as a complex vector whose amplitude and phase depend on the traveled distance and on the interactions experienced by the propagating wave. Considering all the paths between the two radio terminals and the corresponding propagation delays and angles of arrival, a multidimensional characterization of the array-dependent MIMO channel matrix is derived. Let (θ_D, ϕ_D) be the initial (departure) direction of the q-th ray generated by the t-th antenna. The far field $\mathbf{E}_{\mathbf{T}}^{(q,t)}(r,\theta_D,\phi_D;\omega_{RF})$ radiated by the same antenna in the direction (θ_D, ϕ_D) and computed by EM analysis as previously discussed, represents the input to the RT algorithm for the ray under consideration. Considering its interaction with the channel in terms of spreading factor (reflection, diffraction and scattering), path losses and phase shift, the ray field incident on the phase center of the receiving array and referred to the position of its r-th element is

$$\begin{aligned}
\mathbf{E}_{r}^{(q,t)}(r,\theta_A,\phi_A;\omega_{RF}) &= \Gamma^{q,t}\left(s_1^{q,t},..,s_\ell^{q,t},..,s_{N_B^{q,t}}^{q,t}\right)\cdot \\
&\cdot\left[\prod_{\ell=\min\{1,N_B^{q,t}\}}^{N_B^{q,t}} \underline{\underline{A_\ell^{q,t}}}\right]\cdot \mathbf{E}_{\mathbf{T}}^{(q,t)}(r,\theta_D,\phi_D;\omega_{RF})e^{\pm j\beta d^h}
\end{aligned} \tag{6.7}$$

In (6.7)

- (θ_A, ϕ_A) is the ray direction of arrival;
- s_ℓ is the length of the ℓ-th segment composing the q-th path;
- $N_B^{q,t}$ is the number of “bounces” experienced by the ray;
- $\Gamma^{q,t}$ is the spreading factor;
- $\underline{\underline{A_\ell^{q,t}}}$ is an appropriate dyadic used to decompose the field into orthogonal components at the ℓ-th interaction point;
- d^h is the distance of the phase center of the r-th element from the receiving array phase center.

In order to define the channel transfer matrix, the receiving array excitations for each incoming ray need now be computed.

6.3 CALCULATION OF THE MULTIPLE-RECEIVER CURRENT EXCITATION

The multiple receiving front end is described by a block diagram similar to the one shown in fig. 6.1 for the transmitter side. In this case N_R connection ports between the N_{RAD} and the N_{NORAD} linear subnetworks are used to transfer the signal received by the array to the N_R receivers. The receiving array is again characterized by a frequency-domain 3-D EM simulation and the corresponding (N_R x N_R) admittance matrix $\mathbf{Y_{AR}}$ is computed for each frequency of interest. The q-th ray radiated by the t-th element of the transmitting antenna will excite voltages and currents in the receiving array.

In such conditions the N_{RAD} network is active, though linear, and may be represented by a Norton equivalent circuit leading to the circuit equations

$$\mathbf{I}_{\mathbf{R,s}}^{(q,t)} = \mathbf{Y_{AR}}(\omega_{RF})\,\mathbf{V}_{\mathbf{R,s}}^{(q,t)} + \mathbf{J}_{\mathbf{R,s}}^{(q,t)} \tag{6.8}$$

In (6.8) $\mathbf{J}_{\mathbf{R,s}}^{(q,t)}$ is the vector of unknown Norton current sources at the N_{RAD} connection ports, representing the circuit equivalent of the incident field associated with the ray under consideration. In order to find $\mathbf{J}_{\mathbf{R,s}}^{(q,t)}$ we first suppress the incident ray, and operate the receiving array in a transmitting mode. The array is now fed by a unit voltage source connected to the r-th port, and all remaining ports are short-circuited. In such conditions the radiated far field $\mathbf{E}_{\mathbf{RN}}^{r}(\theta_A', \phi_A'; \omega_{RF})$ and the input admittance Y_{rr} are computed by EM analysis as discussed in §6.2. Here, (θ_A', ϕ_A') are the angular coordinates of the ray direction of arrival in a receiver-referred spherical phrame. We then reintroduce the incident field and short-circuit all the antenna ports, so that by (6.8) the entries of $\mathbf{J}_{\mathbf{R,s}}^{(q,t)}$ coincide with the port currents. Such currents may then be expressed by a straightforward application of the reciprocity theorem, as in chapter 4. Specifically, for a the q-th ray radiated by the t-th element, the r-th entry of $\mathbf{J}_{\mathbf{R,s}}^{(q,t)}$ may be cast in the form:

$$\begin{aligned} J_{r,s}^{(q,t)} = j\frac{2}{\eta}\lambda\, Y_{rr}\, \mathbf{E}_{\mathbf{RN}}^{r}(\theta_A', \phi_A'; \omega_{RF}) \cdot \\ \cdot \mathbf{E}_{r}^{(q,t)}(r, \theta_A, \phi_A; \omega_{RF}) \quad (1 \le r \le N_R) \end{aligned} \tag{6.9}$$

A superposition of all the contributions (6.9) spanning all the incoming rays finally yields the current source at the r-th port:

$$J_{r,s} = \sum_{t=1}^{N_T} \sum_{q=1}^{N_{RAY}^{t}} J_{r,s}^{(q,t)} \tag{6.10}$$

where N_{RAY}^{t} is the number of rays coming from the t-th transmitter element. The exact computation of the (N_T x N_T) channel transfer matrix is now immediately available by simultaneously writing (6.10) for all ports in vector form:

$$\mathbf{J}_{\mathbf{R,s}} = \mathbf{H}(\omega_{RF})\mathbf{V}_{\mathbf{T,s}} \tag{6.11}$$

At this stage, we write the receiver N_{NORAD} equations in a way similar to (6.3), namely

$$\tilde{\mathbf{I}}_{\mathbf{R,s}} = \mathbf{Y}_{\mathbf{DR}}(\omega_{RF})\,\mathbf{X}_{\mathbf{R,s}} + \mathbf{Y}_{\mathbf{RR}}(\omega_{RF})\,\mathbf{V}_{\mathbf{R,s}} \tag{6.12}$$

where the subscript “R” stands for “receiver”, and the meanings of all quantities are otherwise identical. (6.8), (6.12) and the nonlinear subnetwork equations are now handled in the usual way to produce a multitone HB analysis of the receiver.

6.4 A PERFORMANCE BENCHMARK

A 2x2 MIMO link designed for WLAN application at 2.347 GHz is considered. The transmitter consists of two single-conversion front ends (the single diagram block is shown in fig. 3.5) with a total of 196 device ports and 2370 nodes; the receiver consists of two image-rejection front ends with 416 device ports and 2490 nodes (fig. 3.14). The antennas at both sides are two parallel half-wave dipoles printed on separate substrates and are analyzed by full wave EM analysis for several element spacings. They are shown in fig.6.2. The dielectric constant is 6.15, the copper thickness is 0.035 mm and the substrate thickness is 0.635 mm.

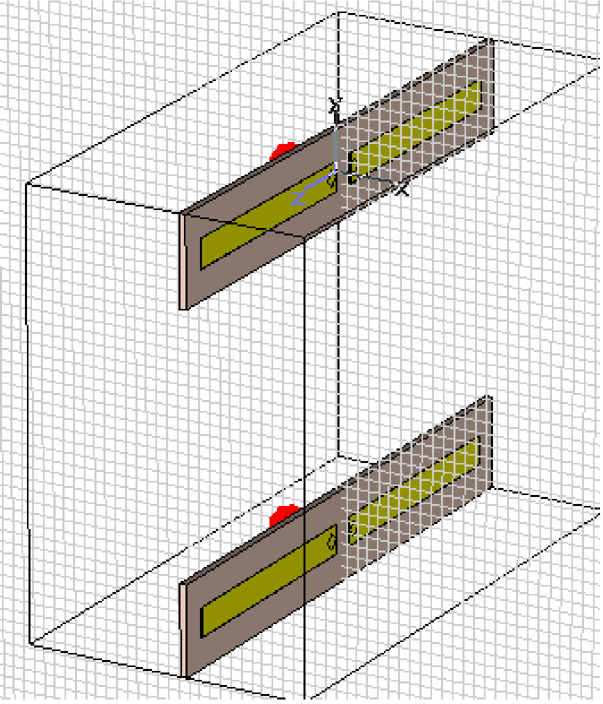

Figure 6.2: Parallel half-wave dipoles on separate substrate

The results in terms of two-port scattering parameters can be observed in figs. 6.3 a) , b). In fig 6.3 a), note that |S11| is almost coincident for SISO and 4λ cases, better than in l/8 case. In this last case, switching to fig. 6.3 b), some power is transmitted to the other port, so that to -10 dB mutual coupling is reached. This happens because of the proximity of the two antennas. Moreover, as far as the distance between antennas increases, the coupling tend to disappear.

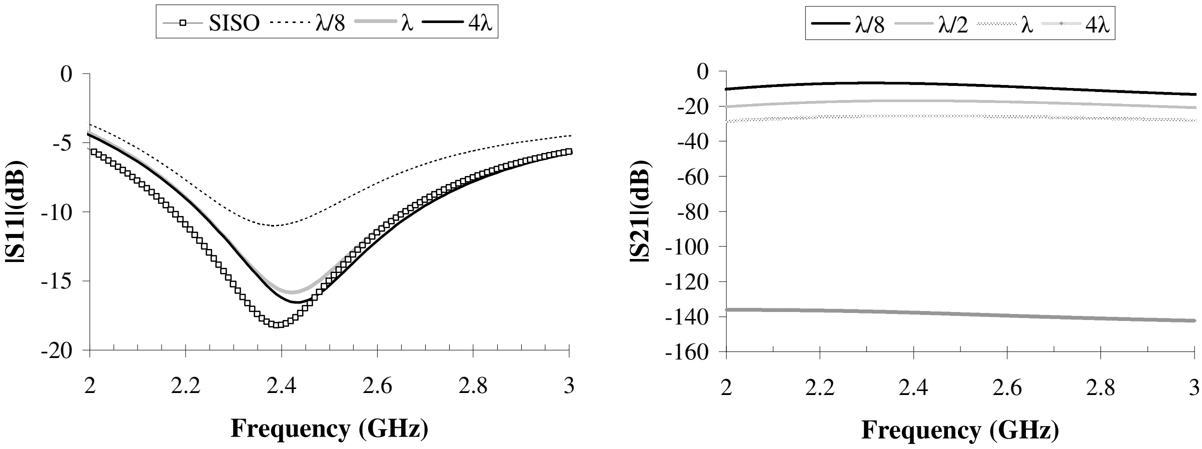

Figura 6.3: a) |S11| and b) |S21| vs frequency for several element spacings

In terms of and “embedded radiation pattern”, it may be observed a 15% shift of the resonant frequency, and a remarkable pattern deformation with respect to the standalone dipole. The λ/2 distance case is taken into exam in fig.6.4 a),b),c),d). Figs. 6.4 a),b) show the E-plane of a standalone dipole and of a dipole at λ/2 distance from the second dipole, respectively. Similarly, 6.4 c),d) show the H-plane in the same two configurations. By comparison of 6.4 a),b) and of 6.4 c),d), we may observe a clear pattern modification due to the parasitic dipole in proximity to the fed one.

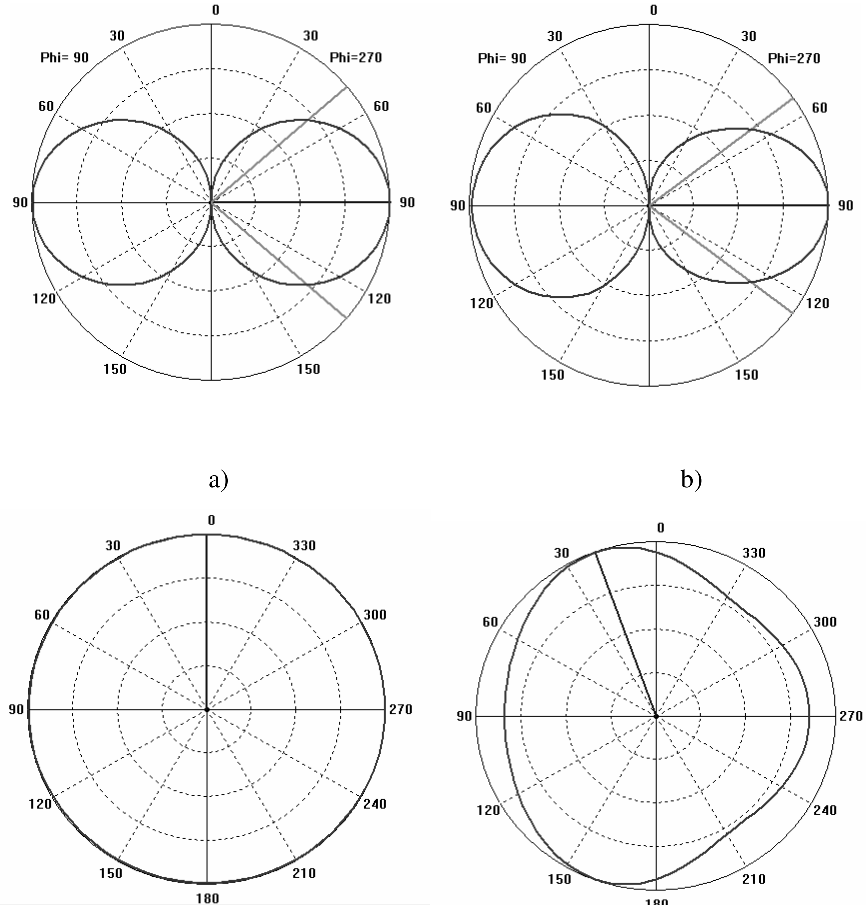

a) b)

c) d)

Figure 6.4: Radiation pattern of the antenna elements: a) Standalone dipole E-plane; b) E-plane of the first dipole, at a λ/2 distance from the second dipole ; c) Standalone dipole H-plane; d)) H-plane of the first dipole, at a λ/2 distance from the second dipole.

The effects of antenna spacing on the channel transfer matrix are investigated in a rich scattering propagation scenario. A sequence of nonlinear link analyses is carried out by varying the transmitting antenna element spacing. The front ends are excited by a sinusoidal IF signal. The receiving antenna elements are kept at a fixed distance of 0.63 cm corresponding to a half wavelength. The channel scenario needs more than 3000 propagation rays. Figs 6.5 and 6.6

compare the amplitudes of the channel transfer matrix coefficients (the first subscript refers to the transmitter dipole, the second one to the receiver), computed by the procedure introduced in this work, for a distance of λ/8 and 2λ, respectively. The two configurations have been found to be the most interesting ones. For the chosen propagation scenario the two plots clearly show that the closer element spacing takes advantage of the channel selective fading in a significant way.

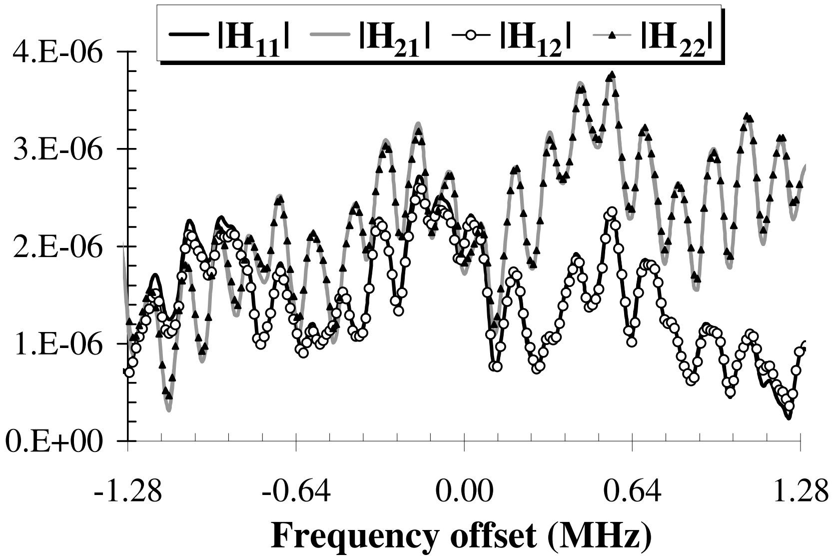

Figure 6.5 : Channel transfer matrix for λ/8 dipoles spacing.

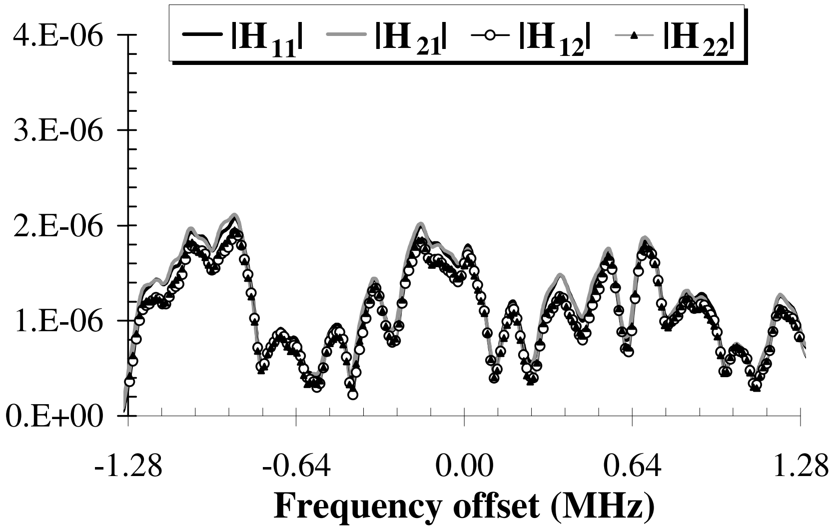

Figure 6.3 : Channel transfer matrix for 2λ dipoles spacing.

Indeed, higher values of the H(ω) elements directly mean a channel capacitance improvement [29]. The input IF carrier is then phase- and amplitude- modulated with a 16-QAM format at a bit rate of 1.25 Mb/sec. The output power spectrum of the link for the optimum dipole.spacing, as computed by in-phase combining the output signals of the two receivers (equal gain combining technique), is plotted in figure 6.7.

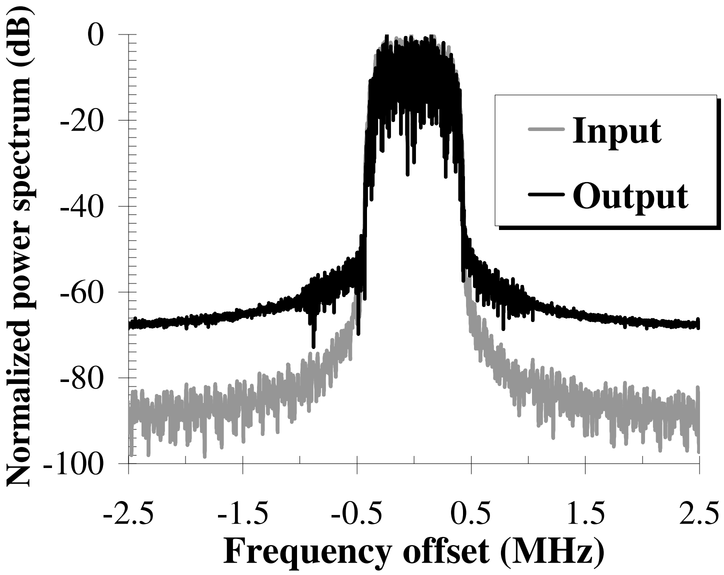

Figure 6.7: Optimum MIMO link normalized power spectra

For comparison the analysis is repeated for a SISO (single-input single output) link in the same propagation scenario and the output power spectrum is plotted in figure 6.8. These spectra shows that proper antenna diversity results in a strong reduction of the spectral regrowth.

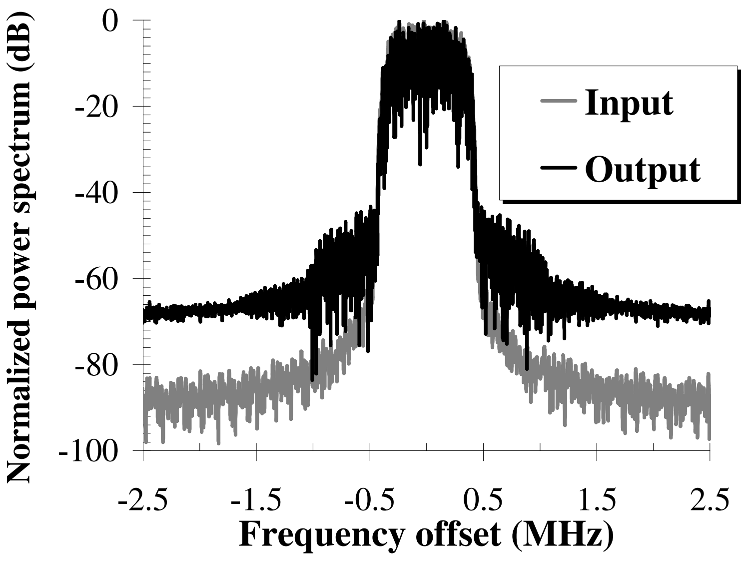

Figure 6.
6.8: SISO link normalized power spectra

This is confirmed by fig. 6.9 where the computed BER of the MIMO link is plotted versus element spacing with a reference noise spectral density of -192 dBc/Hz. In this deterministic case, a strong coupling between elements gives a significant contribution to the minimization of bit-error-rate.

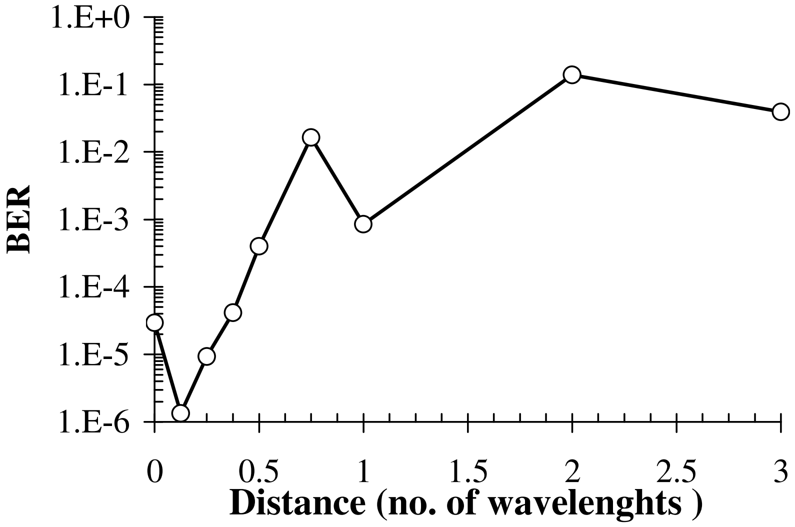

Figure 6.9 : BER as a function of dipoles spacing.

7.1 INTRODUCTION

A last application of the co-simulation technique to ultra-wideband systems is described in the following paragraphs. Nevertheless, a difference occurs with respect to the other case studies. Here not all the link calculation has been performed, but only the transmitter side. The whole computation, including the receiver side, will be subject of future work.

Ultra-wideband (UWB) is probably the most promising technology for modern wireless systems from the viewpoint of low complexity, low power consumption, low cost and high-data-rate short-range wireless connectivity.

UWB technology is a high potential for future wireless applications. Significant research and industrial effort have already been invested, mainly focusing on its high bandwidth potential intended for indoor short range (up to 10 m) and high data rates (> 100 Mb/s) applications, such as wireless multimedia and high performance PC peripherals [30]. Another class of applications which make use of UWB's unique low probability of detection (LPD), low interference, and multipath immunity, is that of medium indoor range, low data rates (< 1 Mb/s), and very low power applications with sensing and tracking capabilities.

As for the bandwidth, according to the Federal Communications Commission, FCC, ultra-wideband devices can operate in the 3.1-10.6 GHz bandwidth while employing at least 500MHz bandwidth (@-10dB point) with a power spectral density (PSD) of less than -41.25 dBm/MHz [31]

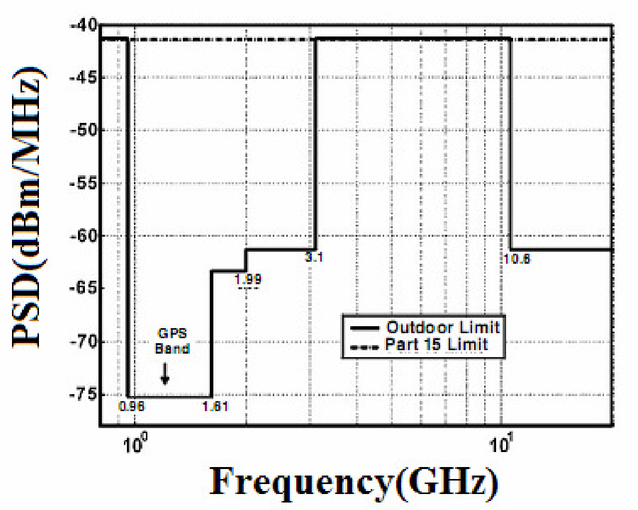

Figure 7. 1 : Mask of an UWB communication system

(see fig. 7.1).

There are several advantages in UWB technology, compared to traditional wireless technologies [32]. Due to its low EIRP emission limit, an UWB signal "behaves as noise" to other radio systems, which results in a low probability of interception and detection. Besides, an UWB signal has excellent multipath immunity and less susceptibility to interferences from other radios, due to its wide bandwidth nature. Furthermore, the UWB technology offers the possibility of greatly simplifying the transceivers architectures. As will be discussed later on, since the information is encoded as short pulses, explicit up and down conversions can be omitted, which results in substantial reduction in the use of power hungry and large area analog circuitry, such as mixers and PLL, and can be realized as a complete SoC in low cost CMOS technologies.

The idea to simulate an ultra-wideband link by means of nonlinear/EM co-simulation techniques would be a turning point in the field of microwave co-simulation techniques. In order to deal with this issue, for instance, it is necessary to develop a co-design technique in order to characterize the entire RF transmitter chain, i.e. RF amplifier and transmitting antenna, at the same time; the aim is to insert this RF chain in a complete UWB link simulation, which will be subject of future work.

From a circuit viewpoint, a major challenge of UWB systems is the need to accurately optimize the power transfer between transmitter and receiver, in such a way as to obtain a flat received power with minimum ripple across the very broad frequency band of interest [33]. This work shows that this goal can best be achieved by designing the transmitter block as a whole including the radiating elements.

This poses the problem of suitably defining the system output as well as a figure of merit simultaneously encompassing nonlinear electrical and radiation performance, to be used as the design goal. The proposed solution is based on the following ideas. In a wireless system, the physical connection between transmitter and receiver is established by the radiated field. From the system viewpoint, the true transmitter output is thus the radiated field **E** incident on the receiver antenna in signal terms, or the associated power density $\mathbf{E} \bullet \mathbf{E}^{*}/2\eta$ in power terms. In order to optimize the power transfer to the receiver, the transmitter design goals should be formulated in terms of such quantities. For this purpose, let us make use of a new figure of merit conventionally called the *electromagnetic-transducer gain* G_{ET}, that suitably combines the antenna and front-end gain. The circuit-antenna assembly is then optimized as a whole by means of nonlinear/electromagnetic (EM) design techniques [34]. In this way the traditional procedure based on separate matching of the antenna and transmitter is effectively overcome and the available degrees of freedom are increased, leading to a significant performance improvement.

In order to illustrate the method, in this work I first design and test a printed UWB antenna by EM techniques. I then feed the antenna by a traveling-wave amplifier (TWA) designed with 50 Ω load, and show that poor performance, in terms of far field flatness, is obtained in this way. This is an expected result: in fact, the transmitter load, which is the antenna input impedance, is not exactly 50 Ω; at the same time, the transmitter output impedance cannot be assumed 50 Ω. These impairments directly lead to a performance degradation of the overall system.

The same is shown to be true if the amplifier is designed for conjugate match to the actual antenna impedance: even if the matching between the two subsystem is perfect, nevertheless far-field flatness is not guaranteed. We then discuss a quantitative definition of G_{ET}, and show that a direct nonlinear/EM optimization of the TWA/antenna assembly in terms of such quantity effectively overcomes the limitations of traditional design techniques and leads to the desired result.

7.2 UWB PLANAR MONOPOLE ANTENNA DESIGN

A planar monopole with a topology similar to the one considered in [35], is adopted as the radiating element in the 7.5 GHz band starting from 3.1 GHz recently defined by the FCC [30]. The design is carried out by the space-mapping-related technique introduced in [34].

Beyond the large bandwidth, the antenna presents these features:

a) reduced dimensions;
b) monopole-like radiation pattern (i.e. toroidal shape around the main axis), suitable for broadcasting, mobile communications, RFID applications, etc..;
c) possibility to integrate it over the same circuit substrate.

Let us give now an accurate description of the procedure followed for the antenna monopole design. The monopole is fed by a 50 Ω line; two structures are designed in a first step: both a 4GHz and a 10 GHz resonant monopole with a partial ground plane; the direct merge of these two structures in a single shape, whose dimensions are chosen as an average of the initial ones, leads to our starting-point. At this stage, the resulting -10 dB bandwidth is within the range 3-6 GHz. Therefore, the 10GHz resonance must be recovered, and the countermove is to taper step-wise the bottom part of the antenna. In such a way, a 3-8 GHz bandwidth is covered. Finally, two slots are etched in the resulting patch in order to improve the high-frequency performance. The wider slot behaves as a 9GHz resonator, whereas the thinner one introduces a further 10GHz resonance.

The final antenna design is depicted in fig. 7.2 a). The antenna lies in the x-y plane, and the far-field maximum occurs in the broadside direction. The dimensions and locations of both slots are included among the design variables. The layout design variables are: the minimum and maximum patch half widths, W_1 and W_2; the total patch length L_p; the feed line length L_g, (this sets the partial ground plane length, as well); the chamfer angle α. The steps are marked by dotted lines, and their number is equal to 3 ($N_{STEP} = 3$). The step width (S_W) and height (S_H) are derived parametrically as follows:

$$S_W = \frac{W_1 - W_2}{N_{STEP}} \qquad\qquad S_H = S_W \,\mathrm{ctg}\,\alpha \tag{7.1}$$

The optimization process proved that input matching and antenna gain across a wide band are conflicting requirements, so that a delicate tradeoff between such two goals must be established. The optimized dimensions are W_1= 7.5mm, W_2 = 1.8mm, L_p = 16mm, L_g= 14mm, Ws1=9.4mm, Ws2= 7.7mm, Ls= 10.2mm and $\alpha = 67°$. Fig. 7.2 b) shows photographs of the fabricated prototype on a Taconic RF-60A 0.635mm-thick substrate, with relative permittivity ε_r=6.5.

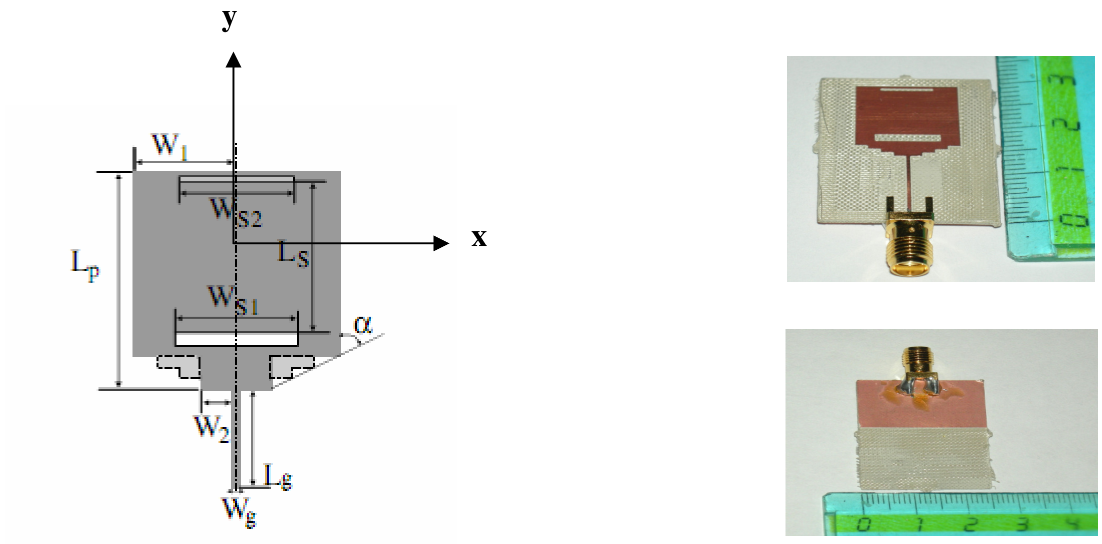

a) b)

Figure 7.2 – a) UWB antenna layout and parameters; b) prototype front view and back view.

In spite of the compact layout, both the input reflection coefficient and the far-field gain exhibit the required broadband behavior, as shown in fig. 7.3 . The gain ripple across the band is less than 2 dB, which represents a considerable improvement with respect to [35]. This is partly due to the more sophisticated optimization procedure and partly to the introduction of the second slot. The measured magnitude of S_{11} is also plotted in fig. 7.3, showing satisfactory agreement with the predictions. In figs. 7.4 a),b),c) the far-field E-plane at 4, 9 and 10 GHz respectively is plotted. Fig. 7.4 a) shows a typical monopole-like shape for the antenna E-plane. As the frequency increases, the same shape is maintained till 8 GHz.

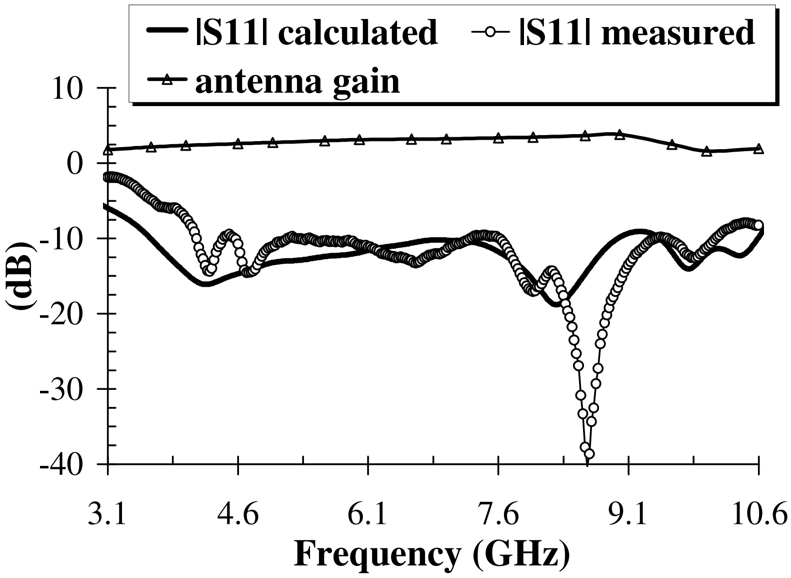

Figure 7.3 – Standalone UWB antenna performance

At 9 GHz the first slot resonates, and it is noteworthy that the slot changes the radiation properties of the structures, since its radiated field is orthogonally polarized with the respect to the monopole one. The clear effect consists in a maximum radiation shift of about θ =15° (fig. 7.4b)). At 10 GHz (fig. 7.4c)), the second slot resonates, and a secondary lobe appears; once again, the radiation diagram is modified with respect to the ones in figs. 7.4 a),b). Nevertheless, such modifications doesn’t significantly affect the θ=0 E-field absolute value, which is quite constant with the frequency. Considering the H-plane, in fig. 7.5 a) the 4GHz radiation pattern is clearly omnidirectional, and it keeps this property till 8GHz; slight modifications take place at higher frequencies (figs. 7.5 b),c)).

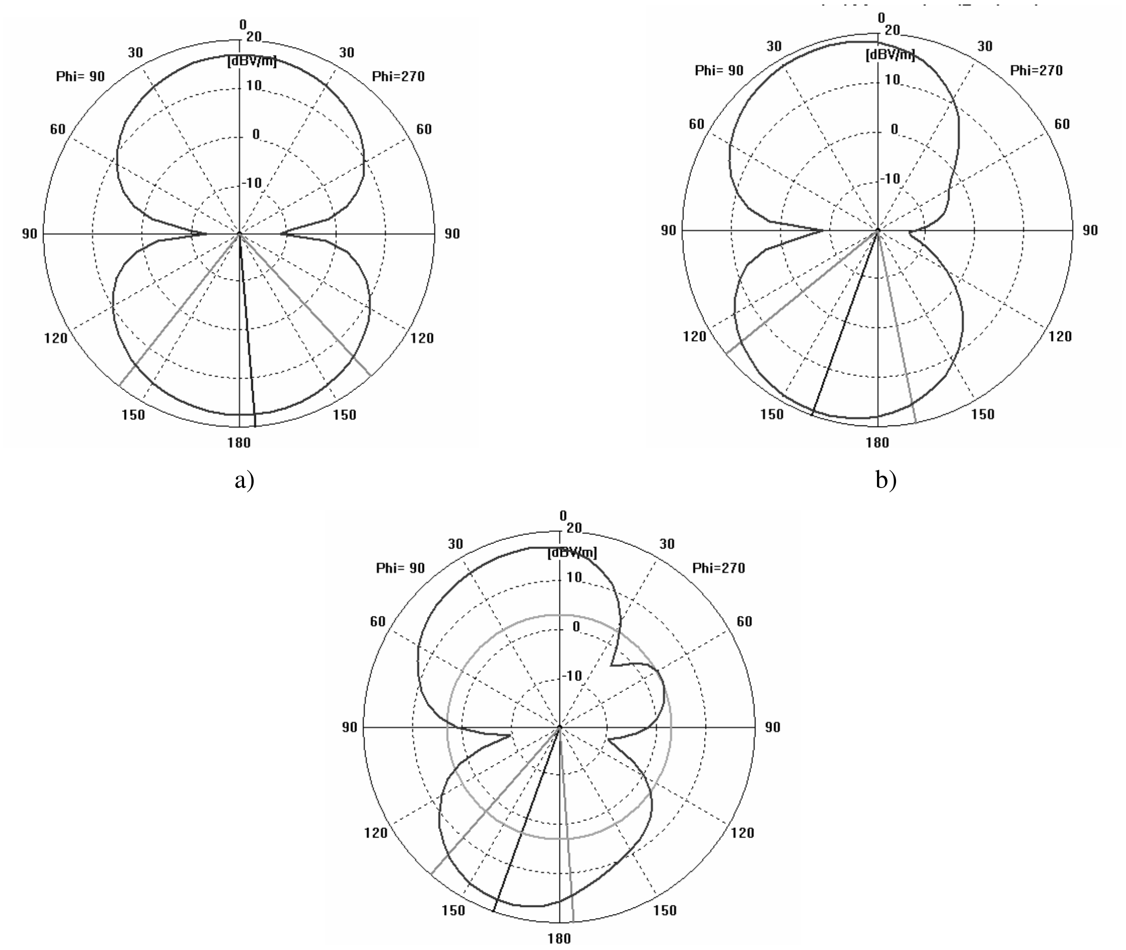

a)

b)

c)

Figure 7.4 - a) 4GHz; b) 9GHz; c) 10GHz : Far field(dBV/m) in E-plane (y-z), sweep of θ angle

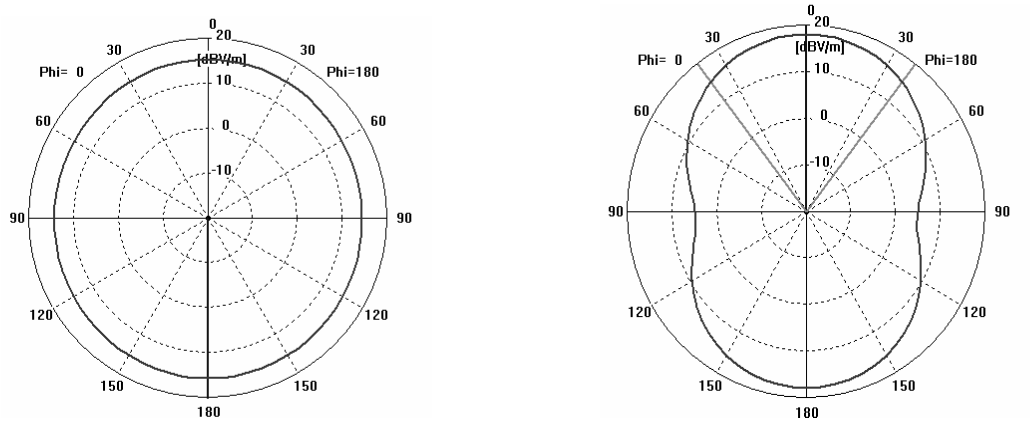

a)

b)

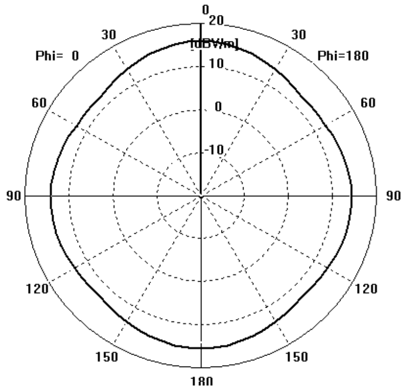

c)

Figure 7.5 - a) 4GHz; b) 9GHz; c) 10GHz : Far field(dBV/m) in H-plane (x-z), sweep of θ angle

7.3 UWB ACTIVE ANTENNA CO-DESIGN

The antenna is now connected to a broadband TWA previously designed with a 50 Ω termination. In fig. 7.6 the TWA directly connected to the antenna is shown. Let us describe this 3-stage traveling wave amplifier. A drain bias line feeds the FET drains in the upper side of the structure; on the lower side, a gate bias line imposes a voltage on the FET gates. Only three lumped components are used: a resistance between the gate bias and the FET on the left, and two capacitances to block the DC current, both at RF input and output. Its meander shape allows to reach very wide bandwidth . The amplifier has approximately 5 ± 1.5 dB gain and -5 ± 1.5 dBm output power at -10 dBm input (fig. 7.7), which is appropriate for UWB applications. At this power level the TWA operates at or below the 1-dB gain compression point across the entire 3.1 – 10.6 GHz band.

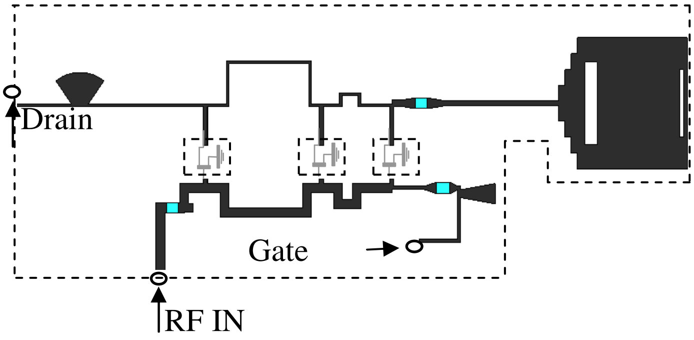

Fig. 7.6 – Top view of the amplifier-antenna subsystem layout.

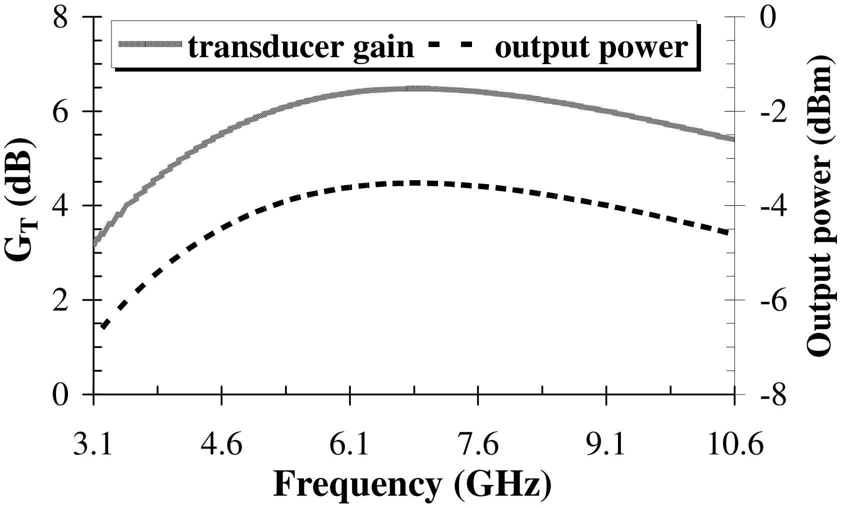

Fig. 7.7 – Transducer gain and output power of a 3-stage traveling-wave amplifier at -10 dBm input.

The far-field performance of the active antenna in such conditions is reported in fig. 7.8 (“50-ohm match” curve), and is found to be rather poor. The power density exhibits a large ripple across the band (over 10 dB), and drops sharply when each band edge is approached. No significant improvement can be obtained by re-optimizing the amplifier for conjugate match to the actual antenna impedance (“conjugate match” curve in fig. 7.8). We thus have to resort to a different design philosophy for the TWA/antenna assembly in order to produce a constant radiated power density with limited ripple (say, of the order of ± 1 dB) all over the band.

The proposed problem has several peculiar aspects. The far-field power density level is a combined effect of three contributions, namely, 1), the amplifier gain, 2), the power transfer between amplifier and antenna, and, 3), the antenna gain. For a consistent design, we need a figure of merit allowing the best tradeoff among such quantities to be directly established. This implies that individual specifications on 1) to 3) *should not* be imposed, otherwise the problem would be over-constrained. In addition, depending on the TWA layout, EM couplings may exist between the antenna and the amplifier (especially the gate and drain transmission lines) which may influence both the power transfer and the radiation pattern. In such cases, we do not have a well-defined interface between antenna and amplifier, and the subsystem may only be analyzed by coupled nonlinear/EM techniques.

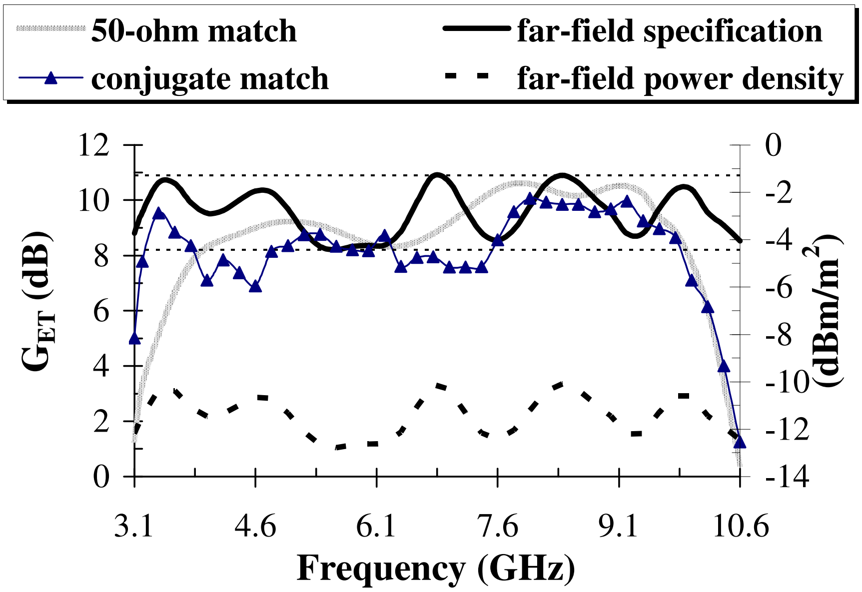

Figure 7.8 : Electromagnetic-transsducer gain and far-field power den-sity at r_L = 1 km for a UWB active antenna (-10 dBm input).

Based on the above ideas, the design procedure is organized as follows. The amplifier nonlinearities are handled by the piecewise harmonic-balance (HB) technique. The active antenna is described as the interconnection of a linear subnetwork including the amplifier and antenna layouts, and of a number of nonlinear devices (MESFET's). The design variables are the layout parameters of both. The linear subnetwork has n_D device ports for connection to the transistors, and one RF input port. There is no output port, though, since the system output is represented by the radiated field. The RF excitation is simply described as a voltage source with impressed voltage U_G and internal impedance R_G. For a given set of layout parameters and a given angular frequency ω, the EM analysis of the linear subnetwork provides its admittance matrix **Y**(ω) and the normalized far-field pattern $\mathbf{e}_i(\theta, \phi; \omega)$ associated with a unit-voltage excitation of the i-th LS port $(1 \leq i \leq n_D + 1)$. Making use of **Y**(ω) an HB analysis is carried out with a spectrum consisting of a suitable number of harmonics of each fundamental frequency ω of interest to compute the voltage phasors $V_i(\omega)$ at the LS ports. The radiated far field is then

$$\mathbf{E}(r, \theta, \phi; \omega) = \frac{\exp(-j\beta r)}{r} \sum_{i=1}^{n_D+1} \mathbf{e}_i(\theta, \phi; \omega)\, V_i(\omega) \qquad (7.2)$$

where r, θ, ϕ are spherical coordinates with origin in the antenna phase center. If r_L is the receiver distance and θ_L, ϕ_L are the angular coordinates of the link direction, the power density of the field incident on the receiver is given by

$$\frac{\left\|\mathbf{E}(r_L, \theta_L, \phi_L; \omega)\right\|^2}{2\eta} = \frac{\left\|\sum_{i=1}^{n_D+1} \mathbf{e}_i(\theta_L, \phi_L; \omega)\, V_i(\omega)\right\|^2}{2\eta\, r_L^2} \tag{7.3}$$

where η is the free-space wave impedance.

In order to define G_T, we now have to compare (7.3) with a reference quantity corresponding to a unit-gain situation [36]. The logical reference is the power density generated by a unit-gain amplifier fed by the same RF source and ideally matched both to the source and to a unit-gain antenna (isotropic radiator). This quantity is given by

$$\frac{\left\|\mathbf{E_{ref}}(r_L, \theta_L, \phi_L; \omega)\right\|^2}{2\eta} = \frac{\left|U_G\right|^2}{8R_G}\,\frac{1}{4\pi r_L^2} = \frac{\left|U_G\right|^2}{32\pi R_G r_L^2} \tag{7.4}$$

We finally combine (7.2) and (7.3) to get expression (7.4) below.

The amplifier-antenna assembly is now designed for a nominal G_{ET} of 10 ± 1 dB at -10 dBm input, with simultaneous specifications at 38 fundamental frequencies uniformly spaced across the [3.1 – 10.6] GHz band.

$$\begin{aligned} G_{ET} &= \frac{\left\|\mathbf{E}(r_L, \theta_L, \phi_L; \omega)\right\|^2}{\left\|\mathbf{E_{ref}}(r_L, \theta_L, \phi_L; \omega)\right\|^2} = \\ &= \frac{16\pi R_G}{\eta\left|U_G\right|^2}\left\|\sum_{i=1}^{n_D+1} \mathbf{e}_i(\theta_L, \phi_L; \omega)\, V_i(\omega)\right\|^2 \end{aligned} \tag{7.5}$$

The design variables are the antenna layout parameters shown in fig. 7.2 a) and the widths and lengths of the TWA transmission lines. 4 harmonics plus DC are used for each HB analysis. The optimization algorithm is a modified space-mapping technique as discussed in [34]. The overall design process takes about 16 hours on a 3 GHz PC and requires a total of 37 EM analyses. The optimized system has a G_{ET} of 9.5 ± 1.5 dB as shown in fig. 7.8, which represents an excellent result for a [3.1 – 10.6] GHz bandwidth. The final G_{ET} is plotted in fig. 7.8 (“far-field specification” curve) together with the far-field power density. The resulting performance is very well behaved, and in particular an effective control of the gain roll-off at the band edges is observed.

In conclusion, this chapter presents a new co-design methodology for ultra-wideband integrated antenna design. The main concept to point out is that the transmitter and antenna cannot be separately handled, and they must be analyzed as a whole. The initial specification in terms of gain has been achieved; the final assembly, realized following the new methodology, clearly shows a flat gain in broadside direction across the entire bandwidth.

.

8.1 CONCLUSIONS

A general and rigorous link analysis approach, based on nonlinear circuit analysis coupled to full-wave electromagnetic simulation, has been presented, and it has been applied to several link case studies.

First of all, in chapter 3 a circuit-level nonlinear/EM analysis of a single IF-to-IF link under modulated drive has been developed. The method simultaneously takes into account two fundamental issues, that is, the antennas EM behavior and the transmitter and receiver front end nonlinearities. I underline that EM analysis is used *once for all* to characterize the signal transfer from the transmitter to the receiving antenna; subsequently, envelope-transient HB is then used to compute the system response at the circuit level. The CPU time is obviously longer than with behavioral models but is still quite affordable, so that a good tradeoff between cost and accuracy is achieved.

A natural extension to an End-to-End link analysis has been carried out in chapter 4 . The most important feature regards the BER computation, which has been made possible by resorting to an artificial neural network approach. The capability of the extended method is particularly interesting for RF designers. It may provide a rigorous check of the system-level link budget, developed at the beginning of the project, before prototyping. Two drawbacks are present: first of all, simulation time is relatively high; secondly, this is an IF-to-IF circuit-level technique, whereas baseband circuits are treated at a system-level. However, to overcome the first one, it is believed that simulation time can significantly be reduced in the next years thanks to the advances in PC calculation capability. As for the second issue, an effective solution is already available, and it is presented in the next paragraph.

A critical aspect in the link computation consists in the propagation environment. Chapter 5 shows how is possible to integrate it in the previously developed procedure. Antennas are EM characterised once for all, and their impedances and far-field quantities are treated by a Ray-Tracing approach. The latter, again *once for all*, characterizes the propagation of the signal along a realistic scenario. Then, the powerful nonlinear tool integrates the Ray-Tracing output, in order to carry out the circuit-level analysis. Interesting case studies have been shown in a realistic propagation environment.

Chapter 6 is devoted to show a new extension of the method to multiple-input-multiple-output systems, which lead the way in the wireless communications. The set of transmitters is treated as a unique nonlinear system loaded by the multiport antenna, and is analyzed by nonlinear circuit techniques. In order to establish the connection between transmitters and receivers, the far fields incident on the receivers are evaluated by EM analysis and are combined by extending to the MIMO case an available ray tracing technique. On the receiver side, EM theory is used to describe the receiving array as a linear active multiport network. As in chapter 4, the computation of BER performance at the circuit level is demonstrated. In the end, the most important and undoubted novelty of the approach consists in the capability to precisely account for mutual coupling on both the frequency-dependent *near-field* and *far-field* performance of each radiating element.

Chapter 7 gives another hint on the advanced capabilities developed by the proposed Co-design technique, applied to ultra-wideband systems. In conclusion of that chapter, I ended up with the affirmation that transmitter and antenna cannot be separately designed; if so, the goal, which often consists in reaching a uniform far-field value over the entire bandwidth, is hardly achievable. On the contrary, the co-design of both RF devices lead to straightforward results, and this is a key aspect to account for within the scope to simulate the whole ultra-wideband link.

8.2 FUTURE WORK

It is noteworthy that a complete UWB link simulation would be an absolute novelty in the microwave techniques world. In this way, the future work must be developed following two paths.

First, the transmitting part here considered represents only a part of an ultra-wideband link. So, the receiver side will be characterized utilizing a broadband low-noise amplifier, such as [37], which will be excited by radiated pulse. In a first step, the channel model will be ideal, afterwards it may be utilized a deterministic UWB channel model.

As for the second path, time will be devoted to simulate an ultra-wideband link according to the direct-sequence approach [38], (i.e. the pure UWB transmission approach, which is in contrast with OFDM approach); at the beginning, this will be done under sinusoidal excitation. But the actual keystone regards the most significant and promising UWB challenge, and it consists in performing an accurate link simulation *under nanosecond pulse drive*. For this purpose, MHB technique is not suitable anymore. In fact, no carrier can be identified in UWB systems studied with DS-approach, and therefore the MHB quasi-periodic approximation in (2.8) is not meaningful. On the contrary, a traditional linear convolution must be implemented, according to §2.4 in [28]. Going into details, an UWB electronic pulse generator creates the nanosecond pulse, which is amplified by a nonlinear system, typically a broadband TWA, whose linear subnetwork response is calculated through the above mentioned linear convolution. Practically, a time-domain system response to an impulsive excitation must be directly calculated. At this stage, the pulse is transmitted by a suitable ultra-wideband antenna. On the receiving side, dual operations are going to be performed. In this way, it's possible to end up with a complete link characterization through the usual index of performances, such as BER.

8.3 PHILOSOPHY OF THE WORK AND GENERAL PERSPECTIVES

As final considerations, hereby I would like to clearly explain the underlying philosophy of the work carried out, and to give some perspectives.

For instance, the method proposed has to be intended as a reference frame for the system-level analysis tools. They are obviously faster than the technique proposed; nevertheless, some aspects of it are now essential, especially for high-frequency systems. In fact, there is hardly any alternative to EM analysis if the effects of real-world antenna systems, or couplings between several parts of baseband and RF circuit, must be accounted for.

Therefore, a higher-level simulation tool, such as the one proposed, is an effective candidate in order to establish how the numerous approximations implied by ordinary system-level analysis affect the overall accuracy.

The obvious comparison is with circuit analysis techniques for high frequencies. Twenty years ago EM analysis was essentially a research topic for academic people, and most designers confined themselves to the use of circuit techniques, possibly including quasi-static models for simple discontinuities. At that time, the proposal of an all-electromagnetic design procedure would have most likely produced a wealth of skeptical comments. Right now circuit techniques are still universally in use, *but* almost everybody in the world would check his/her final design with EM analysis before going to fabrication. I believe that the same might become true with system design.

Meanwhile, the advent of more and more sophisticated and efficient nonlinear simulation algorithms is likely to greatly improve the usability of this approach in the years to come. In addition, two aspects have to be underlined. First, I think circuit-level link analyses are going to be extremely helpful within the scope to construct link behavioural models as accurate as possible. In the future, this will satisfy the RF designers request to have powerful and flexible tools, in order to rigorously and quickly characterize a telecommunication link. Second, the utilization of DHB algorithms will make possible a faster circuit-level simulation for both logical and analog parts of the link; thus, a rigorous co-simulation of all the large-size baseband nonlinear transceiver sections, as well the RF circuitry, including antennas and channel, will be allowed in a short time.

A.1 INTRODUCTION

In this appendix A, I would like to show an application of a co-design technique suitable to handle a reconfigurability issue. The study has been carried out in a 5-month stage at E.N.S.T.A. in Paris, in cooperation with U.E.I. research group.

For instance, a "reconfigurable" antenna is a radiating element whose frequency behaviour can change according to a logic configuration, obtained by a set of devices placed before the antenna. Usually these kind of devices are well known as RF "switches". It is worth mentioning the advantages obtained by using such approach in modelling antennas, instead of making use of traditional multi-band antennas: first, the signal radiated from the antenna is more reliable; in fact, a reconfigurable antenna reaches deepest resonances with respect to multi-band antennas: while the latters need to occupy a larger bandwidths, and therefore their Q value is low, the formers reach high Q values. Secondly, a reconfigurable antenna is more robust to interference or spurious signal, than a multi-band one. Let us suppose that N is number of switches, M the number of states of the switch; thus, M^N the number of the possible configurations of the antenna; let us assume i,j two index ($i=1,\ldots, M^N$; $j=1,\ldots, M^N$; $i \neq j$). Whenever the i-th configuration is active, 1 or more resonances are presented by the antenna, whereas the resonances obtained by each j-th configuration are not present. In such a way, any spurious signal at the j-th configuration is rejected by the antenna, and the robustness to interference higher. Finally, the last advantage is the ability to comply with future standards through updates.

Considering the trend to offer multiple services in the same terminal (GSM900, GSM1800, WIMAX, Bluetooth, UMTS, GPS…), I started this work within the scope to outline a methodology for the Co-design of a reconfigurable antenna, able to cover some of these services. In this case study, the antenna is capable to work at GSM900, GSM1800 and WIMAX frequencies, when connected to a real RF switch. The target bandwidth at -6dB (typical for mobile communications) are: 890-915 MHz for GSM900; 1710-1785MHz for GSM1800; 3.4-3.6GHz for WIMAX.

In order to outline this methodology, four main steps have been done:

- design of the reconfigurable antenna;
- measures of the switch;
- outline of the co-design methodology.

A.2 RECONFIGURABLE ANTENNA DESIGN

In the first part of the stage, I modelled a planar inverted-F reconfigurable antenna. It is a metallization trace suspended on a printed circuit board (PCB) ground plane, with a feeding pin and a small shorting wall. This antenna, shown in fig. A.1,A.2,A.3 presents two configurations: the first one shows two interesting resonances at 900MHz and 1800MHz frequency, for GSM frequencies; the second one shows a main resonance in the WIMAX band (3.4-3.6GHz). The difference between the two configurations is given by an additional shorting pin (circled in fig. A.1). In the former one, that pin creates a conductive path for the current, from the trace to the PCB. In the latter one, the pin is not connected. The switch is now represented as an ideal wire (radius 0.4 mm) . The feeding point is the “XF” circled point in fig. A.3. More in details, in the **configuration “on”** this wire is connected to the ground. In the **configuration “off”,** it is not connected.

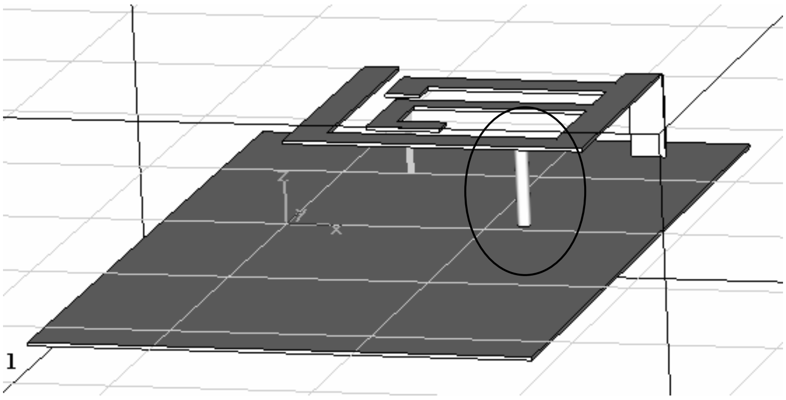

Figure A.1: Perspective view of PIFA antenna with PCB (shorting pin circled)

L1=29mm; L2=30.2mm; L3=L1; L4=21.8mm; L5=3.7mm; L6=3.1mm; L7=10.7mm; L8=5.2mm; L9=20.1mm; L10=10.5mm; L11=7.6mm; W1=3.5mm; W2= 2.5mm; XF= 5mm; YF= 21.8mm; XV= 23.5mm.

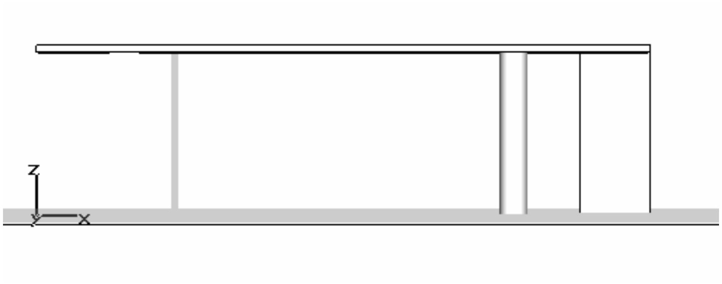

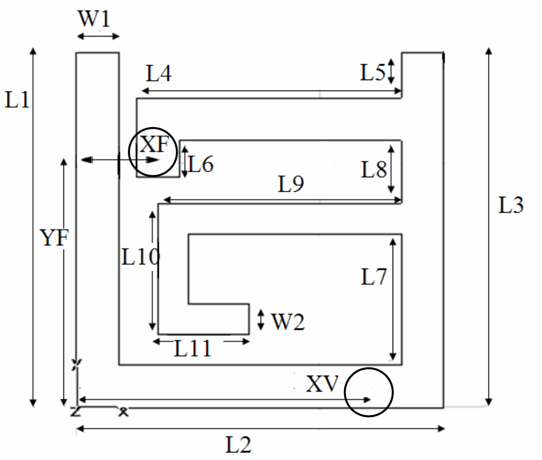

Figure A.2: antenna with PCB side view (x-z cutting plane) Figure A.3: antenna top view

The following graphs show the performances of the reconfigurable antenna. Fig. A.4 shows the |S11| in the "ON" state, in the WIMAX band. Fig. A.5 shows the power density flow along the trace: the feed is the point where most of the power is concentrated; the resonance is given by the coupling between the feed and the left metallization. The antenna presents circular polarization, with a 3.5 dB gain. In fig A.6-A.7, E-plane and H-plane are shown (the antenna lies in x-y plane).

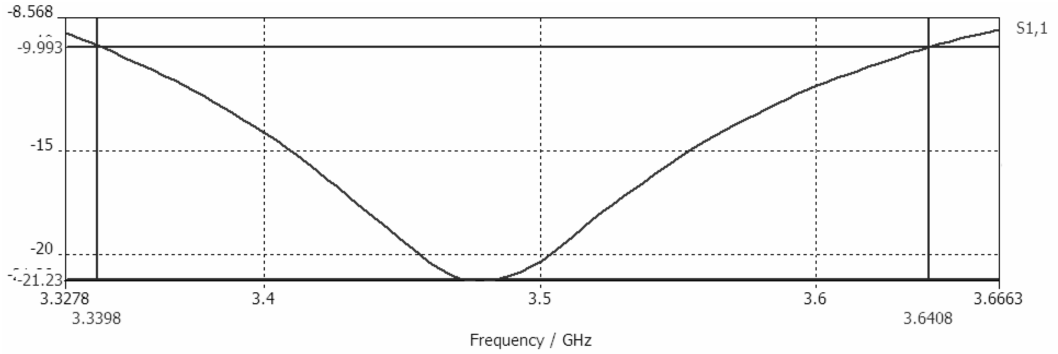

Figure A.4: |S11| (dB) zoom in Wimax band

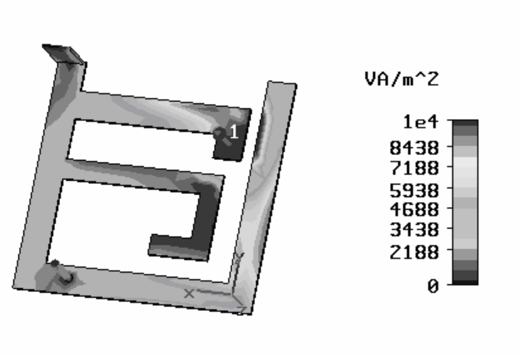

Figure A.5: Power density flow @ 3.5GHz

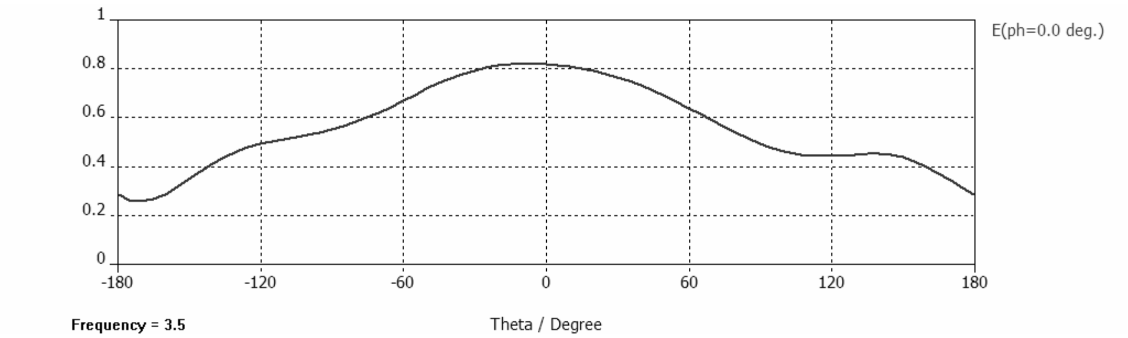

Figure A.6: E-field (V/m) in x-z plane @ 3.5GHz

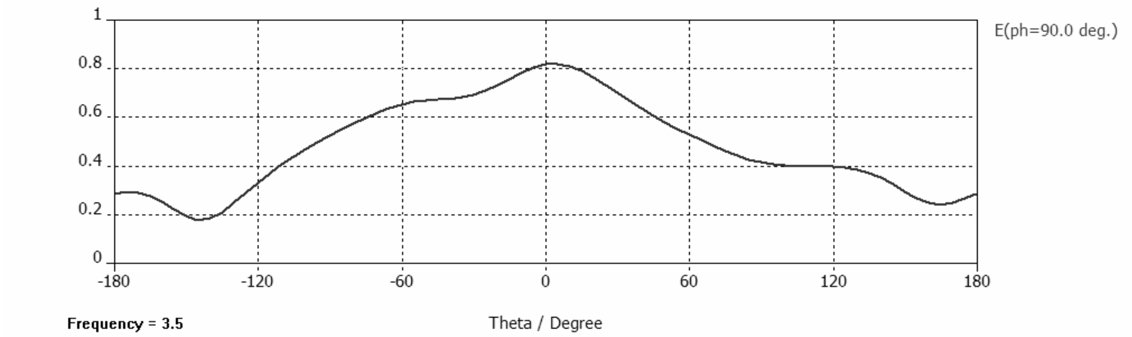

Figure A.7: H-field (V/m) in y-z plane @ 3.5GHz

Let us switch to the "OFF" state. Figs. A.8-A.9 show the |S11|, at GSM900 frequency. The GSM900 and GSM1800 simulated bandwidth are 27 MHz and 85 MHz, respectively . Fig. A.10-A.11 show the power density flow along the trace: note that the lower resonance is approximately given by the sum of external length (fig. A.10) ; on the contrary, the higher resonance is given by the central trace length (fig. A.11) . The antenna presents circular polarization, with a -0.2 dB gain @0.903GHz, and 4.1 dB gain @1.77GHz. Those gains are not surprising, but ordinary values for GSM mobile communication antennas. In fig A.12-A.13, E-plane and H-plane for GSM900 frequency are shown, and in fig. A.14-A.15, the same planes are plotted for GSM1800.

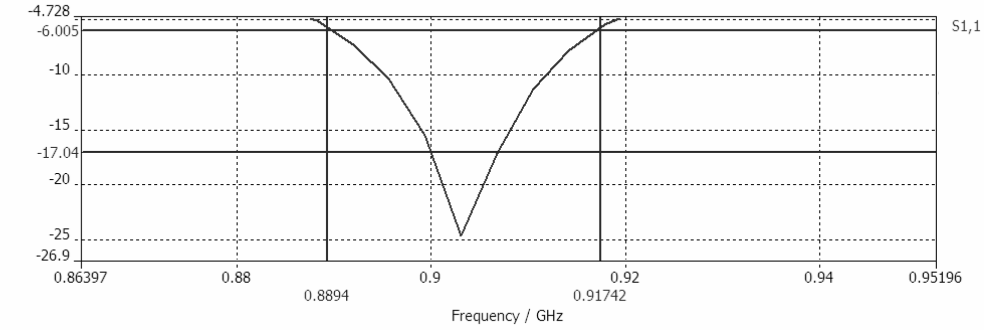

Figure A.8: |S11| (dB) zoom in GSM900 band

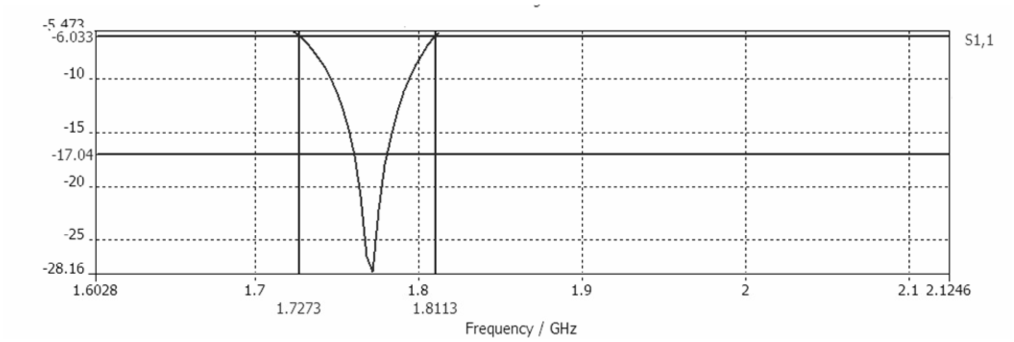

Figure A.9: |S11| (dB) zoom in GSM1800 band

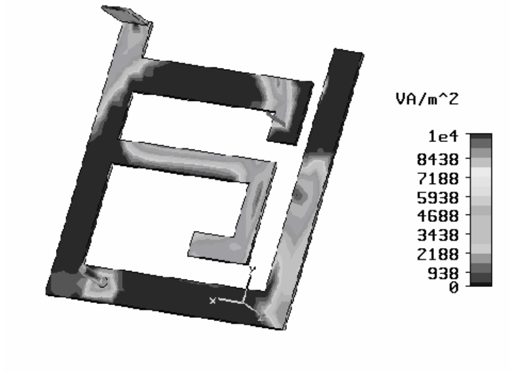

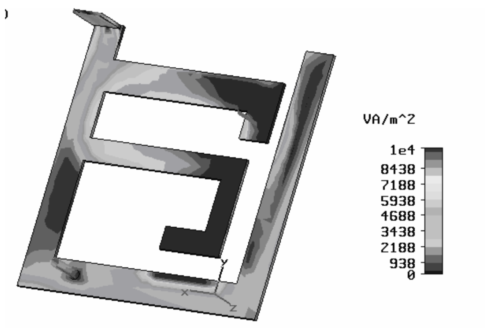

Figure A.10: Power density flow @ 0.903GHz

Figure A.11: Power density flow @ 1.77 GHz

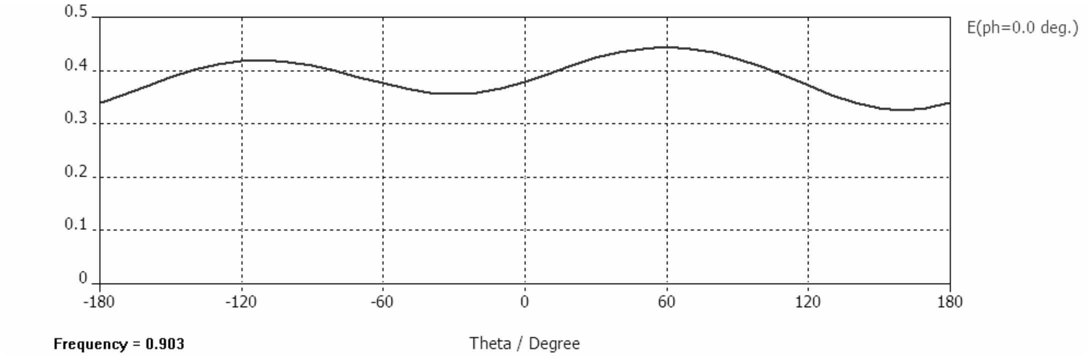

Figure A.12: E-field in x-z plane @ 0.903 GHz

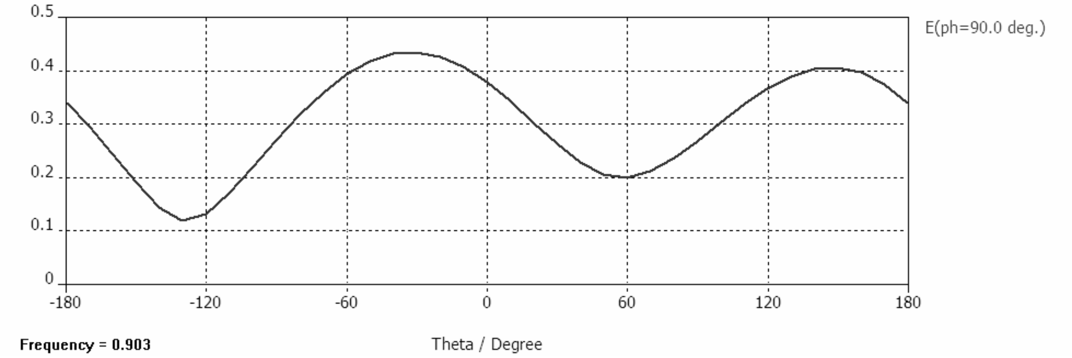

Figure A.13: H-field in y-z plane @ 0.903 GHz

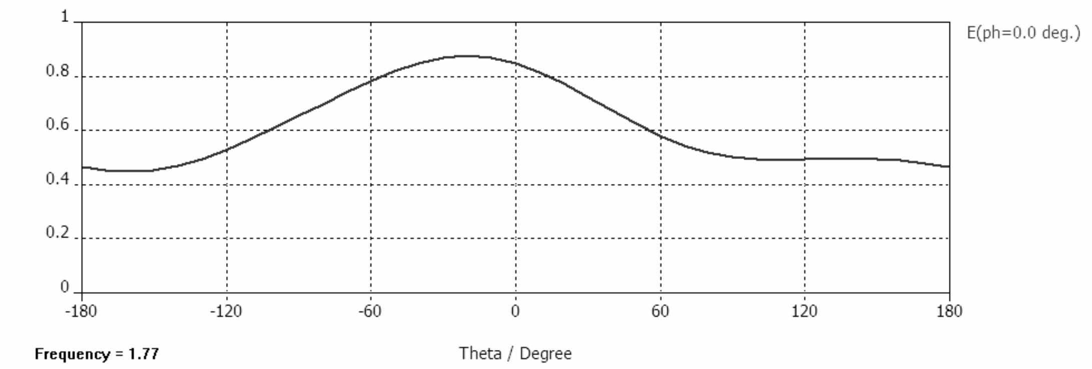

Figure A.14: E-field in y-z plane @ 1.77 GHz

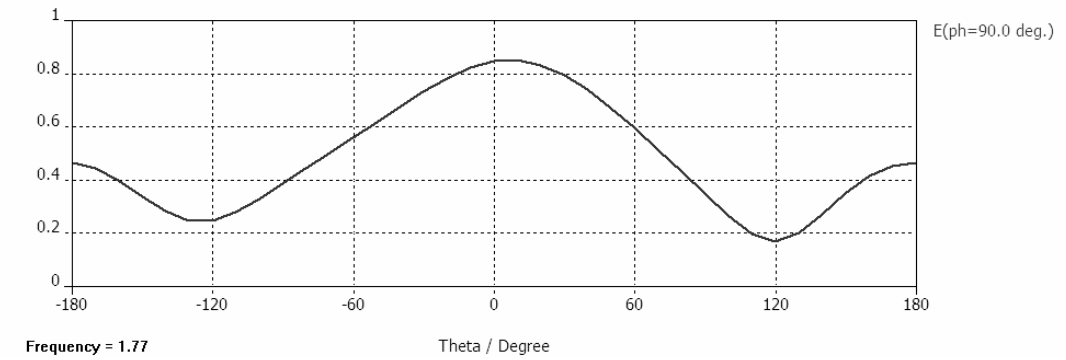

Figure A.15 : E-field in x-z plane @ 1.77 GHz

Both WIMAX and GSM900-1800 antennas have been fabricated, and their layouts are represented in fig. A16,A.17, respectively.

Figure A16: WIMAX antenna

Figure A.17 : GSM900-1800 antenna

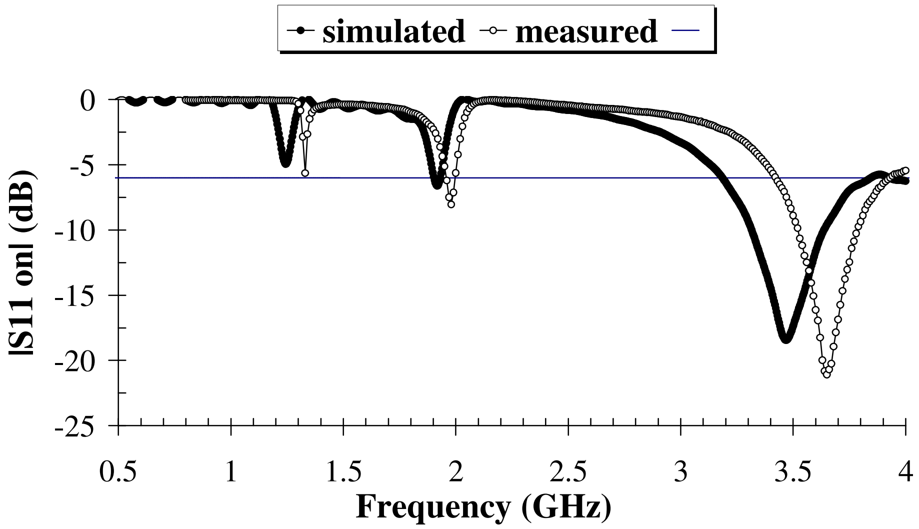

Figure A.18 : Comparison between measured results and simulated.

As for the comparison between measured and simulated results, a discrete agreement for the “ON” state is obtained: 130-MHz shift at Wimax may be observed in fig. A.18. Anyway, in 3.4-3.6 GHz bandwidth, the antenna is under the -6dB threshold. The discrepancy is mostly due to technological asymmetries in the fabrication. In “OFF” state, 20-MHz shift and 60MHz shift have been observed for GSM900 and GSM1800 frequencies, as in fig. A.19.

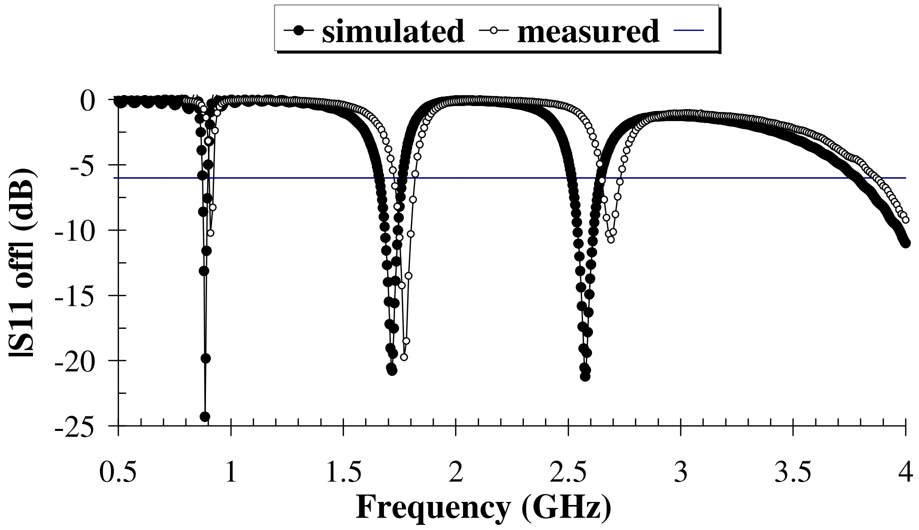

Figure A.19 : Comparison between measured results and simulated.

.

A.3 RF-SWITCH MEASURES

At this stage, a real SW-439 RF-switch has been characterized, in order to replace the ideal wire. In fig. A.20, it is mounted on a test board. The S-matrix of the de-embedded switch is presented in the following graphs. Figs. A.21, A.22 show the S11 and S21 of the “ON” switch respectively. As it may be observed, they show good performances. The matching, plotted in fig. A.21, is always under -12.5dB. As for GSM900 and WIMAX frequencies, the matching is always better than -20 dB, while it’s –13dB for GSM1800 frequency. Moreover, almost no losses occur during the transmission (fig. A.22), so that the device *insertion loss* (equal to |S21|^2) is low.

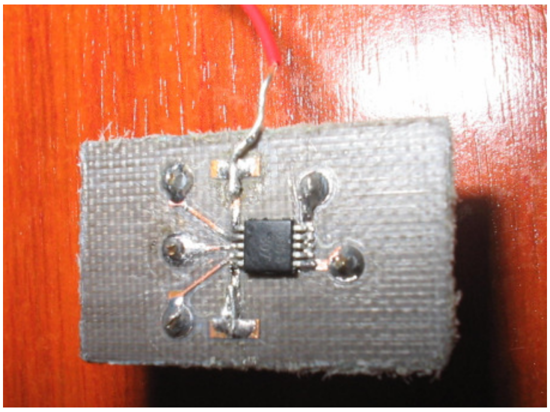

Figure A.20:RF-SWITCH test board

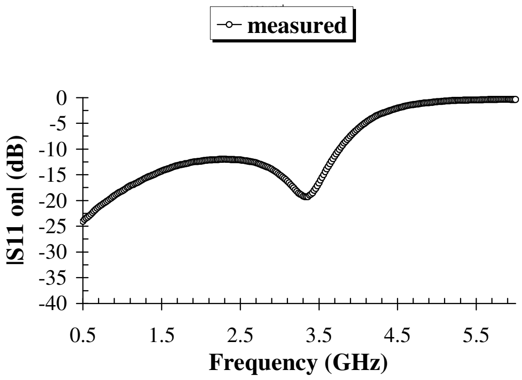

Figure A.21: |S11| (dB) –“ON”

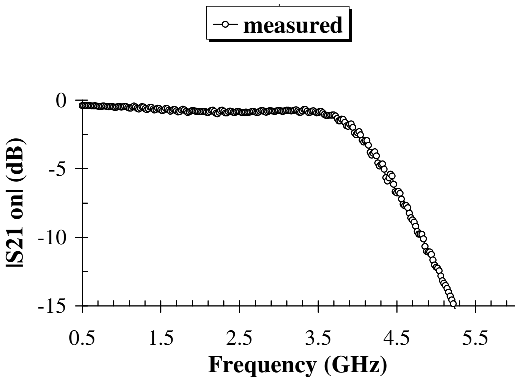

Figure A.22: |S21|(dB) –“ON”

When the switch is “OFF”, some losses are present during the insertion, as in fig. A.23; on the contrary, the isolation, defined as -|S21|, is always excellent (fig. A.24) up to 3.6GHz.

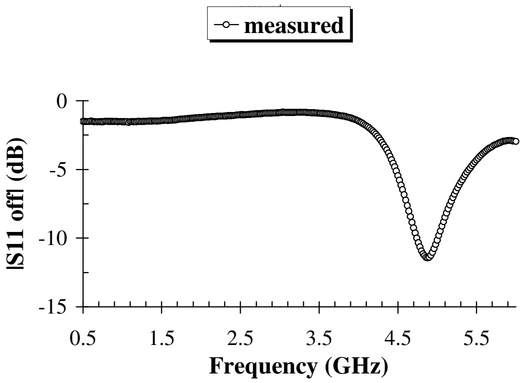

Figure A.23 : |S11|–"OFF"

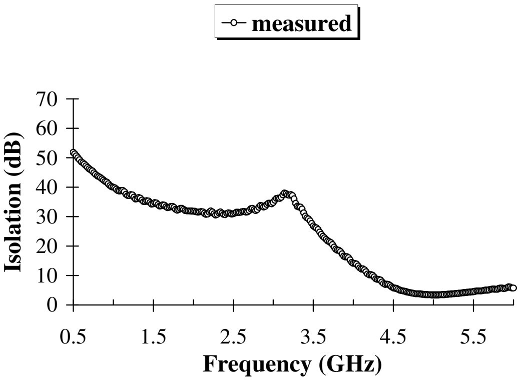

Figure A.24: isolation–"OFF"

A.4 OUTLINE OF A CO-DESIGN METHODOLOGY

In the last phase of the project, a Co-design methodology for the design of the overall system switch-antenna has been setup. For instance, throughout S-matrix connection, antenna and switch have been connected in the "OFF" state (fig. A.25) . If only a small shift for GSM1800 frequency occurred, unfortunately a suppression of GSM900 frequency was observed (fig. A.26). Then, the antenna has been connected to the switch in the "ON" state. It appeared, in fig. A.27, that WIMAX frequency had to be clearly re-tuned, because it has been shifted by 260MHz.

The result obtained underlines the importance to define a Co-design technique: the two separate systems, once merged together, do not work properly as they do in the "stand-alone" configuration. Moreover, this affirmation confirms the conclusions at the end of chapter 7.

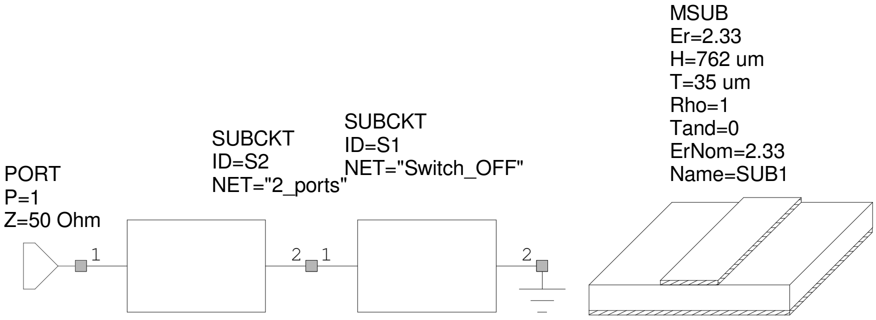

Figure A.25: direct "OFF" connection

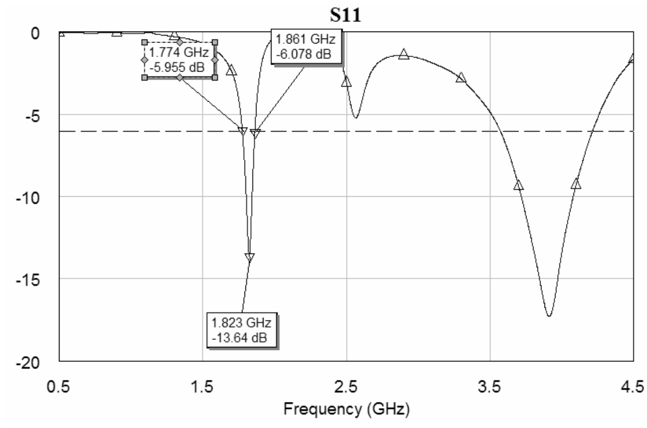

Figure A.26: |S11|(dB) - “OFF”

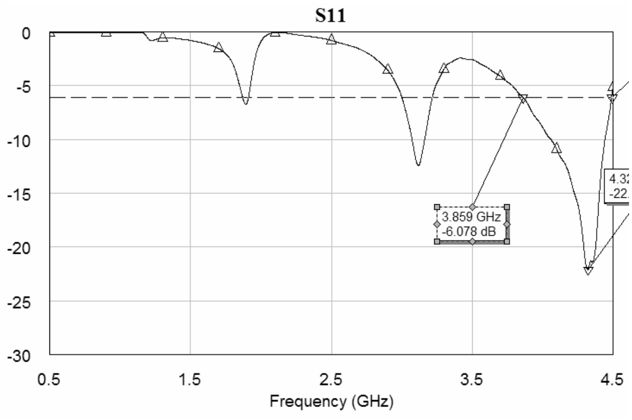

Figure A.27: |S11|(dB) – “ON”

At this stage, the keystone was given by the idea of decoupling the matching problem. That has been possible because of the high isolation in the “OFF” state. The idea can be explained as follows. First of all, it’s possible to model a matching network between the antenna and the switch; such network will reproduce “OFF” state, i.e. it will make the “OFF” switch see two open circuits at GSM900 and GSM1800. Nevertheless, it will affect the remaining configuration as well.

Once designed this network, a new one adjusts the “ON” configuration. The second one must be put between the RF switch output and ground; in this way, it doesn’t affect the “OFF” configuration, since the switch is well isolated.

It is noteworthy that this solution involves no re-design of the antenna.

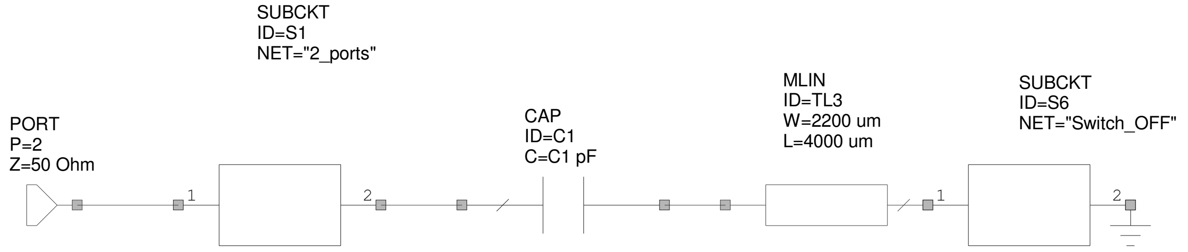

Figure A.28: Matching circuit for the “OFF” circuit

The solution found in fig. A.28 involves only a 2x4 mm metallization, with a 0.6pF series capacitance. The |S11| is shown in fig. A.29, and it reproduces the measured curve in fig. A.19. Specifications are fulfilled for GSM900 (25 MHz, 890-915MHz) and for GSM1800 (90 MHz reached, 1705-1795 MHz).

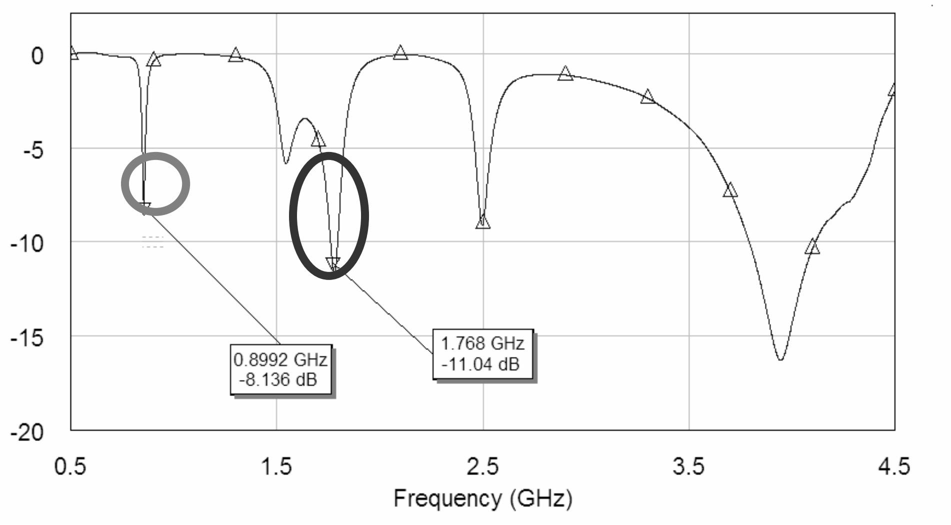

Figure A.28: Final |S11| for the “OFF” configuration

The second network, placed after the switch turned on, consists in a simple stub 2.2x6.5 mm. The overall diagram block is now represented in fig. A.29. It is noteworthy that ground, initially placed after the switch output to simulate the ideal pin connected in “ON” state, is nomore needed. On the contrary, an open stub match the preceding circuitry to the shortcircuit. The reason lies in the non-ideality of the switch, which introduces phases mismatch to be compensated for.

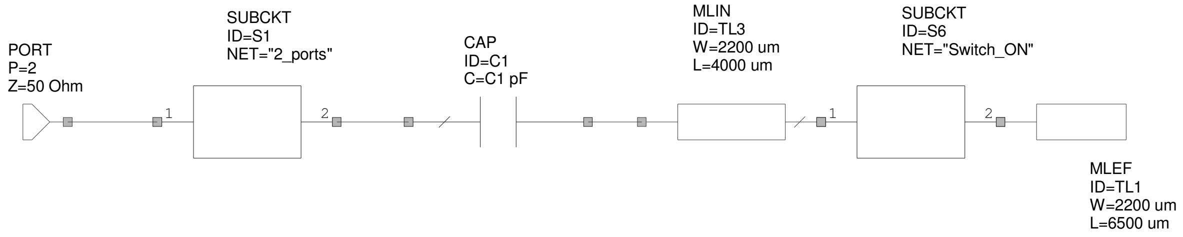

Figure A.29: final configuration, switch “on”

In this way, WIMAX requirements are satisfied. In fig. A.30, the covered bandwidth at -6dB is more than 200 MHz, with a central frequency of 3.3GHz.

In conclusion, two antenna prototypes have been invented and fabricated, and the measured results are slightly different from the simulated ones. Measures on a real RF-switch have been performed. After that, a precise methodology has been setup in order to tackle antenna-switch connection issues. Therefore, a complete study on the antenna-switch interactions has been performed, with interesting simulated results produced after the matching network design.

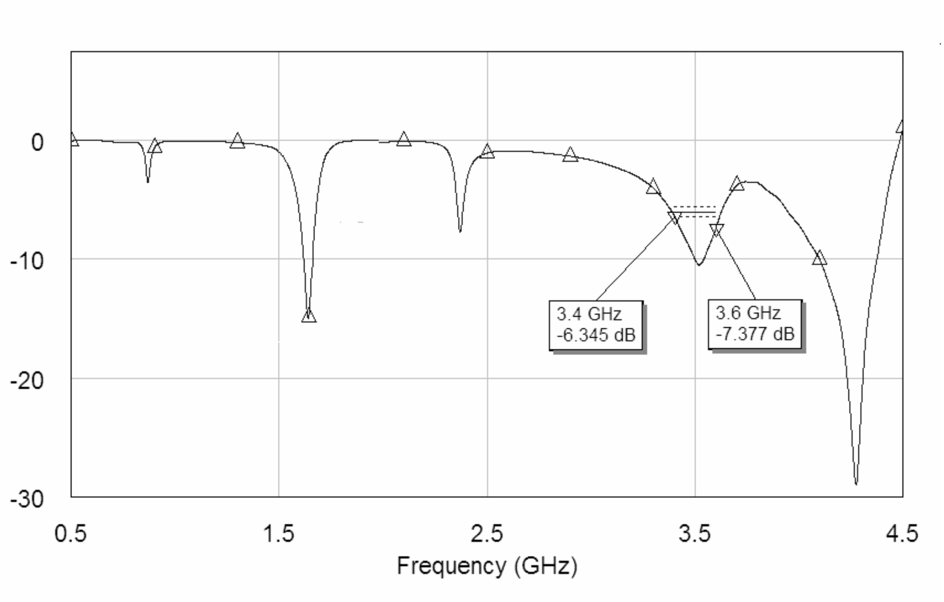

Figure A.30: Final |S11| for the "ON" configuration

Complete works on reconfigurable antennas has been presented in [39],[40]. In particular, the last one shows an application of a PIFA reconfigurable antenna for multiple services, using the same concept developed in this work.

APPENDIX B : COMPLEX ENVELOPE SIGNALS

This short appendix clarifies the expression of the voltage complex envelope in time-domain, env(t). Let us assume that A(t) and $\Psi(t)$, complex envelope absolute value and phase, are the well known modulation laws; ω_m and ω_o are respectively the half-bandwidth and the central angular frequency of the signal as in (4.1)

$$\omega_m = \frac{\omega_2 - \omega_1}{2} \qquad \text{(B.1)}$$

$$\omega_o = \frac{\omega_2 + \omega_1}{2}$$

Then it's possible to hold that a modulated signal sm(t) is related to complex envelope A(t) $e^{-j\psi(t)}$ through (4.2)

$$\mathrm{sm}(t) = \Re e(A(t) \cdot e^{-j\Psi(t)} e^{j\omega_o t}) \qquad \text{(B.2)}$$

where A(t) $e^{-j\psi(t)}$ = env(t) can be expressed as (4.3) and $\chi(\omega)$, phase deviation, as (4.4)

$$A(t) \cdot e^{-j\Psi(t)} = \int_{-\omega_m}^{\omega_m} V(\omega_o + \omega) \cdot e^{j(\omega t - \chi(\omega))} d\omega \qquad \text{(B.3)}$$

$$\chi(\omega) = \phi(\omega_o + \omega) - \phi(\omega_o) \qquad \text{(B.4)}$$

where V is the voltage spectrum. Therefore, by looking through (4.2), a modulated signal can be obtained through an amplitude and phase modulation on a carrier. From (4.3), it turns out that a complex envelope is a baseband signal, and it's obtained by translating a pass-band signal centered at f_o central frequency to DC.

The advantage given by the complex envelope representation of the modulated signal is significant. In fact, if a modulated signal had to be analysed by a circuit simulation tool, since it is a radiofrequency signal, all the harmonics over the fundamental frequency would be taken into account. Therefore time-domain analyses would be too heavy, because the timestep, related to the maximum frequency in the circuit, would be very low. On the contrary, since the corresponding complex envelope signal is baseband, the maximum frequency is lower than in modulated case (practically, the maximum frequency is the band upper bound). Therefore, timestep is usually higher than in modulated case, and simulations are much quicker (see §4.5) . This appendix is a short extract from [41].

LIST OF PERSONAL PAPERS

1. V. Rizzoli, A. Costanzo, D. Masotti and P. Spadoni, Circuit-Level Nonlinear/Electromagnetic Co-Simulation of an Entire Microwave Link, *2005 IEEE MTT-S Int. Microwave Symp. Digest*, Long Beach (CA, U.S.A.), June 2005, pp. 813-816.

2. V. Rizzoli, D. Masotti, P. Spadoni, A. Costanzo, and F. Fuschini, "Distortion Analysis of RF Links by Means of Circuit-Level Nonlinear/EM Front-end Simulation and Realistic Channel Description", *2006 36th European Microwave Conference*, Manchester (UK), September 2006, pp 161-164.

3. V. Rizzoli, A. Costanzo, D. Masotti, P. Spadoni, "Prediction of the End-to-End Performance of a Microwave/RF Link by means of Nonlinear/Electromagnetic Co-Simulation", *IEEE **Transactions** on Microwave Theory Techniques*, Dec. 2006, pp. 1149-1160.

4. V. Rizzoli, A. Costanzo, E. Montanari and P. Spadoni, "CAD Procedures for the nonlinear/electromagnetic co-design of integrated microwave transmitters", *2007 IEEE MTT-S Int. Microwave Symp. Digest*, Honolulu (HI, U.S.A.), June 2007, pp. 2031-2034.

5. V. Rizzoli, A. Costanzo, and P. Spadoni, "Computer-Aided Design of Ultra-Wideband Active Antennas by Means of a New Figure of Merit", *IEEE Microwave Components and **Letters**,* to be published in April, 2008.

6. V. Rizzoli, A. Costanzo, P. Spadoni, F. Donzelli, D. Masotti and E. M. Vitucci, "A CAD Procedure for MIMO Link Estimation by the combination of Nonlinear, Electromagnetic and Propagation Analysis Techniques", *2008 IEEE MTT-S Int. Microwave Symp. Digest*, Atlanta (GA, U.S.A.), June 2008, pp not yet available.

ACKNOWLEDGMENTS OBTAINED

7. S. Loizeau, A. Sibille, "Reconfigurable Pifa Antenna with UltraWideband Tuning", EUCAP, Edinburgh, UK. 11 - 16 Nov. 2007.

BIBLIOGRAPHY

[1] T. K. Sarkar *et al.*, “*Smart antennas*”. Wiley Interscience: Hoboken, 2003.

[2] Nuno B. Carvalho, José C. Pedro, Wonhoon Jang, and Michael B. Steer, “Simulation of nonlinear RF circuits driven by multi-Carrier modulated signals”, *2005 IEEE MTT-S Int. Microwave Symp. Digest,* Long Beach, CA, June 2005, pp. 801-804.

[3] V. Rizzoli, A. Costanzo, and G. Monti, “General electromagnetic compatibility analysis for nonlinear microwave integrated circuits”, *2004 IEEE MTT-S Int. Microwave Symp. Digest*, Fort Worth, TX, June 2004, pp. 953-956.

[4] M. Clemens and T. Weiland ,”DISCRETE ELECTROMAGNETISM WITH THE FINITE INTEGRATION TECHNIQUE” , Progress In Electromagnetics Research, PIER 32, 65–87, 2001.

[5] V. Rizzoli, A. Lipparini, A. Costanzo, F. Mastri, C. Cecchetti, A. Neri, D. Casotti, “ State-of-the-Art Harmonic Bilance simulation of Forced Nonlinear Microwave Circuits by the Piecewise Technique”, IEEE Transactions on Microwave Theory and Techniques, VOL. 40, n.1, January 1992, pp. 12-28.

[6] V. Rizzoli, A. Neri, F. Mastri, A. Lipparini, “Modulation-Oriented Harmonic Balance based on Krylov subspaces”, *1999 IEEE MTT-S Digest,* pp. 771-774.

[7] V. Rizzoli, A. Lipparini, D. Masotti, and F. Mastri, “Efficient Circuit-Level Analysis of Large Microwave Systems by Krylov-Subspace Harmonic Balance”, 2001 *IEEE IMS Int. Microwave Symp. Digest*, Phoenix, AZ, May 2001, pp. 25-28.

[8] V. Rizzoli, E. Montanari, D. Masotti, A. Lipparini, and F. Mastri “Domain-Decomposition Harmonic Balance with Block-Wise Constant Spectrum”, *2006 IEEE IMS Int. Microwave Symp. Digest*, San Francisco, CA, June 2006, pp. 860-863.

[9] W. R. Curtice. "Intrinsic GaAs MESFET equivalent circuit models generated from two-dimensional simulation," IEEE Transactions on Computer-Aided Design. vol. 8. pp. 395-402. Apr. 1989.

[10] V. Rizzoli, C. Cecchetti, A. Lipparini, and F. Mastri. "General purpose harmonic balance analysis of nonlinear microwave circuits under multitone excitation," IEEE Transactions on Microwave Theory Technique, vol. 36, pp. 1650-1660, Dec. 1988

[11] V. Rizzoli, C. Cecchetti, and A. Lipparini, "A general purpose program for the analysis of nonlinear microwave circuits under multitone excitation by multidimensional Fourier transform," *Proc. 17th European Microwave Conf.*, Rome, Sept. 1987, pp. 635-640.

[12] E. Ngoya et al., "Efficient algorithms for spectra calculations in nolinear microwave circuits simulators," IEEE Transactions on Circuits Systems, vol. 37, pp. 1339-1355, Nov. 1990.

[13] V. Rizzoli, A. Neri, and F. Mastri, “A modulation-oriented piecewise harmonic-balance technique suitable for transient analysis and digitally modulated signals”, *Proc. 26th European Microwave Conf.* (Prague), Sept. 1996, pp. 546-550.

[14] M. Abramowitz and I. A. Stegun, *Handbook of Mathematical Functions*. New York: Dover, 1965.

[15] V. Rizzoli, F. Mastri, C. Cecchetti, and F. Sgallari, “Fast and robust inexact-Newton approach to the harmonic-balance analysis of nonlinear microwave circuits”, *IEEE Microwave Wireless Components and Letters*, Vol. 14, July 2004, pp. 349-351.

[16] V. Rizzoli, E. Montanari, A. Lipparini, F. Mastri and D. Masotti, “A fully automatic domain partitioning technique for the efficient circuit-level simulation of large nonlinear microwave subsystems"”, *IEEE Microwave Guided Waves Lett.*, Vol. 7, Oct. 1997, pp. 359-361.

[17] V. Rizzoli, A. Costanzo, and F. Mastri, "Analysis of digitally modulated steady states nonlinear circuits by Krylov-subspace harmonic-balance", *Proc. European Conf. Circuit Theory Design* (Helsinki), Aug. 2001, pp. II/197-II/200.

[18] E. O. Brigham, “*The fast Fourier transform and its applications*”. Prentice-Hall: Upper Saddle River, 1988.

[19] J. Liu, A. Bourdoux, J. Craninckx, B. Come, P. Wambacq, S. Donnay, and A. Barel, “Impact of front-end effects on the performance of downlink OFDM-MIMO transmissions”, *IEEE 2004 RAWCOM*, pp. 159-162.

[20] K. S. Narendra and K. Parthasarathy, “Identification and control of dynamical systems using neural networks”, *IEEE Trans. Neural Networks 1 (1)*, 1990, pp. 4-27.

[21] M. Kimura and R. Nakano, “Learning dynamical systems by recurrent neural networks from orbits”, *Neural Networks 11* (1998), pp. 1589-1599.

[22] H. E. Rowe, *Signals and noise in communications systems*. Van Nostrand: Princeton, 1965.

[23] V. Rizzoli, C. Cecchetti, and F. Mastri, "A rigorous frequency-domain approach to large-signal noise in nonlinear microwave circuits", *IEEE Microwave Guided Waves Lett.*, Vol. 8, June 1998, pp. 220-222.

[24] C. A. Balanis, *Antenna Theory and Design*. Harper and Row: New York, 1982.

[25] T. J. Brazil, “Accurate and efficient incorporation of frequency-domain data within linear and non-linear time-domain simulation”, *2005 IEEE MTT-S Int. Microwave Symp. Digest*, Long Beach, CA, June 2005

[26] V. Degli-Esposti *et al.*, “An advanced field prediction model including diffuse scattering”, *IEEE Trans. Antennas Prop.*, vol. 52, July 2004, pp. 1717-1728.

[27] V. Rizzoli, A. Costanzo, M. Rubini, and D. Masotti, "Investigation of Interactions Between Passive RFid Tags By Means of Nonlinear/EM Co-Simulation", *Proc. 36th Europ. Microwave Conf.*, Sept. 2006, pp. 722-725.

[28] V. Rizzoli, A. Neri, F. Mastri, and A. Lipparini, "A Krylov-subspace technique for the simulation of RF/microwave subsystems driven by digitally modulated carriers", *Int. Journal RF Microwave Computer-Aided Eng.*, Vol. 9, Nov. 1999, pp. 490-505.

[29] K. Rosengreen, P.S. Kildal, “Radiation efficiency, correlation, diversity gain and capacity of a six-monopole antenna array for a MIMO system: theory, simulation and measurement in reverberation chamber”, *IEE Proc. Microwaves, Ant. and Prop.,* Vol. 152, Feb. 2005, pp. 7–16.

[30]T.K.K. Tsang, M.N. El-Gamal,“Ultra-Wideband(UWB) communication systems: an overview”, IEEE-NEWCAS Conference, 2005. The 3rd International, pp. 381 – 386, 19-22 June 2005.

[31] “First report and order, revision of part 15 of the Commission’s rules regarding ultra-wideband transmission systems”, FCC, Washington, DC, ET Docket 98-153, Feb. 14, 2002.

[32]R. J. Fontana, “Recent System Applications of Short-Pulse Ultra-Wideband (UWB) Technology”, IEEE Trans. Microwave Theory and Techniques, Vol. 52, pp. 2087-2104, Sept. 2004.

[33] J. D. McKinney, I. S. Lin and A. M. Weiner "Shaping the power spectrum of ultra-wideband radio-frequency signals", *IEEE Trans. Microwave Theory Tech.,* Vol. 54, no. 12, pp. 4247-4255, Dec. 2006.

[34] V. Rizzoli, A. Costanzo, D. Masotti, A. Lipparini, and F. Mastri "Computer-aided optimization of nonlinear microwave circuits with the aid of electromagnetic simulation", *IEEE Trans. Microwave Theory Tech.,* Vol. 52, no. 1, pp. 362-377, Jan. 2004.

[35] S. H. Choi, J. K. Park, S. Kim, and J. Y. Park, "A new ultra-wideband antenna for UWB applications", *Microwave Opt. Technol. Lett.,* Vol. 40, no. 5, pp. 339-401, March 2003.

[36] V. Rizzoli, A. Costanzo, and P. Spadoni, "CAD Procedures for the nonlinear/electromagnetic co-design of integrated microwave transmitters", *2007 IEEE MTT-S Int. Microwave Symp. Digest*, Honolulu, HI, June 2007.

[37] X. Duo, T. Torikka, Li-Rong Zheng, M. Ismail, H. Tenhunen, E. Tjukanoff, “ A DC-13GHz LNA for UWB RFID applications”, Norchip Conference, 2004. Proceedings, pp. 241 – 244, 8-9 ,Nov. 2004.

[38] R. Kohno; M. McLaughlin; and M. Welborn, "DS-UWB Physical Layer Submission to 802.15 Task Group 3a," IEEE Document number 802.15-04-0137r4.

[39] V. Rizzoli, D. Masotti, F. Mastri, R. Gaddi “Nonlinear Modelling of Reconfigurable Microwave Components based on resistive MEMS Switches”, *2007 37th European Microwave Conference*, Munich, 3-8 Oct. 2007.

[40] S. Loizeau, A. Sibille, "Reconfigurable Pifa Antenna with UltraWideband Tuning”, EUCAP, Edinburgh, UK. 11 - 16 Nov. 2007.

[41] V. Rizzoli, A. Lipparini, “Propagazione elettromagnetica guidata / 1” , Ed. Progetto Leonardo, pp. 115-123.